Fall 12-2022

Numerical Simulation of Electroosmotic Flow of Viscoelastic Fluid in Microchannel

Jianyu Ji
Old Dominion University, jianyuji1993@gmail.com

NUMERICAL SIMULATION OF ELECTROOSMOTIC FLOW OF VISCOELASTIC FLUID IN MICROCHANNEL

by

Jianyu Ji
B.S. May 2016, Nanjing University of Aeronautics and Astronautics, China
M.S. March 2019, Nanjing University of Aeronautics and Astronautics, China

A Dissertation Submitted to the Faculty of
Old Dominion University in Partial Fulfillment of the
Requirements for the Degree of

DOCTOR OF PHILOSOPHY

MECHANICAL ENGINEERING

OLD DOMINION UNIVERSITY
December 2022

Approved by:

Xiaoyu Zhang (Director)

Venkat Maruthamuthu (Member)

Tianbing Xu (Member)

Yan Peng (Member)

ABSTRACT

NUMERICAL SIMULATION OF ELECTROOSMOTIC FLOW OF VISCOELASTIC FLUID IN MICROCHANNEL

Jianyu Ji
Old Dominion University, 2022
Director: Dr. Xiaoyu Zhang

Electroosmotic flow (EOF) has been widely used in various biochemical microfluidic applications, many of which often involve the use of viscoelastic non-Newtonian fluids. Due to the existence of the elastic effect, the viscoelastic EOF develops into chaotic flow under extremely low Reynolds numbers, which is known as elastic turbulence. The mechanism of elastic turbulence in electroosmotic flow remains unclear. Numerical simulation plays an important role in understanding the mechanisms of elastic turbulence. This dissertation is aimed to study the EOF of viscoelastic fluids in constriction microchannels under various direct current (DC) and alternating current (AC) electric fields. First, the EOF of viscoelastic fluid in a straight contraction microchannel is investigated. The influences of the polymer concentration and the applied DC electric field on the elastic instabilities are analyzed. The flow fluctuations and secondary upstream vortices before the entrance of the microchannel are found to be related to the induced elastic stress within the microchannel. The polymer concentration shows a more significant influence on the elastic instability. A flow map in polymer concentration and electric field domain is formed as guidance for further studies.

Then, the study is extended to the viscoelastic EOF in a microchannel with 90° bends under the combination of DC and AC electric fields. The elastic turbulence is identified from the fluctuation of the velocity field and upstream vortices. The energy spectra of the velocity fluctuation show power-law decay over a wide range of frequencies, which is a typical characteristic of elastic

turbulence. The 90° bends show influence on the dye concentration profile in cross sections of the microchannel. A more even dye concentration distribution is obtained with an increasing number of 90° bends. Moreover, the opening angle of the particle trace at the exit of the contraction microchannel show dependency on the frequency of the AC electric field, which is related to the characteristic frequency of the viscoelastic EOF.

The study is then focused on the influence of the frequency of the AC electric field on the viscoelastic EOF. Short contraction microchannels are adopted for the frequency study. The peak in the energy spectra of the velocity fluctuation under DC electric field indicates the characteristic frequency of the viscoelastic EOF. Under AC electric field, the highest amplitude of the energy spectra is obtained when the frequency of AC electric field is close to the characteristic frequency. The same trend is also observed in the statistical results of the average velocity. However, when the frequency is relatively high, both the amplitude of the energy spectra and the average velocity decrease to a level even lower than under a DC electric field, which indicates the existence of an optimal frequency of the AC electric field in order to achieve the highest flow rate.

This dissertation is dedicated to my parents.

ACKNOWLEDGEMENTS

I would like to acknowledge each of the following special individuals who provided invaluable support during my Ph.D. study at Old Dominion University.

First, I would like to express my sincere gratitude to my advisors Dr. Xiaoyu Zhang and Dr. Shizhi Qian. I am truly grateful that I had the chance to study things in different areas with both professors. During my Ph.D. study, I have been greatly encouraged and motivated by them and learned a lot from their careful guidance, passion for our field, and kind academic mentoring. The things I learned from them will have a deep influence on my career.

To my dissertation committee, Dr. Venkat Maruthamuthu, Dr. Tianbing Xu, and Dr. Yan Peng, I would like to thank them for their contribution to my Ph.D. study. They have given me valuable comments on my research work from different perspectives, which has inspired me and helped me to find a way to improve my research work.

I would also like to thank my lab mates Bingqi and Rohan. It is a great pleasure to study and work with them. They have been strongly supportive and helped me greatly in both my study and my life. And I learned many skills from them that can make me better.

Last, my hearty thanks to my parents and my sister for their support during my study abroad. They always encourage me whenever I have any difficulties. They have more confidence in me even than I do. Without them, I could not be where I am today.

NOMENCLATURE

Re	Reynolds number
Wi	Weissenberg number
El	Elastic number
$\dot{\gamma}$	Shear gradient
ρ	Volumetric density of the fluid
F	Faraday's constant
R	Universal gas constant
T	Absolute temperature
c_0	Bulk salt concentration
Ψ	Total electric potential
ϕ_{Ext}	Externally applied electric potential
ψ	Intrinsic electric potential
ζ	Wall zeta potential
ρ_{E}	Volumetric charge density
z_i	Valence of ionic species i
N	Total number of ionic species
c_{i0}	Ionic concentration of ionic species i
ε_f	Permittivity of the electrolyte solution
η_{s}	Solvent viscosity
η_{p}	Polymeric viscosity

η_0 Total viscosity

λ Relaxation time of polymer molecules

λ_D Debye length

N_1 First normal stress difference

$\mathbf{Q}$ End-to-end connector vector of the polymer chains

ξ Slip parameter of network in PTT model

TABLE OF CONTENTS

Page

LIST OF TABLES

LIST OF FIGURES

Figure Page

Figure Page

Figure Page

Figure Page

Figure Page

Figure Page

CHAPTER 1

INTRODUCTION

1.1 Microfluidics

In various physical, chemical, and biological applications, utilizing microsystems has many advantages over traditional macro-scale devices, such as low sample consumption, quick response time, high throughput, and heat and mass transfer improvement. Microfluidics refers to the science related to the behavior, precise control, and manipulation of fluids in constrained microchannels [1-4], which involves a wide range of disciplines, such as engineering, chemistry, biochemistry, physics, nanotechnology, and biotechnology. Additionally, it is used to create microfluidic systems and devices with chambers and tunnels through which fluids can flow or be contained. The development of microfluidic systems was initially motivated by the demand for micro-analytical tools for biological and chemical applications [5-9]. In the past few decades, significant advances in microfabrication technology have boosted various practical applications for microfluidic devices, such as lab-on-a-chip technology for transporting [10, 11], mixing [12-14], separating [15, 16], or otherwise processing fluids with features of small volumes or small sizes [17]. Due to a high surface-to-volume ratio, fluid handling at the microscale can differ from macro devices. At the macro-scale, fluid volume effects dominate over surface effects, and the flow is driven by pressure gradients or gravitational force. However, on the microscale, a significant difference is the dominance of surface forces, such as surface tension or viscous friction over body forces, such as inertia, which can lead to exciting phenomena and can be exploited for new uses. For example, very low Reynolds numbers are always expected for microfluidic devices, of which an essential consequence is that flow becomes laminar rather than turbulent, and co-flowing fluids do not necessarily mix in the traditional sense. Another example is capillarity, which is negligible in

macro devices. However, it becomes significant in microchannels and can be used to lead solutions into microchannels [18-20]. When comparing microfluidic devices to normally sized systems, there are various advantages. Microfluidics' small volume makes it possible to analyze and use fewer samples, chemicals, and reagents, saving pricey samples and lowering overall application costs. The compact sizes of the microfluidic devices allow integration and many operations executed at the same time, shortening the time of the experiment. The design of the microfluidic chip is such that the incorporation of automation enables the user to produce multi-step reactions with little technical knowledge and many functionalities With the aforementioned advantages of microfluidics and the rapid development of micro-fabrication technologies since the emergence at the beginning of the 1980s, microfluidics has been used in various advanced applications, such as molecular biology [21, 22], DNA analysis [23], polymer processing [24], bio-fluid and food science [25] and the list goes on.

1.2 Viscoelastic fluid

1.2.1 Properties of viscoelastic fluid

In electroosmotic flow, the working fluid is typically an electrolyte solution, such as a KCL aqueous solution, which can be simply described by the well-known Newtonian law of viscosity. The Newtonian model assumes a constant viscosity tensor and a linear relationship between the shear stress and the local shear rate, which is the simplest mathematical model of fluids that account for viscosity. In reality, no real fluid fits the definition perfectly. Particularly, in many practical applications, solutions show strong viscoelasticity due to the additives of fluids with complex structures. Viscoelastic fluid exhibits both viscous and elastic characteristics when stress is applied and always shows non-linear properties. Some typical characteristics of viscoelastic fluid include creep, anisotropy, stress relaxation, the presence of normal stress differences in shear

flow, and hysteresis phenomenon [26]. These characteristics are interactively connected, resulting in some distinctive behaviors of viscoelastic fluid flow.

The elastic effect of the viscoelastic fluids originates from the polymer structure in the fluid. As illustrated in Figure 1.1, the polymers are in a coiled configuration when the shear gradient $\dot{\gamma} \equiv \partial v_x(y)/\partial y$ is small. Once shear gradients become large enough, the elastic polymers are stretched and acquire an average orientation making the fluid anisotropic. As a result, a normal stress difference N1 $\equiv \tau_{p,xx} - \tau_{p,yy}$ is built up, which is the most important effect [27] of polymer solutions. In the above equation, $\tau_{p,xx}$ is the normal stress along the flow direction and $\tau_{p,yy}$ is the normal stress in the transverse flow direction. For simple shear flows of Newtonian fluids, $\tau_{xx} = \tau_{yy} = 0$, and therefore, $N_1 = 0$. In viscoelastic fluids, however, N_1 increases quadratically with the increase of shear rate $\dot{\gamma} \equiv \partial v_x(y)/\partial y$.

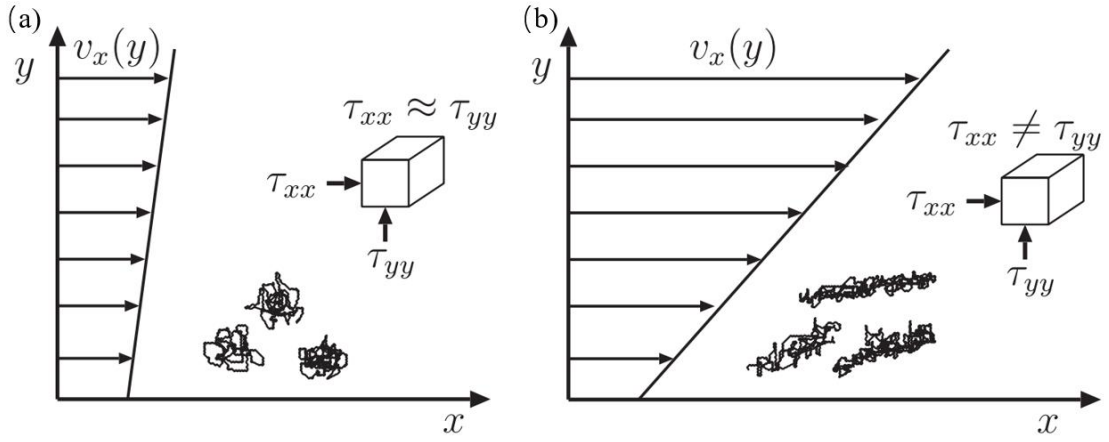

Figure 1.1 Qualitative illustration of the coiled and stretched configurations of the polymer molecules in a simple shear flow $v_x(y)$ in the x direction. (a) For small velocity gradients, the polymers are circularly symmetric without deformation. (b) At large shear rates, the polymers are stretched and oriented, resulting in the normal stress difference. [28]

For viscoelastic fluids, the relevant dimensionless numbers characterizing the fluid rheology include the Reynolds number *Re*, the Weissenberg number *Wi*, and the Elasticity number *El*. For elastic polymers, the viscosity increases rapidly with the polymer length [29]. Therefore, the inertial effects are usually small since the Reynolds number *Re* is inversely proportional to the viscosity, which is defined as

$$Re = \frac{\rho U_0 D}{\eta_0}, \tag{1.1}$$

where D is the characteristic length scale, U_0 is the velocity of the flow, ρ is the fluid density, and η_0 is viscosity.

Since the Reynolds number *Re* is small for fluids with a high degree of polymerization, the Weissenberg number *Wi* is another more important quantitative characterization for the rheology of sufficiently long polymers, which measures the elasticity level of fluids and is defined as the ratio between the relaxation time of the polymers and the characteristic flow time as

$$Wi = \frac{\lambda U_0}{D}, \tag{1.2}$$

The relaxation time λ accounts for the time scale on which a stretched polymer blob to its equilibrium scape in the absence of shear. The limiting case $\lambda \to \infty$ corresponds to the purely elastic material, while $\lambda \to 0$ corresponds to the viscous material. For $Wi << 1$, the fluid behaves essentially like a regular Newtonian fluid, while when *Wi* is around one or larger than one, the viscoelastic properties make the polymer solutions complex and very different from a Newtonian fluid.

In order to evaluate the relative strength of the elastic and inertial effects, another important dimensionless number, Elasticity number *El* for viscoelastic fluid, is defined as the ratio between *Wi* and *Re* as

$$El = \frac{Wi}{Re} = \frac{\lambda \eta_0}{\rho D^2}, \tag{1.3}$$

In microfluidic systems, viscoelastic fluid flow is typically characterized by a low Reynolds number, high Weissenberg number, and high Elasticity number. When the Weissenberg number is around or larger than 1, the characteristic time is relatively small compared to the relaxation time of the polymer. Hence the stretched polymer molecules do not have enough time to return to the original coiled configuration. Under such flow conditions, the viscoelastic effect dominates over the fluid inertia making the flow different from Newtonian fluids.

1.2.2 Elastic instability

For Newtonian fluids, the flow regime is characterized by the Reynolds number. When the Reynolds number is low, the flow is in a laminar flow regime. When the Reynolds number is relatively high, the stable laminar flow develops into turbulence with instabilities due to the nonlinearity of the inertial force. In microchannels, due to the small scale, the Reynolds number is always rather small, and inertial nonlinearity is negligible. However, flow instabilities of viscoelastic fluids have been widely reported even under extremely low Reynolds numbers [30-32]. Such instability and turbulence without the inertia of zero-Reynolds number flow were first systematically studied in a Taylor-Couette cell [30], where viscoelastic fluid flows in concentric rotating cylinders. Wave structures propagating in both the radial and axial directions were observed, and the wavelength and wave number are determined by the curvature, time, and Weissenberg number. Such instability was called elastic instability and turbulence. It has been reported that viscoelastic flows tend to become linearly unstable due to the existence of extra normal stress when there are curvature streamlines in the flow [30, 33, 34]. As illustrated in Figure 1.2 (a), when the Weissenberg number is larger than 1, the polymer is stretched by the shear gradients. Due to the larger curvature and larger shear near the center, the inner side of the polymer

from the upstream stretches and rotates, resulting in a new configuration downstream. Therefore, the polymer is pulled towards the center when curvature exits in the streamline, which also explains the mechanism of the rod-climbing effect [27] of viscoelastic fluids. In a confined curve flow with Weissenberg numbers larger than 1, the significant normal stress effect tends to pull the fluid element in towards the center region with higher curvature. Therefore, a slightly perturbed flow regime is illustrated in Figure 1.2 (b). Some of the fluid elements move inwards towards regions with larger shear, and some fluid elements move outwards. The pulling force increases near the center with stronger shear, while the force decreases far away from the center. Thus, the perturbing effect is self-enhancing, resulting in an unstable flow when the pulling force is large enough.

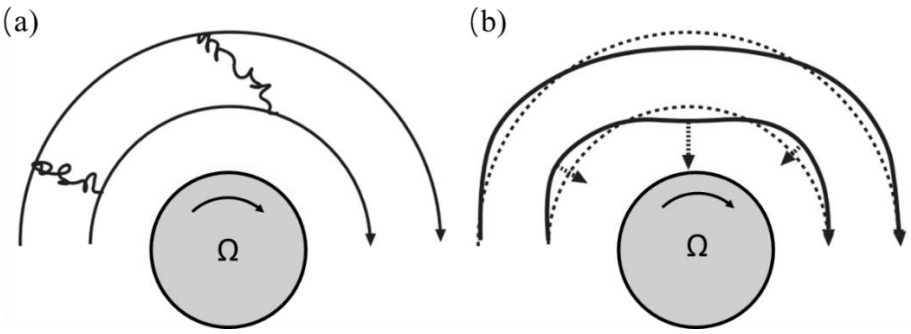

Figure 1.2. Qualitative sketch of a flow situation with curved streamlines. When the Weissenberg number is large enough, the normal stress is significant. The normal forces tend to pull a fluid element in towards the region of the largest curvature of the streamlines and largest flow rate. (a) The polymer from upstream is stretched and oriented by the flow to a new situation downstream. Effectively, the polymer is pulled inwards. (b) Small perturbations of the streamlines (the full lines) show that fluid elements that are displaced inwards towards regions of larger curvature are pulled in even more, and the fluid elements that are displaced outwards are being pulled in less, resulting in an unstable flow. [28]

Since Rayleigh first proposed the concept of elasticity-induced instability in 1880 [35], viscoelastic fluids have attracted numerous researchers' attention. The elastic instability and turbulence greatly enrich the flow behaviors of the viscoelastic fluid in microscales and nanoscales. Much more attention has been paid to elastic instability in microchannels recently due to their practical applications in the improvement of mixing performance and enhancement of heat transfer in microdevices [36-38]. Various flow conditions have been investigated experimentally and theoretically, such as some typical flow geometries investigating elastic instability, as illustrated in Figure 1.3. The flow conditions can be summarized in three main categories: (1) shear-dominated flow, which refers to the flow that the velocity gradient direction is perpendicular to the flow direction, such as flows between two parallel plates [39, 40], flows in the cavity [34, 41], flows in serpentine channels [42, 43], Taylor-Couette flow [44]; (2) extension dominated flow, which refers to the flow with strong stream-wise velocity gradients, and often occurs in contraction-expansion channels [45-47], stagnation point flows (cross-slot [31, 48], T- and Y-shaped channels [49, 50]); and others [33, 51, 52].

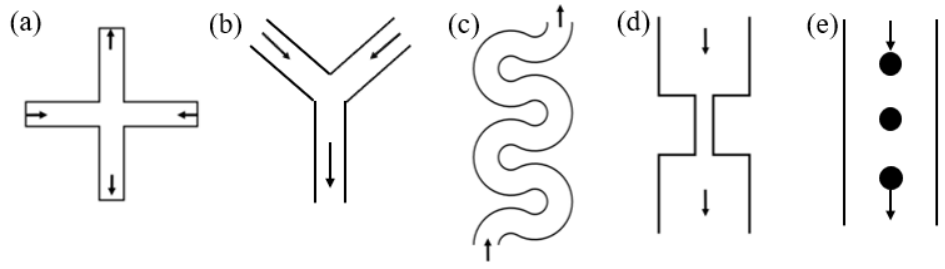

Figure 1.3. Schematic geometries of several flow conditions investigated for the elastic instabilities of viscoelastic fluids: (a) flow in cross-slot, (b) flow in Y-shape channel, (c) flow in serpentine channel, (d) flow in contraction/expansion channel, (e) flow past solid obstacles.

1.2.3 High Weissenberg Number Problem

The research on numerical solutions to non-Newtonian flow problems has grown rapidly since the early 1970s. Descriptions and applications of a wide range of sophisticated techniques have been described and applied for the solution of highly non-trivial flows through complex geometries and at high Deborah numbers. Initially, researchers attempted to modify the algorithms and methods previously used to solve Newtonian flow issues. However, the results were disappointing for the simulation of flows with highly elastic liquids. The early computations were plagued by a loss of convergence of numerical algorithm at relatively low measures of the fluid elasticity [53], which is quantified by the Weissenberg number (*Wi*). Such numerical instability was found in a wide range of viscoelastic models for various numerical techniques, and they were commonly associated with a loss of resolution of discretization methods to solve the exponential growth of stresses at critical points [54]. The critical values of *Wi* can be improved depending on the type of viscoelastic fluid and the numerical methods and discretization schemes utilized but they cannot be eliminated. For example, Crochet and Keunings [55, 56] found that the domain of convergence in *Wi* was significantly larger than using an Oldroyd B model rather than an upper-convected Maxwell (UCM) model in die swell problems, but they still encountered a limiting value. This is the so-called 'High Weissenberg Number Problem (HWNP)', which has been one of the major outstanding problems in the numerical simulation of non-Newtonian flow.

The origin of the HWNP has been lately discovered. As mentioned earlier, by definition, the conformation tensor should be symmetric positive definite. However, the conformation tensor was found to lose the positive-definiteness when *Wi* is relatively high, which is a precursor of the HWNP [57, 58]. Moreover, the viscoelastic flows tend to have stress boundary layers with large variations in the stress gradients, such as exponential stress profiles near geometrical singularities

[59]. It is very challenging to accurately present the stress gradients due to the polynomial interpolations of exponential profiles. The numerical instabilities were found to be arising from the under-resolution of spatial stress profiles [58, 60].

Several techniques have been developed to solve the HWNP by enforcing the positiveness of the conformation tensor. For example, using the eigendecomposition and the Cholesky decomposition of the conformation tensor, Vaithianathan et al. [61] proposed two matrix decomposition-based schemes that can guarantee the positive-definiteness of the conformation tensor. Lozinski et al. [62] proposed the square root conformation formula based on the matrix decomposition of the conformation tensor with its principal square root. Afonso et al. [63] presented a generic kernel-conformation tensor transformation that has been successfully applied to various constitutive models. Some other schemes include the stabilized mixed three-field finite element method by Kwack et al. [64] and the finite difference-based kernel-conformation tensor transformation by Martins et al. [65]. However, the approach that is now most often used is the log-conformation method developed by Fattal and Kupferman [54], which involves changing a variable while utilizing the matrix logarithm of the conformation tensor. The log-conformation representation enhances the depiction of huge stress gradients while still maintaining positive definiteness since it linearizes the exponential stress profiles.

1.3 Electroosmotic flow of viscoelastic fluid

1.3.1 Electric Double Layer

An aqueous solution in contact with a dielectric substance causes ion absorption or dissociation at the solid/liquid interface, which charges the surface electrostatically. Counter-ions will be drawn to the charged surface, while co-ions will be repelled away from it due to the electrostatic interaction between the surface charge and the solution's ions. Consequently, near the charged

surface, a thin layer of what is known as the "electric double layer" (EDL) forms, where counter-ions gather and outnumber co-ions. EDL is often thought to consist of two layers, as shown in Figure 1.4: the Stern layer near the solid/liquid boundary and the diffusive layer beyond the Stern layer. The Stern layer only contains one layer of immobile counter-ions due to the strong electrostatic interaction between the surface charge and the counter-ions. Adjacent to the Stern layer, there is a thicker and more diffuse layer, where counter-ions dominate over the co-ions, and both are mobile. The bulk fluid outside the EDL is electrically neutral.

The variation of the electric potential across the EDL is plotted in Figure 1.4. The induced electric potential gradually decreases to zero in the direction normal to the charged surface since it is proportional to the difference between the concentrations of counter-ions and co-ions, which gradually decreases with increasing wall distance. The wall surface potential and zeta potential are the terms used to describe the potential at the solid/liquid interface (ϕ_s) and the potential at the Stern layer/diffusive layer interface (ϕ_d). Even though the Stern layer is typically only a few angstroms, it should be noted that the wall surface potential is different from the zeta potential unless the Stern layer effect is neglected. The electric potential arising from the charged surface first linearly reduces from the wall surface potential to the zeta potential within the Stern layer, then exponentially decays within the double layer. The zeta potential is often used to approximate the wall surface potential due to the difficulty in measuring or quantifying the wall surface potential. Beyond the diffusive layer, the charged surface's electrostatic influence is minimal, and the net charge almost disappears [66, 67]. The thickness of the EDL is dependent on the bulk salt concentration, which is characterized by a Debye Length λ_D:

$$\lambda_D = \sqrt{\frac{\varepsilon_f RT}{F^2 \sum_{i=1}^{N} z_i^2 c_{i0}}}, \tag{1.4}$$

where ε_f is the permittivity of the electrolyte solution; F is Faraday's constant; R is the universal gas constant; T is the absolute temperature; z_i is the valence of the ionic species; N is the total number of ionic species; c_{i0} is the bulk salt concentration.

Under equilibrium conditions, the concentration of the i^{th} ionic species, c_i, can be described by the Boltzmann equation,

$$c_i = c_{i0} \exp\left(-\frac{z_i F \phi}{RT} \right), \tag{1.5}$$

where ϕ is the electric potential arising from the charged surface, which is governed by the Poisson equation:

$$-\varepsilon_0 \varepsilon_f \nabla^2 \phi = \rho_{\text{E}}. \tag{1.6}$$

In the above, ε_0 is the absolute permittivity in a vacuum; and ρ_{E} is the mobile space charge density, which can be described by:

$$\rho_{\text{E}} = \sum_{i=1}^{N} F z_i c_i. \tag{1.7}$$

Substituting Equation (1.5) and Equation (1.7) into Equation (1.6), the Poisson-Boltzmann (PB) equation can be obtained to describe the electric potential distribution near a charged surface,

$$-\varepsilon_0 \varepsilon_f \nabla^2 \phi = F \sum_{i=1}^{N} z_i c_{i0} \exp\left(-\frac{z_i F \phi}{RT} \right). \tag{1.8}$$

If the absolute value of the valence of all species is equivalent, i.e., $z = |z_i|$ for i = 1-N, the PB equation can be further simplified as:

$$\nabla^2 \phi = \frac{RT\kappa^2}{zF} \sinh\left(\frac{zF\phi}{RT} \right), \tag{1.9}$$

With $\kappa^{-1} = \lambda_D = \sqrt{\varepsilon_0 \varepsilon_f RT / 2z^2 F^2 c_0}$ being the Debye length, and c_0 being the bulk concentration of all counter-ions or co-ions.

If $|\psi| \ll \frac{RT}{zF}$, $\sinh\left(\frac{zF\phi}{RT}\right) \approx \frac{zF\phi}{RT}$, Equation (1.9) can be linearized by the Debye-Hückel approximation [67]

$$\nabla^2 \phi = \kappa^2 \phi, \tag{1.10}$$

based on which the electrical potential decays exponentially away from the charged surface.

When brought into contact with an electrolyte, the majority of materials (such as silicon substrates or glass) utilized in the construction of microfluidic devices spontaneously acquire a surface electric charge. Therefore, selecting the proper materials to stimulate EOF is important. The zeta potential varies depending on the solid surface as well as the chemicals in the fluid, especially the pH of the buffer solution. Table 1.1 provides typical zeta potential values for various fluids in contact with PDMS and silica-coated glass.

Table 1.1 Zeta potentials for different solutions and materials [68].

Solution	Solution pH	Zeta potential ζ(mV)	
		PDMS	Silica-coated glass
HEPES*	7.2	−59.0 ± 1.4	−57.9 ± 0.6
Acetate	4.7	−17.2 ± 3.6	−35.5 ± 0.7
Borate	9.4	−74.4 ± 1.2	−69.5 ± 1.2

*HEPES: 4-(2-Hydroxyethyl) piperazine-1-ethanesulfonic acid.

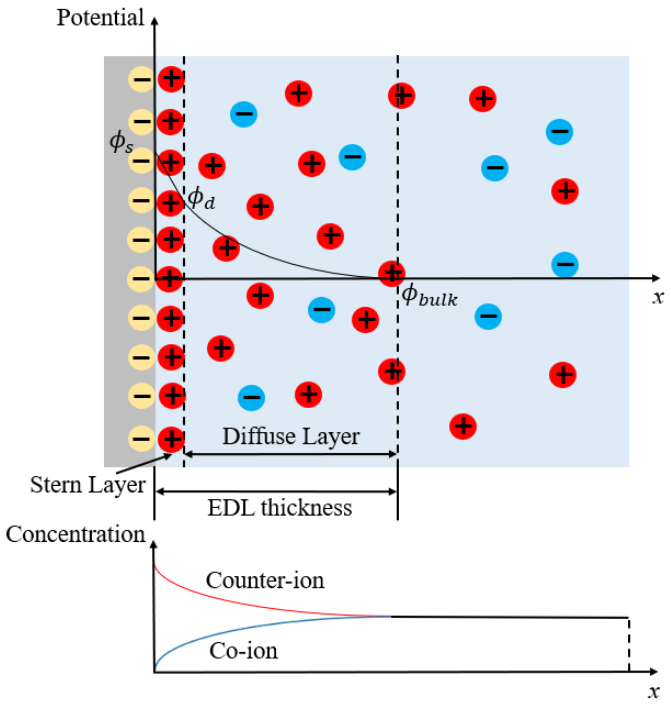

Figure 1.4. Schematic diagram of the EDL structure, the potential, and ionic concentration profile.

1.3.2 Electroosmotic flow

When an external electric field is applied parallel to a negatively or positively charged surface, due to the non-neutral charge within the EDL, the interaction between the external electric field and the net charges accumulated within the EDL generates an electrostatic force exerting on the fluid, driving the fluid toward the cathode or anode, as schematically depicted in Figure 1.5. Such fluid motion is called electroosmotic flow (EOF) [69, 70]. EOF was first reported in the flow of water within a plug of clay under an external electric potential difference by Resus in 1809 [71]. Since then, in-depth investigations into the mechanism of the EOF have been conducted, and much later, practical applications such as electrokinetic micro pumps have also been developed. The EOF-based micropumps are more desirable and useful than traditional pressure-driven micropumps for several advantages. A parabolic velocity profile is commonly observed in

pressure-driven flow, which is highly dependent on the characteristic length of the channel. Therefore, the velocity of the pressure-driven flow in micro/nano channels is limited to a relatively small level. However, the channel height has no effect on the plug-like velocity profile in EOF when the EDL is thin. Moreover, the EOF requires less mechanical manufacturing and accurate control. Numerous studies have been performed on EOF both experimentally [72-74] and theoretically [75, 76] due to the wide applications of EOF in various fields.

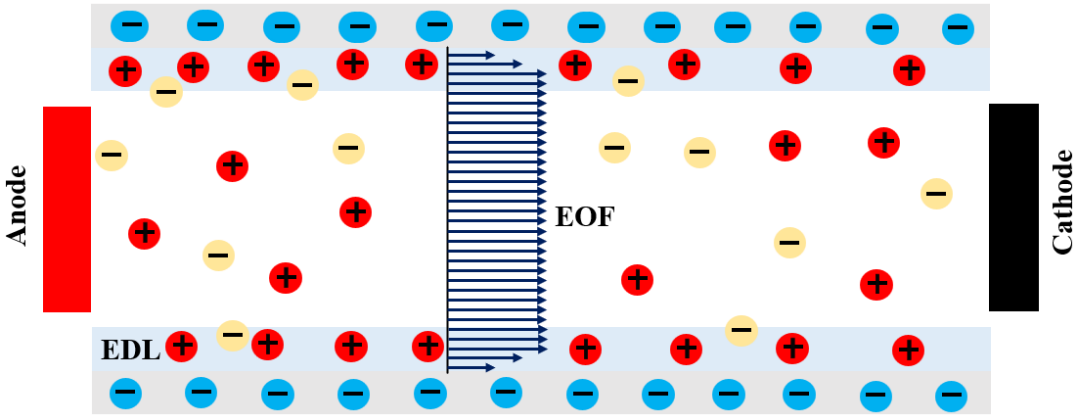

Figure 1.5 The schematic diagram of the electroosmotic flow in a microchannel bearing negative surface charge.

The EOF of the incompressible electrolyte solution is governed by the modified Navier-Stokes equation by taking into account the electrostatic force,

$$\rho\left(\frac{\partial \mathbf{u}}{\partial t}+\mathbf{u}\cdot\nabla\mathbf{u}\right)=-\nabla p+\mu\nabla^2\mathbf{u}-\rho_e\nabla\phi, \tag{1.11}$$

and the continuity equation

$$\nabla\cdot\mathbf{u}=0, \tag{1.12}$$

where ρ is the volumetric density of the fluid, p is the pressure, and μ is the fluid viscosity. The electrochemical ion transport is described by the Poisson-Nernst-Planck equation (PNP). Suppose

the electrolyte solution contains N different types of ionic species, and the ionic concentration of the i^{th} ionic species is c_i. When an external electric field is present in the electrolyte solution, c_i is governed by the Nernst-Plank equation:

$$\frac{\partial c_i}{\partial t} + \nabla \cdot \left(\mathbf{u} c_i - D_i \nabla c_i - z_i \frac{D_i}{RT} F c_i \nabla \phi \right) = 0, \ i = 1, ..., N, \tag{1.13}$$

where D_i is the diffusivity of the i^{th} ionic species, and the electric potential ϕ is described by the Poisson equation as shown in Equation (1.6). The above coupled equations system is called the NS-PNP system, which is highly nonlinear and computationally intensive. To avoid the nonlinearity in the system, many studies have investigated the approximation of the system by linearizing the electrochemical model [77, 78]. One of the most commonly used simplifications is the Poisson-Boltzmann model, as shown in Equation (1.8), by assuming the ionic species distribution follows the Boltzmann equation as described in Equation (1.5).

1.3.3 Electroosmotic flow of Newtonian fluids

After the first demonstration of the principle of electroosmosis by Reuss [79] in the 19th century, EOF of Newtonian fluids has been extensively investigated analytically [80, 81], numerically [82], and experimentally [74] by many researchers over the past 30 years due to the wide range applications of EOF. The following section discusses some of the significant studies of Newtonian EOF.

Important parameters of EOF have been investigated based on Newtonian fluids utilizing a variety of techniques and methods. The EDL theory was developed by Helmholtz in 1879 [83], relating the electric and flow parameters for electrokinetic transport and defining the EDL thickness as a function of the relevant physical quantities. Von Smoluchowski [84] expanded on Helmholtz's double layer theory analyzing the situation in which the EDL thickness is considerably less than the channel dimensions, and derived a velocity slip condition for EOF. Dutta

and Beskok [80] investigated the analytical solution for velocity distribution, mass flow rate, pressure gradient, wall shear stress, and vorticity in mixed electroosmotic/pressure-driven flows in two-dimensional straight channel geometry. There are numerous analytical and numerical studies of fully developed and steady EOF in various geometries. Rice and Whitehead [85] theoretically studied the electrokinetic flow in narrow cylindrical capillaries. Levine et al. [86] developed a theory of electrokinetic flow in parallel plates considering double layer overlap. Herr et al. [87] analytically and experimentally investigated the EOF in cylindrical capillaries with nonuniform wall surface charge distributions. The model and experimental results showed that the velocity profile and sample-dispersion rate are a function of the local potential and system-average potential in the capillary system. Ghosal [88] investigated the effects of slowly varying cross-section geometry and wall charge on EOF in a microchannel using a lubrication approximation, and the pressure gradient introduced by variations in cross-section geometry was found to increase the Taylor dispersion. Kim et al. [89] performed a numerical study of EOF using the PB model in a straight channel with a groove and a T-junction with a rectangular cross-section. The numerical results validated the experimental results of velocity distribution. Kang et al. [90] presented an analytical scheme to solve the Poisson-Boltzmann equation for arbitrary zeta potential and analyzed the dynamic electroosmotic flow in a cylindrical capillary. The electroosmotic flow for microchannels with arbitrary cross-sections and heterogeneous potential was examined in the study of Xuan and Li [91]. Yan et al. [92] proposed a model to assess the finite reservoir impacts on the EOF in a rectangular microchannel. In addition to the numerous analytical and experimental investigations, numerical simulations of the electroosmotic flow in complicated geometries of microchannel networks have been performed [93-96].

In many analyses of EOF, the ionic distribution in the electric double layer is assumed to follow the equilibrium Boltzmann distribution, and the Poisson-Boltzmann equation is used to describe the electric potential induced by the ions [78, 97, 98]. However, in some applications, the convective transport of the ions may have significant effects. Park et al. [99] compared the Poisson-Boltzmann model and the Nernst-Planck equations for the study of steady and unsteady EOF in a straight microchannel and an irregular microchannel with sudden expansion and contraction. For the EOF thought straight channel, the results of the two models are almost the same in the predictions of the EOF when the electric double layer is very thin. However, the results show a significant discrepancy when the electric double layer becomes thicker. In the irregular channel, the two models show the same dependency on the thickness of the electric double layer. However, when the external electric field is relatively high, the PB model predicted circulation in the EOF, while the result of the NP model shows no circulation.

In summary, numerous studies have been performed investigating various conditions and models for the EOF of Newtonian fluids. The Newtonian EOF in different geometries has also been extensively studied and elaborated by many researchers. However, the more complex EOF involving non-Newtonian fluids remains to be better understood, and the literature is rather limited.

1.3.4 Electroosmotic flow of generalized Newtonian fluids

A generalized Newtonian fluid (GNF) is a type of non-Newtonian fluid for which the constitutive equation is generalized from the Newtonian fluid. The shear stress of a generalized Newtonian fluid is a function of shear rate but is not dependent on the history of deformation. Generalized Newtonian fluids can be described by the following rheological equation:

$$\tau = \mu_{\text{eff}}\left(\dot{\gamma}\right)\dot{\gamma}, \tag{1.14}$$

where τ is the shear stress, $\dot{\gamma}$ is the shear rate, and $\mu_{\text{eff}}(\dot{\gamma})$ denotes an effective viscosity of the fluid as a function of the shear rate. Some of the most commonly used types of generalized Newtonian fluids include Power-law fluid [100-102], Cross fluid [103, 104], Carreau fluid [104-106], and Bingham fluid [107-109], etc.

Due to the generalized constitutive equations, it is relatively easy to obtain exact solutions for generalized Newtonian fluids. The EOF of generalized Newtonian fluids has been investigated by many researchers focusing on theoretical and analytical solutions [110] and numerical simulation [111]. The power-law fluid model is the mostly used straightforward GNF model for the analytical solution investigation of fully developed flow conditions. Das and Chakraborty [112] were among the first to employ the power-law model to investigate EOF. In their study, an estimation of the fully developed velocity and temperature distributions and an explicit expression for solution concentration distribution within the microchannel were derived for the EOF in a rectangular microchannel. Zhao et al. [110] investigated the analytical expressions for the shear stress, dynamic viscosity, and velocity distribution in a slit channel utilizing the power-law model. A generalized Smoluchowski velocity is introduced by taking into account contributions due to the finite thickness of the electric double layer and the flow behavior index of power-law fluids. Zhao et al. [113] reported the numerical results of electroosmotic mobility of a more general Carreau non-Newtonian model, presenting the detailed effects of the Weissenberg number, the surface zeta potential, and the power-law index on the electroosmotic mobility. Chakraborty [114] developed a theoretical model for studying the capillary filling dynamics of a power-law fluid in a microchannel. A detailed understanding of the fundamental capillary dynamics can improve the design of blook transportive and monitoring microsystems.

Noting that presuming a non-Newtonian fluid behaves as a purely viscous fluid may be oversimplifying reality, it is essential to compare the theoretical solutions with the data from experimental investigations. Even though the theoretical investigations of the GNF have been extensively performed, many of the solutions from the theoretical studies remain to be further validated by experimental studies.

Olivares et al. [115] analyzed the EOF of polymer solutions considering the non-Newtonian character of the fluid and the polymer concentration profile near the interface, which greatly modify the fluid viscosity. A mathematical model is derived for the EOF velocity of the solutions that present polymer depletion at the wall. In addition, experiments were carried out using carboxymethyl cellulose in fused silica capillaries to validate the consideration of the theoretical model, where both the polymer depletion and a certain degree of specific adsorption were observed to define the electroosmotic mobility.

Zhao et al. [116] presented an analysis of the electroosmotic flow of power-law fluids in the parallel-plate microchannel. Closed-form exact solutions were obtained for the electroosmotic velocity profile and the average velocity in terms of hypergeometric functions by incorporating the electrostatic body force in the electric double layer and the power-law fluid constitutive model. Two important dimensionless parameters, the fluid behavior index and the electrokinetic parameter were examined. Moreover, based on the generalized Smoluchowski velocity, an experimental method was proposed for determining the rheological properties of power-law fluids.

Similar conclusions from analytical investigations on the power-law fluids have been widely obtained by many researchers. However, as mentioned earlier, the power-law model is an ideal assumption of non-Newtonian fluids as a purely viscous fluid. In reality, many biofluids exhibit more complicated properties, such as elasticity, which can induce more complex flow behaviors.

In contrast to the extensive investigation of EOF of GNF, the study of EOF of viscoelastic fluids is relatively less.

1.3.5 Electroosmotic flow of viscoelastic fluids

The investigations described in the above section are restricted to the comparatively simple non-Newtonian model without accounting for the elastic features, as the extremely nonlinear constitutive equations substantially increase the complexity of solving the EOF of viscoelastic fluid. Compared to Newtonian fluids and generalized Newtonian fluids, there is less literature on the EOF of viscoelastic fluids. Only recently, studies on pure EOF of viscoelastic fluids have emerged. Park and Lee [117] were among the first to extend the Helmholtz-Smoluchowski velocity for Newtonian fluids to the calculation of viscoelastic fluids. The Helmholtz-Smoluchowski velocity for viscoelastic fluids was found by solving a simple cubic algebraic equation. A general constitutive equation was adopted in the governing equations, which covers six different kinds of constitutive models (i.e., Newtonian fluid, upper-convected Maxwell model, Oldroyd-B model, simplified PTT model, PTT model, and MPTT model). The derived Helmholtz-Smoluchowski velocity for different models was validated by the results obtained by solving the differential equations directly. Later, Park and Lee [118] numerically investigated the EOF and Newtonian fluid and viscoelastic fluid in a straight rectangular channel with and without external pressure. A general constitutive model was employed same as in their previous study to represent UCM, PTT, and Oldroyd-B models. For the pure EOF with no external pressure gradient, the flow rate showed a significant difference between the Newtonian fluid and the viscoelastic fluid. However, when an external pressure gradient was applied, a secondary flow was observed in the EOF of the viscoelastic fluid, which was not observed in the EOF of the Newtonian fluid.

Afonso is also among the early researchers investigating the analytical solutions for the EOF of viscoelastic fluids. Afonso et al. [119] obtained the analytical solution for combined electrokinetic and pressure forces in parallel plates using the Debye-Hückel approximation. The viscoelastic fluid was described simplified PTT model and Finitely Extensible Nonlinear Elastic with Peterlin closure (FENE-P) model. The influences of fluid rheology, EDL thickness, wall zeta potential, and the external pressure and electric potential on the fluid velocity and stress were discussed. Later, Afonso et al. [120] extended their previous study [119] to the investigation of analytical solution for asymmetric zeta potentials at the walls. Ferrás and Afonso et al. [121] also derived the semi-analytical solutions or electroosmotic annular flow of viscoelastic fluids modeled by the Linear and Exponential PTT model between two concentric cylinders under combined influences of electrokinetic and pressure forcings. And the analytical solution was valid for both no slip and slip velocity at the walls.

Based on the work of Afonso et al. [119], Dhinakaran et al. [122] investigated the analytical solution of pure EOF of a viscoelastic fluid between two parallel plates using the PTT model and the Gordon-Schow-alter convective derivative. A constitutive flow instability was predicted when the shear rate and Deborah number exceeded a critical value. The expression for the critical values of shear rate and Deborah number were reported. Sousa et al. [123] derived an analytical solution for the EOF of viscoelastic fluid under combined electroosmosis and pressure gradient forces. The viscoelastic fluid was described by the PTT model considering the near-wall skimming layer. The skimming layer is wider than the EDL, and the flow rate was enhanced compared to that of the uniform concentration flow case. Choi et al. [124] studied analytically the EOF of viscoelastic fluids in a two-dimensional microchannel with different zeta potentials using the PTT model. The velocity profiles of viscoelastic fluids showed enhancement over corresponding Newtonian fluids

under identical flow and electrochemical conditions. The dependence of the flow enhancement on Deborah number, extensibility parameter, slip parameter, Debye length, and zeta potential was illustrated quantitatively.

The theoretical studies mentioned above provide important insight into the rheological effect on the viscoelastic EOF. However, these studies are limited to comparatively basic geometries, such as between parallel plates, straight rectangular channel, straight cylinder channel. Additionally, existing studies of viscoelastic EOF have been mainly focused on the steady-state EOF under a constant applied electric field. Due to the existence of elasticity and relaxation time of viscoelastic fluids, an intriguing flow phenomena can be induced in the viscoelastic EOF when the flow condition is more complex, such as in more complicated geometries or under time-dependent external electric fields. However, studies on the time-dependent flow states and the instabilities of viscoelastic EOF are very limited.

1.4 Outline of the thesis

Chapter 1 reviews the properties of viscoelastic fluids and the intriguing flow phenomenon of viscoelastic fluid due to the existence of elasticity. The theory and mechanism of electroosmotic flow are introduced based on the equations for Newtonian fluids. The remarkable research works on electroosmotic flow for both Newtonian and non-Newtonian fluids are also reviewed. Particularly the limitation of existing studies on the electroosmotic flow of viscoelastic fluids is elaborated.

Chapter 2 includes the description of mathematical models for the EOF of viscoelastic fluids. Several commonly used constitutive models for viscoelastic fluids are introduced, along with a detailed description of the log-conformation representation and the finite volume method. Then the numerical implementation of the mathematical model in OpenFOAM is described, including

the both-sides-diffusion (BSD) technique and the coupling algorithms adopted in the viscoelastic solver in OpenFOAM.

In Chapter 3, the EOF of viscoelastic fluid in a straight contraction microchannel is investigated. The viscoelastic EOF is studied as a function of the polymer concentration and the applied electric field. The velocity field and flow patterns are analyzed to identify the elastic instabilities. The velocity profile and average velocity of viscoelastic EOF are compared with those of Newtonian EOF to reveal the effects of the elasticity on the flow. Then, the distribution of the induced elastic stress under different flow conditions is analyzed to explain the mechanism of the upstream vortices.

Chapter 4 further extends the study in Chapter 3 to contraction microchannels with 90° bends under a combination of DC and AC electric fields. The energy spectra of the velocity fluctuation in the microchannel are analyzed to identify the elastic turbulence. The dye concentration profiles at different cross-sections of the microchannel are compared to show the influence of the 90° bends on the viscoelastic EOF. Then, the opening angles of the particle trace under various flow conditions are statistically studied to investigate the influence of the frequency of the AC electric field on the elastic instability.

Chapter 5, inspired by the study in Chapter 4, performs a frequency study of the viscoelastic EOF in short contraction microchannels. Three different lengths of the microchannel and a wide range of frequencies of the AC electric field are investigated. The characteristic frequency of the viscoelastic EOF is identified by the energy spectra of velocity fluctuation. The dependency of the velocity fluctuations and the average velocity on the frequency of the AC electric field are then analyzed.

Chapter 6 summarizes the conclusions of this dissertation and some potential future directions of the research work based on the findings in this dissertation.

CHAPTER 2

MATHEMATICAL MODEL OF VISCOELASTIC FL

UID AND NUMERICAL IMPLEMENTATION IN OPENFOAM

Numerical simulation is a very useful tool to investigate and understand the properties of viscoelastic EOF, especially when the flow condition is complex. In this chapter, the mathematical model for the viscoelastic fluids flow problem is first described in general. Then, the approach and mathematical model describing the electro force in the EOF are introduced. Next, several commonly used constitutive models for viscoelastic fluids are described, followed by a detailed elaboration of the log-conformation representation for solving the High Weissenberg Number Problem. Next, the finite volume method is introduced. In the end, the numerical implementation of the mathematical model in OpenFOAM is given, including the BSD technique and the coupling algorithms adopted in the viscoelastic solver.

2.1 Mathematical model

The viscoelastic fluid is assumed to be incompressible, single-phase, and isothermal. The mass and momentum equations are described as follows:

$$\nabla \cdot \mathbf{u} = 0, \tag{2.1}$$

$$\rho\left(\frac{\partial \mathbf{u}}{\partial t} + \mathbf{u}\cdot\nabla\mathbf{u}\right) = -\nabla p + \eta_s \nabla^2 \mathbf{u} + \nabla\cdot\boldsymbol{\tau} + \mathbf{F} \tag{2.2}$$

where ρ is the fluid density; p is the pressure; η_s is the solvent dynamic viscosity; $\boldsymbol{\tau}$ is the non-Newtonian polymer stress, which can be described by various constitutive models depending on the different properties of the viscoelastic fluids; and $\mathbf{F}$ is any external body-force, such as electric force in EOF.

The non-Newtonian polymer stress $\boldsymbol{\tau}$ can be expressed in terms of the conformation tensor $\mathbf{c}$, which is a tensorial variable representing the macromolecular structure of polymers,

$$\boldsymbol{\tau} = \left(\frac{\eta_p}{\lambda} \right) f(\mathbf{c}), \tag{2.3}$$

where η_p is the polymer dynamic viscosity, λ is the relaxation time of the polymer describing the time for the polymer chains to return to equilibrium after deformation; $f(\mathbf{c})$ is a strain function dependent on the constitutive model of the fluid. The conformation tensor **c** describes the behavior of the microstructures, which is responsible for the non-Newtonian features of the fluid. Therefore, the non-Newtonian stress **τ** can be obtained as a function of the configuration of these microstructures (i.e., conformation tensor **c**). A micro-dumbbell model with a spring connecting two beads is used to describe the microstructure of the polymer chains in the stochastic microscopic theory [125], as shown in Figure 2.1. The conformation tensor represents the spatial configuration, or the orientation, of the polymer chains. It is defined as the statistical average of the dyadic product of the end-to-end connector vector **Q** [126] of the polymer chain carrying the elastic load:

$$\mathbf{c} = \frac{\langle \mathbf{Q} \otimes \mathbf{Q} \rangle}{Q_{eq}^2} = \frac{\int \mathbf{Q}\mathbf{Q}^T \kappa(\mathbf{Q}, t) d\mathbf{Q}}{Q_{eq}^2}, \tag{2.4}$$

where Q_{eq} is the equivalent length of the vector **Q**; $\kappa(\mathbf{Q}, t)$ is the probability distribution function of **Q** following the Fokker-Planck equation. Consequently, the conformation tensor is-by definition-symmetric positive definite (SPD). The conformation tensor is normalized such that it is equal to the identity matrix **I** when the polymers are at equilibrium state.

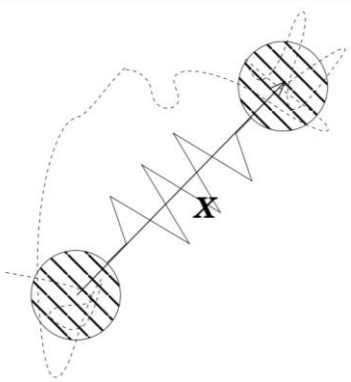

Figure 2.1 In the dumbbell model, the polymer chain is modelled by two beads linked by a spring [125].

The generic differential equation that may include the majority of the viscoelastic models controls the development of the conformation tensor,

$$\frac{\partial \mathbf{c}}{\partial t}+\mathbf{u}\nabla\cdot\mathbf{c}\frac{\partial \mathbf{c}}{\partial t}-\left(\mathbf{c}\cdot\nabla\mathbf{u}^{T}+\nabla\mathbf{u}\cdot\mathbf{c}\right)=-\frac{1}{\lambda}g\left(\mathbf{c}\right), \tag{2.5}$$

where the function $g(\mathbf{c})$ is decided by the constitutive model. In the section that follows, the full formulas of the evolution equation for the conformation tensor will be introduced based on different viscoelastic fluid models.

In electroosmotic flow, the external force **F** can be replaced by the electrical force. The total electric potential Ψ, is decomposed into two variables, $\Psi = \phi_{\mathrm{Ext}} + \psi$, with ϕ_{Ext} representing the potential originating from the externally applied electric potential while ψ being the potential arising from the charge of channel walls. In the current study, the Poisson-Boltzmann equation is used to describe the potential, ψ:

$$\nabla\cdot\left(\varepsilon\nabla\psi\right)=\rho_{\mathrm{E}}=Fc_{0}\left(\exp\left(\frac{e\psi}{kT}\right)-\exp\left(-\frac{e\psi}{kT}\right)\right). \tag{2.6}$$

The potential ϕ_{Ext} is governed by the following Laplace equation,

$$\nabla^2 \phi_{\text{Ext}} = 0. \tag{2.7}$$

Then the momentum equation yields

$$\rho\left(\frac{\partial \mathbf{u}}{\partial t} + \mathbf{u}\cdot\nabla\mathbf{u}\right) = -\nabla p + \eta_s \nabla^2 \mathbf{u} + \nabla\boldsymbol{\tau} - \rho_E \nabla\phi_{\text{Ext}}, \tag{2.8}$$

where ρ_E and ϕ_{Ext} represent, respectively the volume charge density within the electrolyte solution and the externally applied electric potential.

2.1.1 Constitutive models

The relationships between the deformations and the stress response of the material can be described through the constitutive models. The complexity of the underlying physics that results in flow instabilities in many viscoelastic flows must be captured by non-Newtonian constitutive models. There are two types of non-Newtonian constitutive models: the generalized Newtonian fluid models and the viscoelastic fluid models. The generalized Newtonian fluid models are inelastic models, where the stress response is only dependent on the instantaneous rate of deformations. These fluid models can roughly represent the dynamics of polymeric liquids. For the viscoelastic models, the stress response depends on both the instantaneous shear rate and the history of the deformation. In this thesis, only viscoelastic models are used. Therefore, only several well-known viscoelastic fluid models are presented hereinafter.

(a) Oldroyd-B model

The Oldroyd-B model, originally proposed by Oldroyd [127], is one of the most useful and common models in modeling viscoelastic fluids. It was the first material frame-invariant phenomenological model describing the linear viscoelasticity of dilute polymer solutions. The functions in and in are given by

$$f(\mathbf{c}) = \mathbf{c} - \mathbf{I},\ g(\mathbf{c}) = \mathbf{c} - \mathbf{I}. \tag{2.9}$$

By assuming that the polymer molecules behave as a suspension of Hookean springs in a Newtonian solvent, the Oldroyd-B model can be derived from the kinetic theory [128]. The fundamental properties of viscoelasticity: stress relation, creep deformations, and a first normal stress difference are all included in the Oldroyd-B model.

(b) PTT model

The PTT model was derived by Phan-Thien and Tanner [129, 130] from the kinetic theory of an elastic network that represents a polymeric melt. The model makes the assumption that the average network extent affects the rates of junction generation and destruction. Due to the performance of the finite element method (FEM) and its precise prediction of the viscosity at a low shear rate, the PTT model is preferred in various polymer melt issues. The original evolution equation for the PTT model is as follows:

$$\frac{\partial \mathbf{c}}{\partial t} + \mathbf{u}\nabla \cdot \mathbf{c} - (1+\xi)\left(\mathbf{c}\cdot\nabla\mathbf{u}^T + \nabla\mathbf{u}\cdot\mathbf{c}\right) = -\frac{1}{\lambda} g(\mathbf{c}), \tag{2.10}$$

where ξ is the slip parameter of network.

The strain function is given as

$$f(\mathbf{c}) = \mathbf{c} - \mathbf{I}, \tag{2.11}$$

The relaxation function $g(\mathbf{c})$ is supposed to have a linear dependency on the trace of the conformation tensor in the original PTT model [129],

$$g(\mathbf{c}) = \left[1 + \varepsilon\left(\mathrm{tr}(c) - 3\right)\right](\mathbf{c} - \mathbf{I}), \tag{2.12}$$

Later, Phan-Thien and Tanner [130] derived a more accurate relaxation function:

$$g(\mathbf{c}) = \exp\left(\varepsilon \mathrm{tr}(\mathbf{c} - \mathbf{I})\right)(\mathbf{c} - \mathbf{I}). \tag{2.13}$$

Note that in Equation (2.5), the slip parameter of network $\xi = 0$, which is corresponding to the simplified PTT model.

(c) FENE model

Based on the kinetic theory of polymer chains behaving like non-linear elastic springs, the FENE (Finitely Extensible Nonlinear Elastic) models are adapted to describe the viscoelastic properties of the dilute polymeric solutions. The FENE family consists of the FENE-P model derived by Bird et al. [131] using Peterlin's statistical average [132] as a closure approximation and the FENE-CR model by Chilcott et al. [133]. The FENE-P model possesses a finite extensibility and predicts a shear-thinning behavior, and the FENE-CR model eliminates the shear-rate dependency of the steady-state viscosity.

The FENE-P model is given as

$$f(\mathbf{c}) = g(\mathbf{c}) = \frac{\mathbf{c}}{1 - tr(\mathbf{c})/L^2} - \frac{\mathbf{I}}{1 - 3/L^2}. \tag{2.14}$$

The FENE-CR model is given as

$$f(\mathbf{c}) = g(\mathbf{c}) = \frac{\mathbf{c} - \mathbf{I}}{1 - tr(\mathbf{c})/L^2} \tag{2.15}$$

(d) Giesekus model

A constitutive model for concentrated polymer solutions was developed by Giesekus [134, 135] with the addition of quadratic components of the stress, which may be seen as the result of anisotropic hydrodynamic drag brought on by the interactions between polymers. The functions $f(\mathbf{c})$ and $g(\mathbf{c})$ are given as

$$f(\mathbf{c}) = \mathbf{c} - \mathbf{I}, \tag{2.16}$$

$$g(\mathbf{c}) = \alpha\mathbf{c}^2 + (1 - 2\alpha)\mathbf{c} - (1 - \alpha)\mathbf{I}, \tag{2.17}$$

where the dimensionless parameter α is between 0 and 0.5, which quantifies the effect of the anisotropic stretching.

2.1.2 The log-conformation representation

In the present work, the log-conformation representation of Fattal and Kupferman [54] is adapted to solve the HWNP. The log-conformation representation consists in the utilization of a new variable $\boldsymbol{\Theta}$, the matrix-logarithm of the conformation tensor in the constitutive model

$$\boldsymbol{\Theta} = \log \mathbf{c}. \tag{2.18}$$

The velocity gradient $\nabla \mathbf{u}$ can be decomposed into the following according to Fattal and Kupferman [54]

$$\nabla \mathbf{u} = \boldsymbol{\Omega} + \mathbf{B} + \mathbf{N}\mathbf{c}^{-1}, \tag{2.19}$$

where $\boldsymbol{\Omega}$ and $\mathbf{N}$ are anti-symmetric matrices, and $\mathbf{B}$ is a symmetric traceless matrix. The matrices $\boldsymbol{\Omega}$, $\mathbf{B}$, and $\mathbf{N}$ can be derived by the projection of the velocity gradient into the principal base of the stress tensor. The velocity gradient is changed as

$$\mathbf{R}^T \nabla \mathbf{u} \mathbf{R} = \begin{pmatrix} m_{11} & m_{12} \\ m_{21} & m_{22} \end{pmatrix} \tag{2.20}$$

The conformation tensor in the eigen decomposition form for in a two-dimensional problem is written as

$$\mathbf{c} = \mathbf{R} \begin{pmatrix} \lambda_1 & 0 \\ 0 & \lambda_2 \end{pmatrix} \mathbf{R}^T, \tag{2.21}$$

where λ_1 and λ_2 are the eigenvalues and $\mathbf{R}$ is the orthogonal matrix of the conformation tensor containing the eigenvectors. And the decomposed tensors can be written as

$$\boldsymbol{\Omega} = \mathbf{R} \begin{pmatrix} 0 & \omega \\ -\omega & 0 \end{pmatrix} \mathbf{R}^T, \ \mathbf{B} = \mathbf{R} \begin{pmatrix} m_{11} & 0 \\ 0 & m_{22} \end{pmatrix} \mathbf{R}^T, \ \mathbf{N} = \mathbf{R} \begin{pmatrix} 0 & n \\ -n & 0 \end{pmatrix} \mathbf{R}^T, \tag{2.22}$$

where $\mathbf{R}$ is the orthogonal matrix of the conformation tensor containing the eigenvectors.

The calculation of λ_1, λ_2, m_{11}, m_{22}, ω and n are shown as follows. λ_1 and λ_2 are calculated from the characteristic equation of the conformation tensor **c**

$$\det\left(\mathbf{c}-\lambda_i\mathbf{I}\right)=0. \tag{2.23}$$

The expansion of the characteristic equation yields

$$\lambda_i^2+b\lambda_i+d=0, \tag{2.24}$$

where b and d can be expressed by the components of **c** as

$$b=-c_{11}-c_{22},\ d=-\det\left(\mathbf{c}\right). \tag{2.25}$$

The eigenvalues can be expressed by the coefficients b and d using the quadratic formula as

$$\lambda_{1,2}=\frac{-b\pm\sqrt{b^2-4d}}{2}. \tag{2.26}$$

Then the eigen vectors corresponding to the above eigenvalues can be calculated by solving the algebraic equation

$$\left(\mathbf{c}-\lambda_i\mathbf{I}\right)\mathbf{e}_i=\mathbf{0}, \tag{2.27}$$

which yields

$$\mathbf{e}_i=\left[\frac{c_{12}}{\sqrt{c_{12}^2+\left(\lambda_i-c_{11}\right)^2}},\frac{\lambda_i-c_{11}}{\sqrt{c_{12}^2+\left(\lambda_i-c_{11}\right)^2}}\right]. \tag{2.28}$$

Then the decomposition Equation (2.20) becomes

$$\mathbf{R}^{\mathrm{T}}\nabla\mathbf{u}\mathbf{R}=\mathbf{R}^{\mathrm{T}}\mathbf{\Omega}\mathbf{R}+\mathbf{R}^{\mathrm{T}}\mathbf{B}\mathbf{R}+\mathbf{R}^{\mathrm{T}}\mathbf{N}\mathbf{c}^{-1}\mathbf{R}. \tag{2.29}$$

Then substituting Equations (2.20), (2.21), and (2.22) into Equation (2.29) yields

$$\begin{pmatrix}m_{11}&m_{12}\\m_{21}&m_{22}\end{pmatrix}=\begin{pmatrix}0&\omega\\-\omega&0\end{pmatrix}+\begin{pmatrix}m_{11}&0\\0&m_{22}\end{pmatrix}+\begin{pmatrix}0&n\\-n&0\end{pmatrix}\begin{pmatrix}\lambda_1&0\\0&\lambda_2\end{pmatrix}^{-1}, \tag{2.30}$$

which can be simplified as

$$\begin{pmatrix} 0 & m_{12} \\ m_{21} & 0 \end{pmatrix} = \begin{pmatrix} 0 & \omega + \dfrac{n}{\lambda_2} \\ -\omega - \dfrac{n}{\lambda_1} & 0 \end{pmatrix}. \tag{2.31}$$

From Equation (2.31) the following equations are obtained

$$\begin{aligned} \omega &= \frac{\lambda_2 m_{12} + \lambda_1 m_{21}}{\lambda_2 - \lambda_1}, \\ n &= \lambda_1 \lambda_2 \frac{m_{12} + m_{21}}{\lambda_2 - \lambda_1}, \end{aligned} \tag{2.32}$$

The calculation for three-dimensional problems is described in Appendix A.

Substituting Equation (2.29) into Equation (2.10) finally yields the following evolution equation for the log-conformation tensor:

$$\frac{\partial \boldsymbol{\Theta}}{\partial t} + (\mathbf{u} \cdot \nabla)\boldsymbol{\Theta} - (\boldsymbol{\Omega}\boldsymbol{\Theta} - \boldsymbol{\Theta}\boldsymbol{\Omega}) - 2\mathbf{B} = -\frac{1}{\lambda} \exp(-\boldsymbol{\Theta})\, g\left[\exp(\boldsymbol{\Theta})\right]. \tag{2.33}$$

In summary, the viscoelastic fluid solver solves the Equation (2.33) and recovers the conformation tensor with the matrix-exponential of ψ:

$$\mathbf{c} = \exp(\boldsymbol{\psi}). \tag{2.34}$$

The conformation tensor's symmetric positive definiteness is enforced by construction in Equation (2.34). Be aware that the matrix-logarithm and matrix-exponential are tensor operations, where the logarithm and exponent are applied to a tensor's eigenvalues, respectively:

$$\log(\mathbf{c}) \equiv \mathbf{R} \begin{pmatrix} \log \lambda_1 & 0 \\ 0 & \log \lambda_2 \end{pmatrix} \mathbf{R}^{\mathrm{T}}. \tag{2.35}$$

2.2 Finite volume method

Due to the complexity and high nonlinearity of the above differential equations, most problems cannot be solved analytically. Therefore, numerical procedures are required to solve the set of partial differential equations. Several numerical methods have been widely used in computational

fluid dynamics (CFD), such as finite difference (FDM) [136, 137], finite element method (FEM) [138], and finite volume method (FVM) [139-141]. The popularity of FVM in CFD stems from some special properties of the method. First, because terms in the conservation equations are evaluated using face fluxes throughout each unique control volume and because the flux conservation is maintained in a particular volume, the FVM is rigorously conservative. Additionally, the FVM offers high flexibility as a discretization method due to the discretization in the space domain is carried out directly in physical space with no need for any transformation between the physical and computational coordinate systems. Furthermore, because of the adoption of a collocated arrangement [142], the FVM may be used to solve flows in complicated geometries. These advancements have increased the FVM's usefulness while maintaining the FVM's straightforward mathematical formulation across a broad range of applications. Another crucial aspect of the FVM is that it mirrors the physics and the conservation principles it models, such as the integral property of the governing equations and the features of the terms it discretizes. Since the first application of the FVM in the study of the classical benchmark problem of viscoelastic fluid flows past a cylinder by Hu et al. [143], the FVM has been extensively used in the study of the viscoelastic fluid problems [144-146], especially with the implementation of the log-conformation reformulation in the framework of the FVM. In the present study, the FVM is adopted to transform the governing equations into a system of linear algebraic equations.

As seen in Figure 2.2, in the FVM, the space domain is subdivided into finite non-overlapping volumes, and V_{n} represents an arbitrary volume. The volume V_{n} is enclosed by surface S consisting of several segments named by $S_i\,(i=1,2,...)$. $\mathbf{n}_{S_i}$ denotes the normal vector of the volume on segment S_i directing outward from the volume.

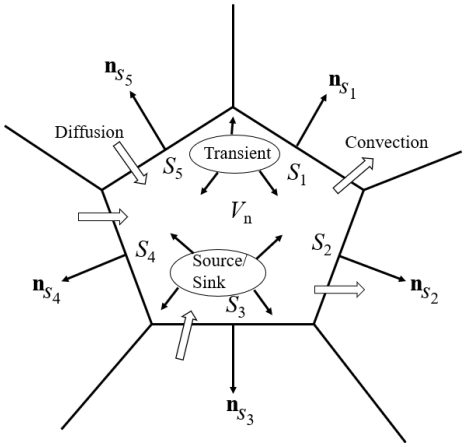

Figure 2.2 Schematic of the discrete cell in the FVM.

By integrating the momentum equation over the volume V_n shown in Figure 2.2, Equation (2.2) is transformed to

$$\int_{V_n} \rho \frac{\partial \mathbf{u}}{\partial t} dV + \int_{V_n} \rho \mathbf{u} \cdot \nabla \mathbf{u} dV - \int_{V_n} \eta_s \nabla^2 \mathbf{u} dV = -\int_{V_n} \nabla p dV + \int_{V_n} \nabla \cdot f(\mathbf{c}) dV + \int_{V_n} \mathbf{F} dV, \tag{2.36}$$

On the left-hand side of the above equation, the three terms represent the temporal term, convection term, and diffusion term, respectively. The time domain is divided into discrete times $t_0, t_1, \ldots, t_n, t_{n+1} \ldots$ with time step $\Delta t = t_{n+1} - t_n$. Then the time derivative term can be discretized with the first-order accurate Euler method as

$$\int_{V_n} \frac{\partial \mathbf{u}}{\partial t} dV = \frac{\mathbf{u}_{n+1} - \mathbf{u}_n}{\Delta t} V_n, \tag{2.37}$$

Two types of Euler method are available depending on the evaluation of other terms in the equation, including implicit method with the term evaluated at t_{n+1}, and explicit method with the term evaluated at t_n. The discretization of the convection term and the diffusion term is done by applying the divergence theorem, which replaces the volume integrals by the surface integrals as

$$\int_{V_n} \rho \mathbf{u} \cdot \nabla \mathbf{u} dV = \int_{V_n} \rho \nabla \cdot \mathbf{u}\mathbf{u} dV = \int_S \rho \mathbf{u}\mathbf{u} \cdot \mathbf{n} dS = \sum_i J_{S_i}^C \mathbf{u}, \tag{2.38}$$

where $J_{S_i}^C$ represents the convection flux over the volume surface. Note that the velocity field **u** varies on the faces of the volume where the summation happens, therefore an approximation of **u** on the faces is needed such that the velocity variation within the volume is included. Various schemes have been developed and applied successfully to the convection discretization, such as the first-order accurate upwind scheme and the second-order accurate central differencing scheme. The diffusion term is discretized as follows

$$-\int_{V_n} \eta_s \nabla^2 \mathbf{u} dV = -\int_S (\eta_s \nabla \mathbf{u}) \cdot \mathbf{n} dS = -\sum_i \eta_s \nabla \mathbf{u} \cdot \mathbf{n}_{S_i} \tag{2.39}$$

The second-order accurate linear scheme can be used to discretize the diffusion term.

On the right-hand side of Equation (2.36), the remaining terms are generally referred as source terms. The treatment of source terms is described as follows

$$-\int_{V_n} \nabla p dV + \int_{V_n} \nabla \cdot f(\mathbf{c}) dV + \int_{V_n} \mathbf{F} dV = \int_{V_n} R(\mathbf{u}) dV. \tag{2.40}$$

The source term $R(\mathbf{u})$ is linearized as $R(\mathbf{u}) = R_0 + R_1 \mathbf{u}$, and the source terms can be treated as

$$-\int_{V_n} \nabla p dV + \int_{V_n} \nabla \cdot f(\mathbf{c}) dV + \int_{V_n} \mathbf{F} dV = R_0 V_n + R_1 \mathbf{u}_n V_n, \tag{2.41}$$

where $\mathbf{u}_n$ is the velocity field evaluated at the volume V_n. Other equations in the system can also be discretized similarly as the momentum equation. Then the set of differential equations are converted to a system of algebraic equations, which can be solved by the algebraic operations.

2.3 Numerical implementation in OpenFOAM

OpenFOAM (Open Source Field Operation and Manipulation) is a powerful FVM-based CFD software and has found widespread use in engineering and science fields due to its ability to implement intricate mathematical models and provide parallel computing. Moreover, OpenFOAM

is distributed with a large set of precompiled applications (solvers) and allows users to create their own or modify existing ones. A variety of solvers for many common classical issues, including compressible flows, incompressible flows, multiphase flows, heat transfer, combustion, etc. OpenFOAM also includes useful meshing tools for the generation of different types of mesh, such as blockMesh for structural 2D and 3D mesh, and cfMesh and snappyHexMesh for hex-dominant mesh. Additionally, OpenFOAM offers easy mesh conversion from frequently used meshing software, such as ANSYS, Fluent, Pointwise, Salome, etc.

The numerical simulations in this thesis are performed using a viscoelastic fluid solver implemented in OpenFOAM. Programmed using the C++ language, OpenFOAM solvers are organized using a standard convention that the source code of each application is stored in a directory with the name as the name of the solver. The top level source file then takes the solver name with the .C extension. For example, the structure of a solver named as newSolver is shown in Figure 2.3. The source code of the solver is in a directory newSolver, where three parts can be found, including the top level file named as newSolver.C, the header file name as otherHeader.H, and a subdirectory named as make for compilation.

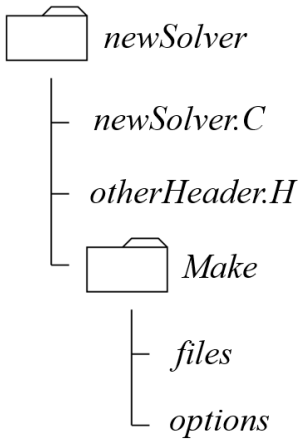

Figure 2.3 Directory structure for a solver named as newSolver.

2.3.1 Viscoelastic fluid solver in OpenFOAM

The library and viscoelastic fluid solver (*viscoelasticFluidFoam*) created by Favero et al. [147] in OpenFOAM provides a variety of constitutive equations to model viscoelastic fluids. However, *viscoelasticFluidFoam* presents stability issues for some high Weissenberg number problems. Recently, Pimenta and Alves [148] optimized *viscoelasticFluidFoam* and created *rheoTool* by modifying some critical points minimizing the stability issues. In *rheoTool*, Pimenta and Alves [149, 150] implemented coupled solvers for simulating electrically-driven flows and tested the solvers in benchmark flows. In the present study, the electroosmotic flow of viscoelastic fluids is numerically solved by the solver *rheoEFoam* implemented in *rheoTool*.

2.3.2 The both-sides-diffusion (BSD) technique

The both-sides-diffusion technique consists in adding a diffusive term on both sides of momentum equation with the one on the left-hand side added implicitly and the one on the right-hand side explicitly. Both added terms will cancel each other once the steady state is reached. This method has a stabilizing effect by increasing the ellipticity of the momentum equation. Incorporating the terms arising from the both-sides-diffusion in the momentum equation, then

$$\rho\left(\frac{\partial \mathbf{u}}{\partial t}+\mathbf{u}\cdot\nabla\mathbf{u}\right)-\nabla\cdot\left(\eta_s+\eta_p\right)\nabla\mathbf{u}=-\nabla p-\nabla\cdot\left(\eta_p\nabla\mathbf{u}\right)+\nabla\cdot\boldsymbol{\tau}+\mathbf{F} \tag{2.42}$$

It should be noted that the additional diffusive terms are scaled by the polymeric viscosity η_p, which is an optional but popular choice in the literature [151].

2.3.3 Coupling algorithms

In the OpenFOAM toolbox, most solvers use segregated solutions to solve linear systems of equations in a coupled way, where the equations for each variable are solved sequentially. However, even for a fully implicit method, the coupling between variables is weak, resulting in the occurrence of numerical divergence. For pressure-velocity coupling, the SIMPLE and

SIMPLEC algorithms are commonly used in steady-state solvers, and the PISO and PIMPLE algorithms are commonly used in transient solvers. Pimenta and Alves [148] investigated the SIMPLEC algorithm in solving transient viscoelastic fluid flows at low Reynolds numbers and great stability and accuracy were obtained. The continuity equation derived for SIMPLEC yields [148]

$$\nabla\cdot\left(\frac{1}{a_P-H_1}\left(\nabla p\right)_p\right)=\nabla\cdot\left[\frac{\mathbf{H}}{a_P}+\left(\frac{1}{a_P-H_1}-\frac{1}{a_P}\right)\left(\nabla p^*\right)_P\right] \tag{2.43}$$

where a_p are the diagonal coefficients from the momentum equation, $H_1=-\sum_{nb}a_{nb}$ is an operator representing the negative sum of the off-diagonal coefficients from momentum equation, $\mathbf{H}=-\sum_{nb}a_{nb}\mathbf{u}_{nb}^*+\mathbf{b}$ is an operator containing the off-diagonal contributions, plus the source terms (except the pressure gradient) of the momentum equation and p^* is the pressure field known from the previous time-step. After obtaining the continuity-compliant pressure field, the velocity is then corrected by following equation

$$\mathbf{u}=\frac{\mathbf{H}}{a_p}+\left(\frac{1}{a_p-H_1}-\frac{1}{a_p}\right)\left(\nabla p^*\right)_p-\frac{1}{a_p-H_1}\left(\nabla p\right)_p \tag{2.44}$$

Same as the pressure-velocity coupling problem, the stress-velocity decoupling problems lead to the similar numerical challenges. In the interpolation from cell-centered to face-centered fields, cell-centered velocity tends to lose the influence of the forces of its neighborhood cells. Such forces can be pressure gradient or the polymeric extra-stress. In the case of polymeric extra-stresses, it is the divergence term ($\nabla\cdot\boldsymbol{\tau}$) in the momentum equation accounting for the decoupling when $\boldsymbol{\tau}$ is linearly interpolated from cell centers to face centers. Pimenta and Alves [148] described a new stress-velocity coupling method as follows

$$\boldsymbol{\tau}_f = \overline{\boldsymbol{\tau}}_f + \eta_p \left[\left(\nabla \mathbf{u} \mid_f + \left(\nabla \mathbf{u} \right)^T \mid_f \right) - \left(\overline{\nabla \mathbf{u}} \mid_f + \overline{\left(\nabla \mathbf{u} \right)^T} \mid_f \right) \right], \tag{2.45}$$

where the terms with an overbar are linearly interpolated from cell-centered values, and the remaining velocity gradients are directly evaluated from the cell-centered velocities standing the face. Substituting the definition of into the momentum equation with the both-sides-diffusion terms yields

$$\rho \left(\frac{\partial \mathbf{u}}{\partial t} + \mathbf{u} \cdot \nabla \mathbf{u} \right) - \nabla \cdot \left(\eta_s + \eta_p \right) \nabla \mathbf{u} = -\nabla p - \overline{\nabla \cdot \eta_p \nabla \mathbf{u}} + \nabla \cdot \overline{\boldsymbol{\tau}} + \mathbf{F}. \tag{2.46}$$

2.3.4 Overview of the algorithm

In the solver rheoEFoam, the coupling between the pressure and velocity fields is ensured by the SIMPLEC algorithm and an inner-iteration loop is used to reduce the explicitness of the method and to increase its accuracy and stability. The sequence adopted in the rheoEFoam solving the differential equations consists of the following steps [148]:

Step 1. Initialize the fields $\{\mathbf{u}, p, \boldsymbol{\tau}, \phi_{\text{Ext}}, \psi, \boldsymbol{\Theta}\}_0$ and time $(t = 0)$.

Step 1.1. Compute steady state ϕ_{Ext} and ψ.

Step 2. Enter the time loop $(t = \Delta t)$.

Step 2.1. Enter the inner iteration loop $(i = 0)$.

Step 2.1.1. Compute $\boldsymbol{\Theta}_i$ and $\boldsymbol{\tau}_i$ by log-conformation method.

Step 2.1.2. Compute estimated velocity field $\mathbf{u}_i^*$ by solving the momentum equation.

Step 2.1.3. Compute pressure field by enforcing the continuity equation.

Step 2.1.4. Correct the previously estimated velocity field using the correct pressure field.

Step 2.1.5. Increase the inner iteration index and repeat the computation from Step 2.1.1, until the inner iteration criteria (i.e., maximum tolerance) is satisfied.

Step 2.1.6. Set $\left\{\mathbf{u}, p, \boldsymbol{\tau}, \phi_{\text{Ext}}, \psi, \boldsymbol{\Theta}\right\}_t = \left\{\mathbf{u}_i, p_i, \boldsymbol{\tau}_i, \phi_{\text{Ext}_i}, \psi_i, \boldsymbol{\Theta}_i\right\}_t$.

Step 2.2. Increase time, $t = t + \Delta t$, and return to Step 2.1 until the simulation time is reached.

Step 3. Stop the simulation and exit.

CHAPTER 3

ELECTROOSMOTIC FLOW OF VISCOELASTIC FLUID THROUGH A CONSTRICTION MICROCHANNEL

3.1 Introduction

The EOF of viscoelastic fluid through a 10:1 constriction microfluidic channel connecting two reservoirs on either side is numerically investigated. The flow is modeled by the Oldroyd-B (OB) model coupled with the Poisson-Boltzmann (PB) model. EOF of polyacrylamide (PAA) solution is studied as a function of the PAA concentration and the applied electric field. In contrast to the steady EOF of Newtonian fluid, the EOF of PAA solution becomes unstable when the applied electric field (PAA concentration) exceeds a critical value for a fixed PAA concentration (electric field), and vortices form at the upstream of the constriction. EOF velocity of viscoelastic fluid becomes spatially and temporally dependent, and the velocity at the exit of the constriction microchannel is much higher than that at its entrance, which is in qualitative agreement with the experimental observation from the literature. Under the same apparent viscosity, the time-averaged velocity of the viscoelastic fluid is lower than that of the Newtonian fluid.

The existing studies of EOF have been mainly focusing on Newtonian fluids [152, 153]. However, in reality, EOF has been widely used to control and manipulate biological fluids (i.e., blood, saliva, lymph, protein, and DNA solutions) [154-156] and polymeric solution [156], which exhibit non-Newtonian characteristics. Therefore, investigating the EOF of viscoelastic fluids is of practical importance. Bello et al. [157] conducted the pioneering study on the EOF of non-Newtonian fluid and measured the EOF velocity of methyl cellulose solution in a capillary. Their results show that the EOF velocity of such polymer solutions is much higher than that predicted with the classic Helmholtz-Smoluchowski velocity. Chang and Tsao [158] conducted similar

experiments and found the effective viscosity decreased because of the sheared polymeric molecules inside the electrical double layer (EDL). Theoretically, non-Newtonian effects can be characterized by proper constitutive models relating the dynamic viscosity and the rate of shear. Such constitutive models include power-law model [159], Carreau model [104], WhiteMetzner model [160], Bingham model [107], Oldroyd-B model [127], PTT model [129], Moldflow second-order model [161], Giesekus model [162], etc. Das and Chakraborty [112] developed an approximate solution for the EOF velocity of power-law fluid between two parallel plates. Zhao et al. [110, 116] derived a generalized Helmholtz-Smoluchowski velocity for the EOF of power-law fluid in a slit microchannel. Later, Zhao and Yang [163, 164] extended the study to a cylindrical microcapillary. Olivares et al. [115] experimentally investigated EOF of a non-Newtonian polymeric solution and verified the generalized Helmholtz-Smoluchowski velocity. Tang et al. [165] numerically investigated EOF of a power-law fluid using Lattice-Boltzmann method. Zimmerman et al. [104] carried out a numerical simulation of EOF of Carreau fluid in a T-junction microchannel and found that the flow field significantly depended on the non-Newtonian characteristics of the fluid. The aforementioned studies on EOF of non-Newtonian fluid are limited to inelastic constitutive models (i.e., power-law and Carreau models). However, some fluids show both viscous and elastic behaviors, which can be presented by viscoelastic constitutive models. There is existing literature investigating the characteristic of EOF of viscoelastic fluids, showing that the viscoelasticity of the fluid affects the flow pattern and flow rate. Note that in the those studies, the EOF of non-Newtonian fluid was assumed to be in a steady state.

Recently, EOFs of non-Newtonian fluids have been reported to be time-dependent and show instabilities even at low Reynolds numbers. Such EOFs are time-dependent because of the nonlinear viscosity and elasticity of non-Newtonian fluids. Bryce and Freeman [166] first reported

the electro-elastic instability in EOF of PAA solutions through a 2:1:2 micro-scale contraction/expansion when the applied electric field exceeded a threshold value. Later, Bryce and Freeman [167] reported that such instabilities insignificantly enhanced the mixing in microflow. Pimenta and Alves [148, 168] later experimentally and numerically studied the electro-elastic instabilities of PAA solutions in both cross-slot and flow-focusing microdevices and found that mixing efficiency was not improved significantly. Song et al. [169] experimentally and numerically studied the elastic instability in EOF of viscoelastic polyethylene oxide (PEO) solutions through T-shaped microchannels. The results demonstrated that the threshold electric field for the onset of instability highly depended on the PEO concentration. Song et al. [170] later extended the work by experimentally investigating the fluid rheological effects on the elastic instability in EOF of six types of phosphate buffer-based aqueous solutions through T-shaped microchannels. They found that shear thinning effect of the fluid might account for the electro-elastic instabilities. However, the fluid with high elasticity alone did not have instability, which is inconsistent with the results of Pimenta [168]. The authors attribute the inconsistency to the neglect of microstructural effects. (e.g., polymer-wall interaction and electric effect on the molecular structure of the polymer, etc.) of shear-thinning polymer solutions. However, this experimental result shows similarity to the work of Ko et al. [171], in which weakly shear-thinning, viscoelastic polyvinylpyrrolidone (PVP) and PEO solutions exhibited Newtonian-like EOF patterns. In contrast, shear-thinning and weakly elastic xanthan gum (XG) solution exhibited disturbance and vortices, suggesting that fluid elasticity alone has an insignificant impact on the steady-state EOF pattern. More recently, Sadek [172] experimentally investigated EOF of viscoelastic fluids through different microchannel configurations, including hyperbolic-shaped contractions followed by an

abrupt expansion, and abrupt contractions followed by a hyperbolic-shaped expansion. EOF showed instabilities of elastic origin at very low Weissenberg numbers (*Wi*) (i.e., $Wi < 0.01$).

There is only limited literature on numerical studies of electro-elastic instabilities. Afonso et al. [173] numerically investigated the elastic instability of EOF through a cross-slot geometry using the upper-converted Maxwell and the simplified Phan-Thien-Tanner models, and a direct flow transition from steady symmetric state to unsteady flow without crossing the steady asymmetric state at a critical *Wi* was observed. Pimenta and Alves [168] numerically investigated the electro-elastic instabilities in cross-slot and flow-focusing micro devices using OB model and PB model. They found that the strong shear-dominated flow within the EDL at the corners had a more significant contribution to the elastic instabilities than the extensionally dominated bulk flow. Song et al. [169] numerically investigated EOF of PEO solution through a T-shaped microchannel. Their model considered only the influence of PEO solution on the fluid viscosity, conductivity, and zeta potential. Due to the neglect of fluid elasticity effect in the mathematical model, only the electrokinetic flow phenomena of dilute PEO solution (i.e., ≤ 750 ppm) were captured.

Both experimental and numerical investigations in the EOF instabilities of viscoelastic fluid are limited, and the conditions proposed by various researchers for triggering the instabilities in the EOF of viscoelastic fluids show inconsistency and remain unclear. Inspired by the existing literature, in this chapter, we numerically study the EOF of viscoelastic fluids in a constriction microchannel, which is close to an actual microfluidic device.

3.2 Mathematical Model and Geometry

We consider incompressible monovalent binary electrolyte solution such as KCL with bulk concentration c_0 mixed with PAA polymer solution of concentration c_p, which fills a microchannel of height H_C, length L_C, and width w connecting two identical reservoirs of height H_r and length

L_r on either side. The solid walls of the constriction microchannel and the reservoirs are assumed to carry a constant negative zeta potential, ζ_0. When dealing with non-Newtonian fluids, constant zeta potential has been widely accepted [174]. Huang et al. [174] compared theoretical and experimental results of PEO solutions, and constant zeta potential was proven for various PEO concentrations. Therefore, in the current study, the effect of the polymer concentration on the wall zeta potential is neglected. Two electrodes are placed at both ends of the reservoirs, and an external potential bias U_0 is applied between the inlet (Anode) and outlet (Cathode). Through the interaction between the externally applied electric field and net charges accumulated within the EDL in the vicinity of the charged walls, EOF flowing from the anode reservoir through the constriction microchannel towards the cathode reservoir is generated. The apparent electric field between the inlet and outlet is defined as $E_{app} = U_0/(2L_r + L_C)$. In some applications, there are slit microchannels with width much larger than height [175, 176]. For example, two-phase flow patterns were studied in a microchannel with 10-mm width and 50-μm height [175]. For microchannels with such geometries, the flow can be simplified to a 2D problem [177]. Therefore, in the current study, the channel width is assumed to be much larger than the channel height, and the flow can be simplified to a 2D problem, as schematically shown in Figure 3.1. A Cartesian coordinate system with the origin fixed at the center of the microchannel is adopted with the *x*-axis along the length direction and the *y*-axis in the height direction.

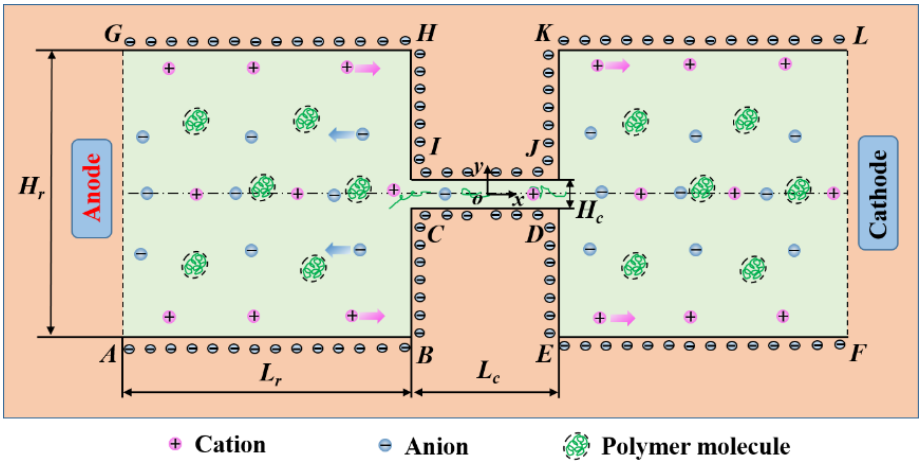

Figure 3.1 Schematic diagram of a constriction microchannel connecting two reservoirs at both ends. The solid walls of reservoirs and the constriction channel are negatively charged, and an electric field is imposed by applying a potential difference between anode and cathode positioned in two reservoirs.

The governing equations are same as introduced in Chapter 2. To numerically solve the coupled equations, CUBISTA scheme [178] is used to discretize the convective terms and central differences are used for the discretization of Laplacian and gradient terms. The time derivatives are discretized with three-time level explicit difference scheme [179], which is of the second order accuracy. The exponential source term is linearized using Taylor expansion up to the second term [180]. All the terms in the momentum equation, except the pressure gradient and the electric contribution, are discretized implicitly. A small time-step, $\Delta t = \lambda/10^5$, is used to ensure accuracy. The well-known SIMPLEC (Semi-Implicit Method for Pressure-Linked Equations-Consistent) algorithm [181] is used to resolve the velocity-pressure coupling. The pressure field is computed by PCG (Preconditioned Conjugate Gradient) solver, of which the tolerance and maximum iteration are set to be 1×10^{-8} and 800, respectively. The velocity field is computed by PBiCG (Preconditioned Biconjugate Gradient) solver, of which the tolerance and the maximum iteration

are set to be 1×10^{-10} and 1000, respectively. The above numerical methods are listed in Appendix B. As shown in Figure 3.2, the boundary conditions are given as follows:

(1) At the Anode (edge AG in Figure 3.2): $\mathbf{n}\cdot\nabla\mathbf{u} = 0$; $p = 0$; $\boldsymbol{\tau} = 0$; $\phi_{\text{Ext}} = U_0$; $\mathbf{n}\cdot\nabla\psi = 0$; $\boldsymbol{\Theta} = \mathbf{0}$; where $\mathbf{n}$ denotes the normal unit vector on the surface.

(2) At the Cathode (edge FL in Figure 3.2): $\mathbf{n}\cdot\nabla\mathbf{u} = 0$; $\mathbf{n}\cdot\nabla\boldsymbol{\tau} = 0$; $\phi_{\text{Ext}} = 0$; $\mathbf{n}\cdot\nabla\psi = 0$; $\mathbf{n}\cdot\nabla\boldsymbol{\Theta} = 0$.

(3) On the reservoir walls (edges ABC, DEF, GHI, and JKL in Figure 3.2) and the microchannel walls (Edges CD and IJ in Figure 3.2): $\mathbf{u} = \mathbf{0}$; $\mathbf{n}\cdot\nabla\phi_{\text{Ext}} = 0$; $\psi = \xi_0$; $\mathbf{n}\cdot\nabla\boldsymbol{\Theta} = 0$; $\mathbf{n}\cdot\nabla p$ is obtained from the momentum equation; the components of $\boldsymbol{\tau}$ are linearly extrapolated.

The following initial conditions are specified within the domain: $\mathbf{u} = \mathbf{0}$; $p = 0$; $\boldsymbol{\tau} = \mathbf{0}$; $\phi_{\text{Ext}} = 0$; $\psi = 0$; $\boldsymbol{\Theta} = \mathbf{0}$.

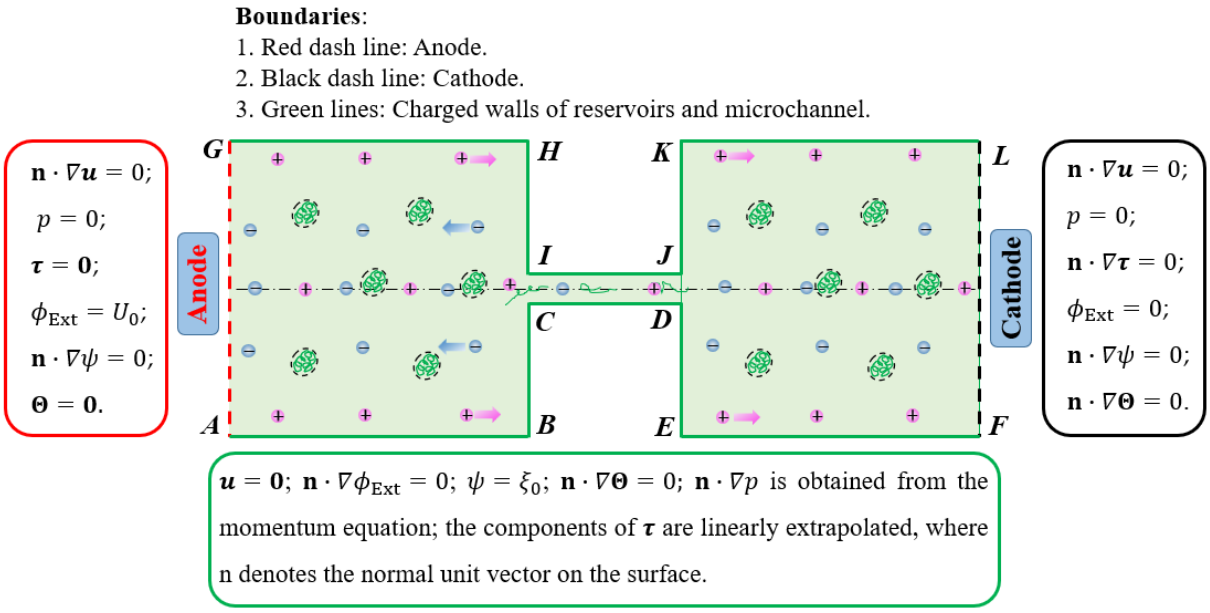

Figure 3.2. Boundary conditions with $\mathbf{n}$ denoting the normal unit vector on the surface.

Structural mesh is adopted to discretize the computational domain. 90° corners of the contraction channel (points I, J, C, and D in Figure 3.1) are smoothed by a fillet of a 1 μm in radius

to avoid sharp turns. The 90° corners of the reservoirs (points H, K, B, and E in Figure 3.1) are smoothed by a fillet of 2 μm in radius. To capture the EDL in the vicinity of the charged walls, a finer mesh is distributed near the charged reservoir and channel walls as shown in Figure 3.3. To reduce the number of mesh, a relatively low bulk concentration c_0 = 0.01 mM is used, and the EDL thickness is 95 nm in this study. There are 77192 cells in the mesh.

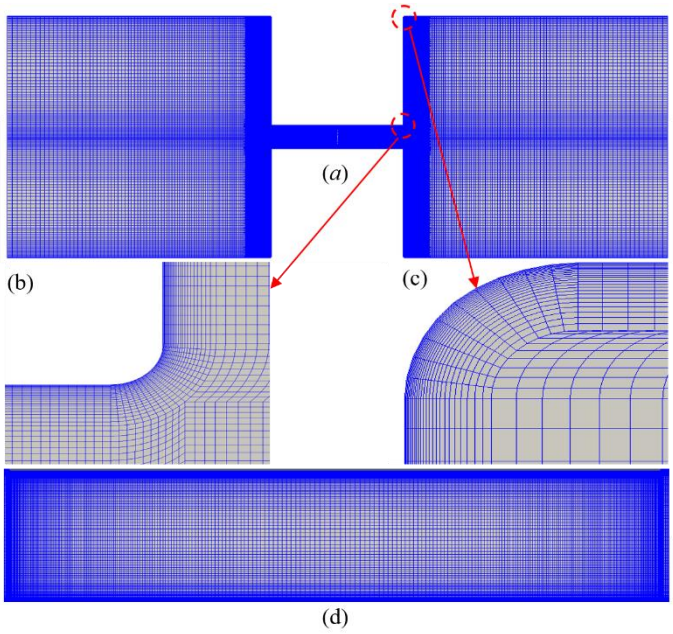

Figure 3.3 Computational mesh used in the numerical simulations. Mesh of the whole geometry (a) and detailed view of the mesh at channel corner (b), at reservoir corner (c), and in the constriction microchannel (d).

3.3 Code Validation of *rheoEFoam*

In this work, η_p and λ for 100 ppm, 250 ppm, and 1000 ppm PAA-water solutions are adopted to accomplish curve fitting as shown in Figure 3.4. The values of η_p and λ were experimentally measured, and the slow retraction method was used to measure the relaxation time. The polymer dynamic viscosity can be expressed as $\eta_p = 2.22\times10^{-5}\cdot c_p$, and the relaxation time can be expressed

as $\lambda = 3.69\times10^{-3} + 3.9422\times10^{-5}\cdot c_p^2$, where c_p represents the weight concentration of PAA solution with the unit of ppm. The η_p and λ for other studied in this work are estimated by the curve-fitting expressions.

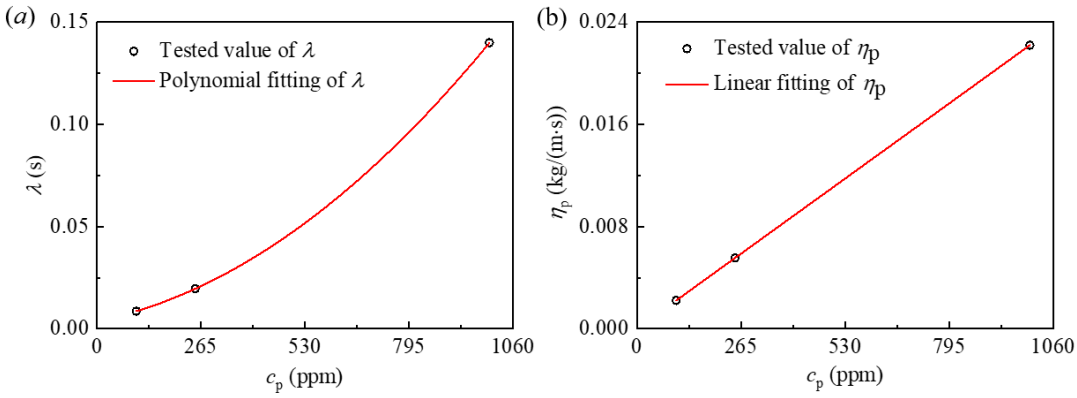

Figure 3.4 (a) Polymer dynamic viscosity η_p and (b) relaxation time λ as a function of the polyacrylamide (PAA) concentration, c_p.

In a microfluidic channel with EDL thickness much smaller than the channel height, the EOF velocity of a Newtonian fluid can be approximated by the Helmholtz-Smoluchowski velocity formula [181],

$$u_0 = -\frac{\varepsilon\xi_0 E_x}{\eta_0}, \tag{3.1}$$

Where E_x is the actual local electric field in the mainstream direction and is the total viscosity η_0 of the fluid. To check the accuracy of the code, both the Newtonian and viscoelastic fluids in the same geometry with H_C = 40 μm, L_C = 200 μm, H_r = 400 μm, and L_r = 400 μm. Other parameters are set as U_0 = 60 V, ξ_0 = −0.11 V [182], and $\varepsilon = 6.906266\times10^{-10}$ F·m^{-1}. For Newtonian fluid, the total viscosity is set as $\eta_0 = \eta_s$ = 0.00322 kg/(m·s). When the concentration of PAA solution is less than 2 ppm, the relaxation time is less than 0.1 ms [183], and the fluid can be

approximately treated as Newtonian fluid. Therefore, for the OB model, parameters are set as η_s = 0.00317 kg/(m·s), η_p = 0.00005 kg/(m·s), $\eta_0 = \eta_s + \eta_p$ = 0.00322 kg/(m·s), and λ = 0.1 ms. Figure 3.5a depicts electric potential $\phi_{Ext}(x,0)$ along the x-axis when E_{app} = 600 V/cm. The electric field in the x-direction, $-\frac{\partial \phi_{Ext}}{\partial x}$, in the constriction microchannel is 1820 V/cm, which is about 10 times of the electric field in the reservoirs. This is because of the 10:1:10 contraction geometry and current conservation. With the same electric conductivity, the electric field is inversely proportional to the cross-sectional area of the geometry. Note that the actual electric field within the constriction microchannel is about three times of the apparent electric field, E_{app}, which does not consider the cross-sectional variation of the geometry. EOFs of both Newtonian fluid and viscoelastic fluid reach a steady state. Figure 3.5b shows the x-component velocity profiles, $u(0,y)$, of the Newtonian fluid (solid line) and the OB model (circles). The velocity first rises rapidly within the thickness of EDL, then reaches a plateau in the cross section of the channel. When E_x = 1820 V/cm, the calculated Helmholtz-Smoluchowski velocity is 4.29 mm/s, and the velocity at the center of the channel is 4.27 mm/s for both Newtonian and OB models. The relative difference between the approximated velocity and the simulated velocity is less than 0.5%. In addition, the result for OB model matches that of Newtonian fluid. Such consistency between Newtonian model and OB model matches that of Newtonian fluid. Such consistency between Newtonian model and OB model is because the polymer dynamic viscosity η_p is much smaller than the solvent dynamic viscosity η_s, and the relaxation time of the polymer λ is also tiny. Under the considered condition, the elastic effect of the fluid is negligible, and the OB fluid is almost the same as Newtonian fluid with the same total viscosity.

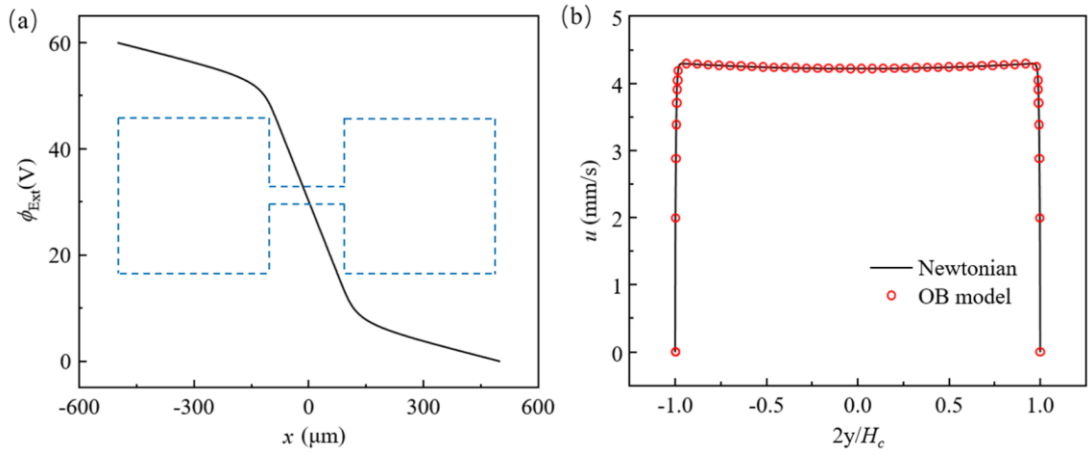

Figure 3.5 (a) Electric potential distribution (blue dash line shows the relative position of the geometry) along the *x*-axis, (b) the *x*-component velocity at the center of the constriction microchannel, $u(0,y)$, for Newtonian model (solid line) and OB model (symbol).

Afonso et al. [119] derived an analytical solution of viscoelastic EOF between two parallel plates based on the Debey-Hückel approximation, which is valid under the condition of low zeta potential (i.e., $\xi_0 < 25$ mV). The analytical solution of the velocity profile across the height of the channel is given as:

$$u^E = \left(\frac{\kappa\psi_0 E_x}{\eta} - 2\bar{C}\kappa^2\varepsilon\lambda^2 \left[\frac{\kappa\psi_0 E_x}{\eta} \right]^3 \right)\left(\bar{A}-1\right) + \frac{2}{3}\kappa^2\varepsilon\lambda^2 \left[\frac{\kappa\psi_0 E_x}{\eta} \right]^3 \times \left(\bar{A}^3-1\right), \tag{3.2}$$

where κ is the dielectric constant of the solution, $\bar{A} = ((\cosh(\kappa y)) / (\cos(\kappa H)))$, $\kappa^2 = ((2n_0 e^2 z^2) / (\kappa k_B T))$, k_B is the Boltzmann constant, and n_0 is the ionic density. For OB model, $\varepsilon = 0$. The above equation yields $u^E = \left(\frac{\kappa\psi 0 E_x}{\eta} \right)\left(\bar{A}-1\right)$.

To further validate our code for OB model, EOF of viscoelastic fluid with $\eta_s = 0.001$ kg/(m·s), $\eta_p = 0.00222$ kg/(m·s), $\eta_0 = \eta_s + \eta_p = 0.00322$ kg/(m·s), and $\lambda = 8.6$ ms in a straight 2D channel (with height of 40 μm) is studied. These rheology parameters are corresponding to those of 100

ppm PAA solution. U_0 is set as 10 V, while ξ_0 is chosen as −10 mV and −110 mV, respectively. Under the considered conditions, the flows are steady state due to relatively low electric field strength. Figure 3.6 depicts the *x*-component velocity profile at the center of the channel, and the numerical results (triangles) are in excellent agreement with the analytical results (lines). Although the analytical solution is based on the Debey-Hückel approximation, the numerical result also agrees well with the analytical solution when the zeta potential ξ_0 is −110 mV. Therefore, the agreement of results attained from the OB model and the Newtonian model, which are also validated by the Helmholtz-Smoluchowski approximation, as well as the agreement of analytical solution of OB model and numerical results for EOF of viscoelastic fluid in a straight channel, validate the code.

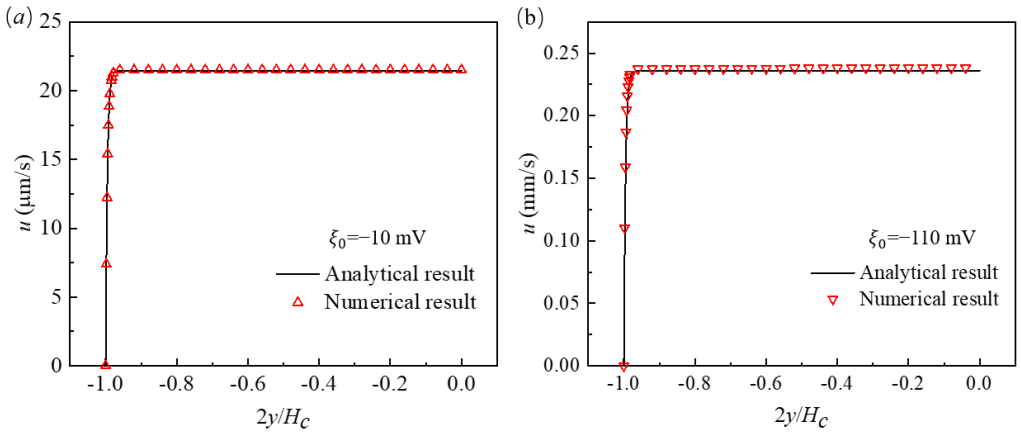

Figure 3.6 The *x*-component velocity profile of viscoelastic electroosmotic flow (EOF) between two parallel plates: (a) zeta potential is −10 mV, (b) zeta potential is −110 mV. Analytical result of Afonso et al. (solid line) and current numerical result (symbol).

3.4 Mesh Independence Study

Three different meshes are used to conduct the mesh independence study with E_{app} = 600 V/cm and c_p = 100 ppm. As shown in Figure 3.7, there are 135192, 95252, and 77192 cells in mesh 1,

mesh 2, and mesh 3, respectively. For mesh 1, the meshes near the charged wall are 7 nm, so there are 14 meshes within the EDL thickness. In mesh 2 and mesh 3, the meshes near the charged wall are 10 nm, and there are 10 meshes within the EDL thickness. However, there are fewer meshes within the two reservoirs in mesh 3 than in mesh 2. Figure 3.8 shows spatial distribution of the normal polymer stress and streamlines of three different meshes at t = 1.78 s. The normal polymer stress and streamlines of the three meshes show no notable difference.

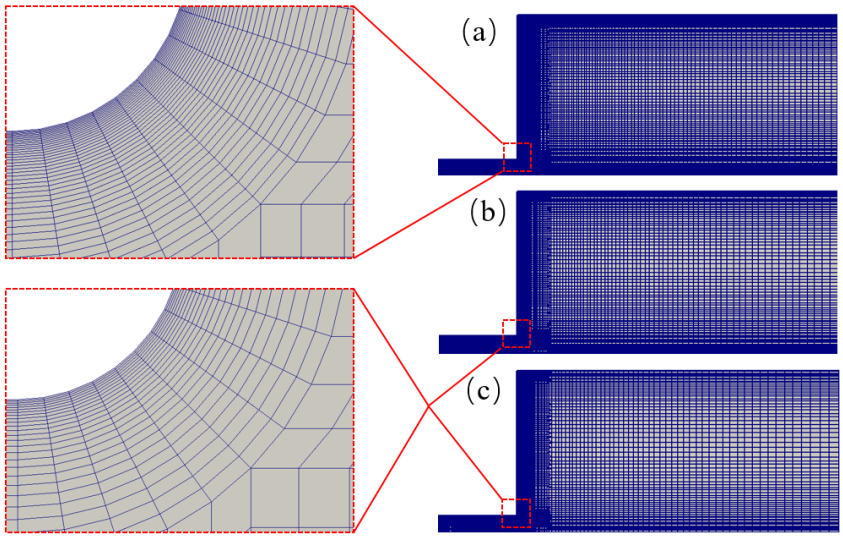

Figure 3.7 Three different meshes used for the mesh independence study. The meshes are symmetric with respect to the *x*-axis and *y*-axis, and only 1/4 of the total meshes are presented. (a) mesh 1: 135192 cells, (b) mesh 2: 95252 cells, (c) mesh 3: 77192 cells.

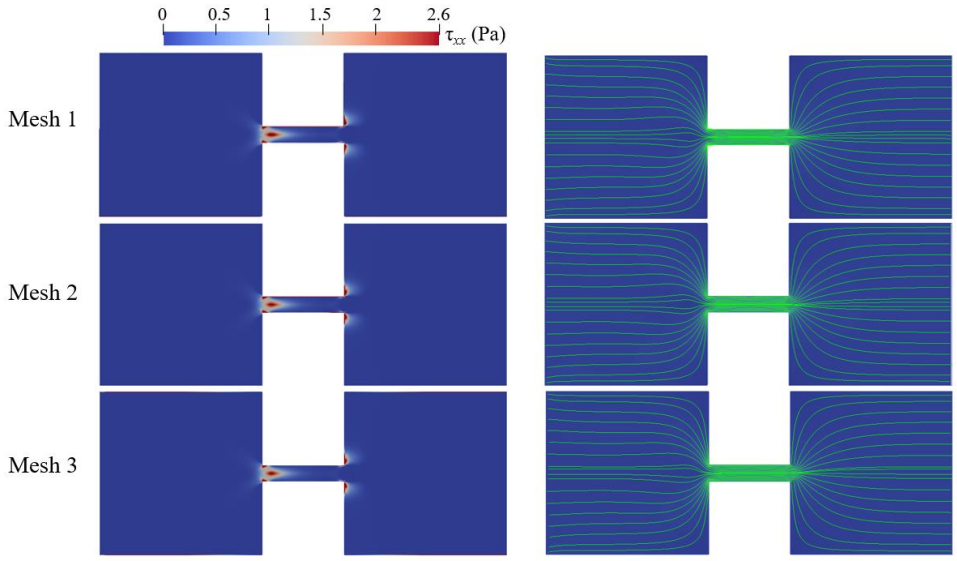

Figure 3.8 Spatial distribution of normal polymeric stress (left) and streamlines (right) for mesh 1 (the top row), mesh 2 (the middle row), and mesh 3 (the bottom row) at t = 1.78 s.

Figure 3.9 shows the spatial distribution of velocity magnitudes along $x = 0$ and $y = 0$ at t = 1.78 s. For velocity magnitude distribution along $x = 0$ (Figure 3.9a), the maximum relative error occurs at $y = 0$. The maximum relative error for mesh 2 is $|U_{\text{meshs2}} - U_{\text{mesh1}}| / U_{\text{mesh1}} = 0.9\%$, and the maximum relative error for mesh 3 is $|U_{\text{meshs3}} - U_{\text{mesh1}}| / U_{\text{mesh1}} = 1.1\%$. The average relative errors for all sampling point are 0.45% for mesh 2 and 0.64% for mesh 3. For velocity magnitude distribution along $y = 0$ (Figure 3.9b), compared to mesh 1, the average relative errors for all sampling points are, respectively, 0.29% for mesh 2 and 0.72% for mesh 3.

Since the results from the above three meshes are in good agreement, mesh 3 is used to perform other simulations.

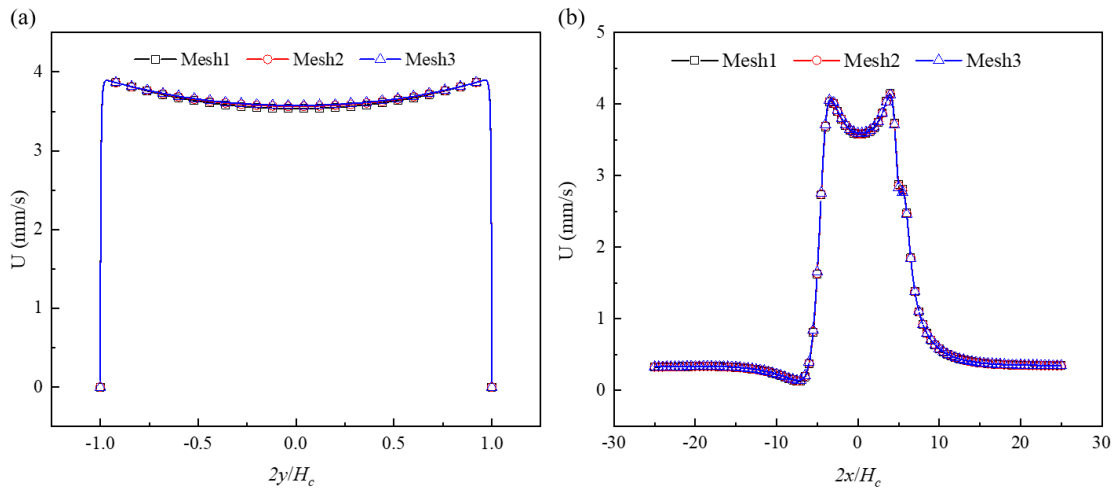

Figure 3.9 Spatial distribution of velocity magnitudes at t = 1.78 s: (a) velocity magnitudes profile at x = 0, (b) velocity magnitudes profile at y = 0.

3.5 Results and Discussion

Newtonian fluid is investigated to provide the reference flow characteristics for the contraction geometry. For the PAA solution with different concentrations c_p, the applied apparent electric field E_{app} varies from low values to high (i.e., 100-600 V/cm). In this section, first, the flow pattern of Newtonian fluid and the time-dependent flow patterns of PAA solutions are described. Then, the instabilities of PAA solutions with various E_{app} and c_p are discussed, and a flow map is formed based on the investigated values of E_{app} and c_p. Finally, statistical results of cross-sectional average velocity are presented.

3.5.1 Instability of PAA Solutions

For Newtonian fluids with various total viscosities, the EOF reaches a steady state under all conditions of the applied electric field strengths. There is no vortex occurring in the reservoirs and the constriction microchannel. The streamlines of Newtonian fluid show excellent symmetry about the x-axis. Additionally, the magnitude of the velocity, $U(x, y)$, is symmetric about the y-axis, $U(x, y) = U(x, -y)$. For EOF of PAA solutions, when E_{app} and c_p are relatively low, the flow pattern

is similar to that of Newtonian fluid, and the flow reaches a steady state without vortex. With increasing E_{app} and c_p, however, the viscoelastic flow becomes time dependent and significant instabilities are observed. Figure 3.10 depicts the streamlines at different times when E_{app} = 100 V/cm and c_p = 500 ppm. Figure 3.11 depicts the streamlines at different times when E_{app} = 600 V/cm and c_p = 150 ppm. Figure 3.12 shows the velocity magnitudes as a function of time at three different locations, namely, upstream the constriction microchannel ($-3H_C$, 0), cent of the constriction microchannel (0, 0), and downstream the constriction microchannel ($3H_C$, 0). For the EOF of both c_p = 150 ppm and c_p = 500 ppm, strong instabilities and upstream vortices are observed.

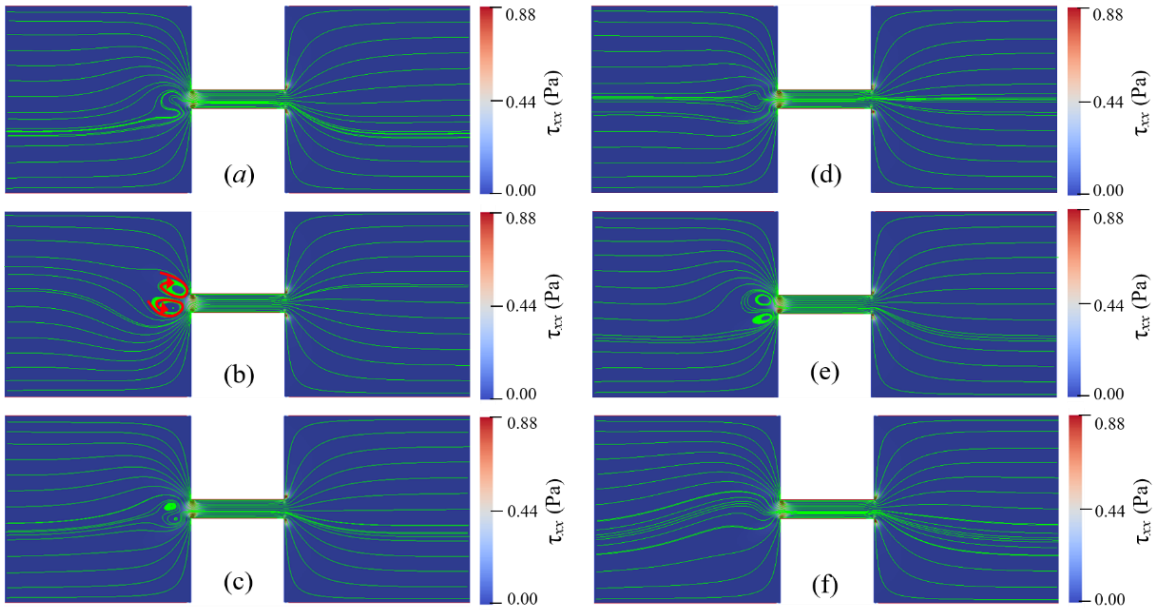

Figure 3.10 Instability of EOF with c_p = 500 ppm and E_{app} = 100 V/cm. Streamlines at different times: (a) 1.71 s, (b) 1.75 s, (c) 1.79 s, (d) 1.83 s, and (f) 1.91 s. The color bar represents the elastic normal stress τ_{xx}.

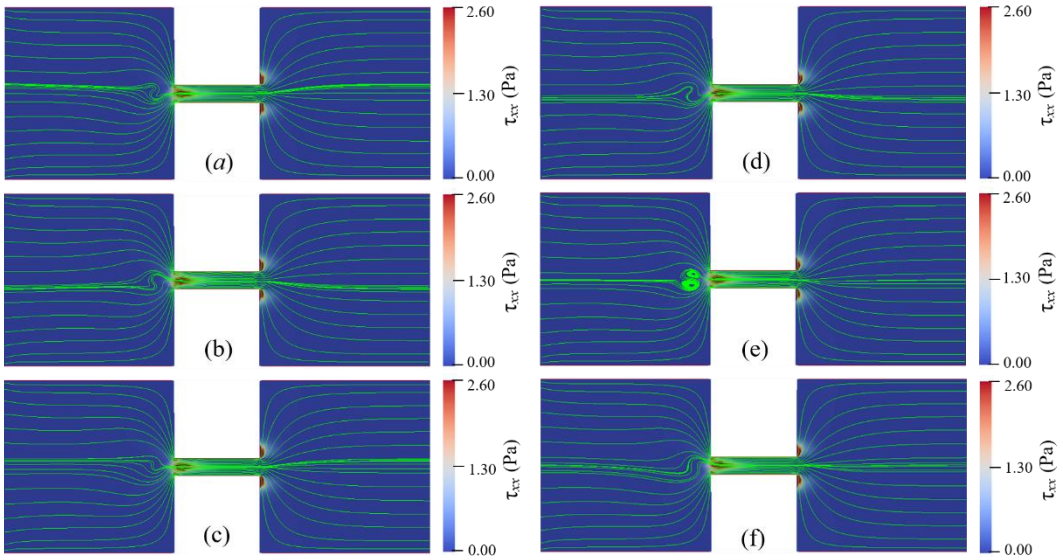

Figure 3.11 Instability of EOF with c_p = 150 ppm and E_{app} = 600 V/cm. Streamlines at different times: (a) 1.70 s, (b) 1.72 s, (c) 1.74 s, (d) 1.76 s, (e) 1.78 s, and (f) 1.80 s. The color bar represents the elastic normal stress τ_{xx}.

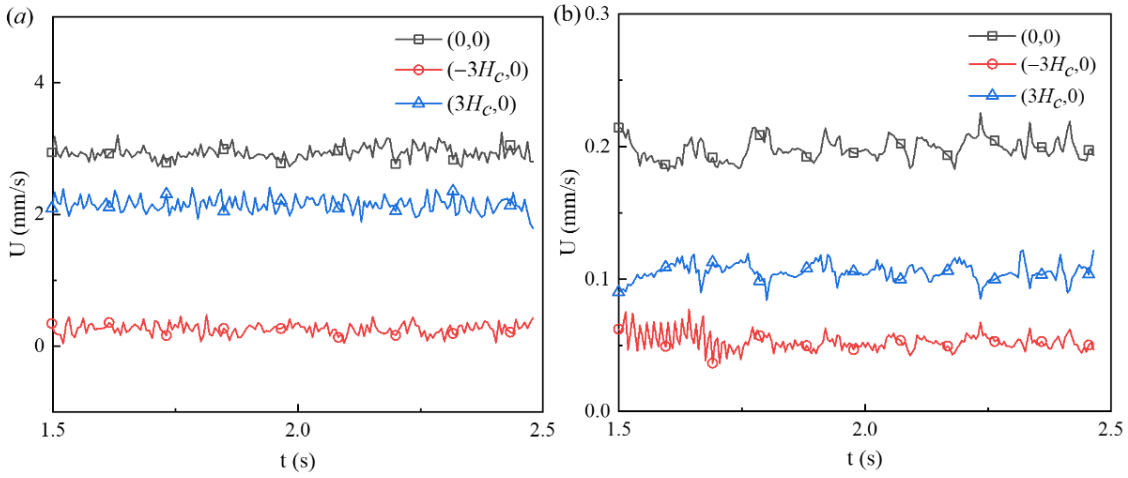

Figure 3.12 Velocity magnitudes at three different locations ((−3H_C, 0), (0, 0), (3H_C, 0)): (a) c_p = 150 ppm and E_{app} = 600 V/cm, (b) c_p = 500 ppm and E_{app} = 100 V/cm.

Figure 3.10 and Figure 3.11 show that the viscoelastic EOF is time dependent. The streamlines in the left inlet reservoir far away from the solid walls (AB and GH in Figure 3.1) and near the

entrance of the constriction microchannel show significant fluctuation and become asymmetric about the *x*-axis. However, the streamlines near the solid walls of both reservoirs and in the outlet reservoir show insignificant change over time. Within 0.1 s, vortices continuously form and disappear within the inlet reservoir right before the entrance of the constriction microchannel. In Figure 3.10a, significant curvature at the streamlines of the EOF upstream the constriction microchannel is observed. Then, the curvature of the streamlines further develops into a pair of vortices showing notable differences at different times. After growing to the maximum size, the vortices start to shrink until the vortices break and disappear, as shown in Figure 3.10c, d. Next, the vortices in the EOF keep forming and breaking repeatedly as shown in Figure 3.10e, f. Comparing Figure 3.10b, c, the central locations of the vortices are both spatially and temporally dependent. In Figure 3.10b, the direction of the circulation is marked by curved red lines. The pair of vortices are in opposite directions and form a stagnant region right before the entrance of the constriction microchannel. Therefore, the induced vortices are referred to as entrance-centerline vortices.

For c_p = 150 ppm and E_{app} = 600 V/cm the width and length of the vortices are nearly the same as the height of the constriction microchannel (H_C), while for c_p = 500 ppm and E_{app} = 100 V/cm, the width and the length of the vortices are about $2H_C$. In a similar geometry, however, Ko [171] did not observe vortices in their experiments with 200 ppm PAA solution under E_{app} ranging from 75 V/cm to 200 V/cm. The elastic instability increases with increasing polymer concentration and the applied electric field. The results discussed in the following section show that for c_p = 200 ppm, the vortices occur when the applied electric field exceeds the threshold value of 300 V/cm. Therefore, the numerical results qualitatively agree with the experimental observation of Ko [171] under their experimental condition. Table C1 in Appendix C summarizes the EOF instabilities

from the literature. In Sadek's [172] experimental study, small vortices at the entrance and large upstream circulation flows were observed. For highly concentrated polymer solution, downstream circulation flows were observed at a critical voltage. The upstream vortices found in this study are distinct from the small vortices and large circulation flows found in Sadek's study [172] in terms of location. Note that the geometry in this study differs significantly from the experimental study of Sadek [172], and large circulating flows near the reservoir corners and channel lips are not observed.

For Newtonian fluid, the EOF reaches a steady state, and the velocity magnitudes are symmetric about the *y*-axis. Therefore, for Newtonian fluid, $U(-3H_C, 0) = U(3H_C, 0)$. However, as shown in Figure 3.12, the velocity magnitudes at three points $(-3H_C, 0)$, (0, 0) and $(3H_C, 0)$ fluctuate around specific values and velocity magnitudes do not show symmetry about the *y*-axis. For c_p = 500 ppm and E_{app} = 100 V/cm, as shown in Figure 3.12b, the time-averaged velocity at the channel center is 0.201 mm/s with a standard deviation of 0.013 mm/s. The time-averaged velocity downstream the constriction microchannel is 0.108 mm/s, which is about two times that upstream the constriction microchannel (i.e., 0.047 mm/s). For c_p = 150 ppm and E_{app} = 600 V/cm, the time-averaged velocities at the upstream, center, and downstream of the constriction microchannel are, respectively, 0.19 mm/s, 2.82 mm/s, and 2.05 mm/s. The ratio of the downstream velocity to the upstream velocity is about ten times. In contrast to Newtonian EOF, the flow velocity of the viscoelastic fluid at the downstream is significantly higher than that at the upstream, which has also been experimentally observed in Ko's [171] experiments, where a fluid jet after the constriction microchannel was observed and the ratio of the velocity at the downstream centerline to that at upstream of the constriction microchannel varies between 1 and 2 under E_{app} ranging from 75 V/cm to 200 V/cm and c_p = 200 ppm.

Figure 3.12 also shows that EOF of c_p = 500 ppm and E_{app} = 100 V/cm presents stronger instabilities than that of c_p = 500 ppm and E_{app} = 600 V/cm. Comparing Figure 3.10 and Figure 3.11, the streamlines show stronger fluctuation and larger upstream vortices for solution with relatively high polymer concentrations. Such a trend suggests that although the increase of both E_{app} and c_p can enhance the instabilities of the viscoelastic EOF, the polymer concentration, c_p, affects the instabilities of the EOF more significantly, which will be further discussed in the next section.

Figure 3.10 and Figure 3.11 also show the spatial distribution of elastic normal stress τ_{xx} with the color bar representing its magnitude. To clearly reveal it, Figure 3.13 depicts the spatial distribution of τ_{xx} in the whole geometry for c_p = 150 ppm and E_{app} = 600 V/cm at t = 1.78 s. Within the two reservoirs, the elastic normal stress is nearly zero at location far away from the constriction microchannel. However, significant elastic normal stress is induced near the entrance of the constriction microchannel and near the downstream lips. Due to the contraction geometry, the electric field within the constriction microchannel is about 10 times that within the inlet reservoir as shown in Figure 3.5a, and the flow velocity in the microchannel is significantly higher than that in the reservoir. For example, Figure 3.12 shows that the ratio of the time-averaged velocity within the microchannel to that in the inlet reservoir, $U(0, 0) = U(-3H_C, 0)$, is 4.28 for c_p = 500 ppm and E_{app} = 100 V/cm and 10.79 for c_p = 150 ppm and E_{app} = 600 V/cm. Near the entrance of the microchannel, the high velocity gradient results in a strong extension of polymer molecules and consequently induces significant elastic normal stress. Therefore, τ_{xx} experiences a rapid increase near the entrance of the constriction microchannel. At the exit of the constriction microchannel, similarly, a significant increase of τ_{xx} is induced at the exit lips. Figure 3.14a and b depict the streamlines in the constriction microchannel and the color bar represents the velocity

magnitude, U, for c_p = 150 ppm and E_{app} = 600 V/cm and Newtonian fluid with the same total viscosity and E_{app} at t = 1.78 s, respectively. For the viscoelastic fluid, at both the entrance and exit of the constriction microchannel, as shown by the dashed circles in Figure 3.14a, velocity becomes spatially dependent along the y-axis. Velocity near the walls of the constriction microchannel is significantly higher than that at the centerline of the microchannel, and a local maximum occurs near the inlet/outlet corners of the constriction microchannel. However, in the EOF of Newtonian fluid, as shown in Figure 3.14b, at both the entrance and the exit of the constriction microchannel, the velocity magnitude is more evenly distributed in the cross-section of the constriction microchannel. Figure 3.14c depicts the velocity magnitude profile at the entrance ($2x/H_C = -5$) and exit ($2x/H_C = 5$) of the constriction microchannel. For Newtonian fluid, the velocity magnitude profile is identical at $2x/H_C = \pm 5$ and is symmetric about the x-axis. The ratio of the maximum velocity magnitude near the channel walls to that at the centerline is 1.6. However, for PAA solution, due to the elastic instability, the velocity magnitude profile is asymmetric about the x-axis at $2x/H_C = \pm 5$. In addition, the ratios of the maximum velocity magnitude near the channel walls to that at the centerline are 9.7 and 4 at $2x/H_C = -5$ and $2x/H_C = 5$, respectively, which are much higher than that of the Newtonian fluid. For Newtonian fluid, the velocity profile is symmetric about the centerline of the microchannel (i.e., $y = 0$). However, Figure 3.14c shows that the local maximum velocity near the top channel wall differs from the velocity near the bottom channel wall, and the velocity profile is asymmetric about $y = 0$.

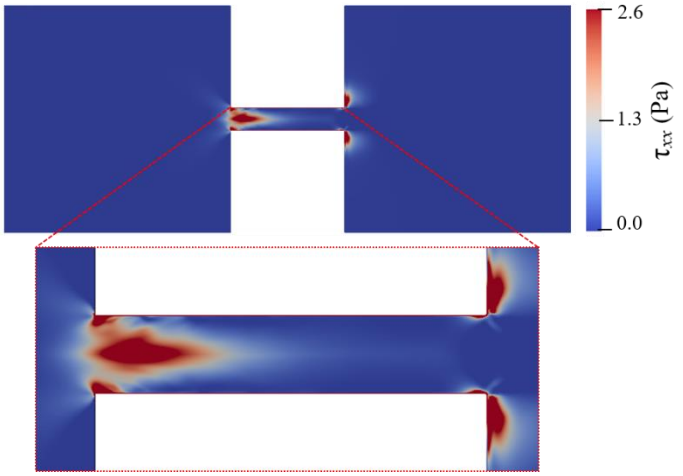

Figure 3.13 Spatial distribution of the elastic normal stress τ_{xx} for c_p = 150 ppm and E_{app} = 600 V/cm at t = 1.78 s.

As PAA solution flows from the microchannel into the outlet reservoir, fluid velocity first decreases when fluid exits the microchannel and then increases in the outlet reservoir, as shown by the region marked with a circle in Figure 3.14a and by the velocity magnitude as a function of x at y = 0 in Figure 3.14d. The two dashed lines in Figure 3.14d represent the entrance and exit of the constriction microchannel. EOF of Newtonian fluid within the constriction is a plateau, and its velocity magnitude within the constriction is much higher than those at both reservoirs, and this is because the electric field within the constriction microchannel is significantly higher than that in the reservoirs. However, the velocity of PAA solution becomes spatially dependent within the constriction, and a local maximum occurs before the exit and a local minimum occurs at the exit of the constriction microchannel. In addition, a local maximum occurs at the downstream outlet reservoir. Figure 3.14d also clearly shows that the velocity in the downstream outlet reservoir is significantly higher than that at the upstream inlet reservoir. For example, $U(2x/H_C = 10.0)/U(2x/H_C = -10.0)$ = 3.37. The unexpected velocity decrease at the microchannel exit and velocity increase at the downstream outlet reservoir do not occur in Newtonian fluid as shown in Figure

3.14b, d. Such a phenomenon is probably because of the extrudate swell effect of polymers [184]. At the exit of the constriction microchannel, curved streamlines tilting toward the walls of the constriction microchannel are observed in viscoelastic fluid, suggesting that fluid tends to flow toward the charged walls of the microchannel. Such lateral velocity component results in the velocity's increase near the microchannel walls and velocity's decrease near the centerline at the exit of the constriction microchannel. In addition, the significant increase of τ_{xx} near the downstream lips observed in Figure 3.13 can also be attributed to the extrudate swell effect of polymers when polymer exits from the constriction microchannel to larger outlet reservoir.

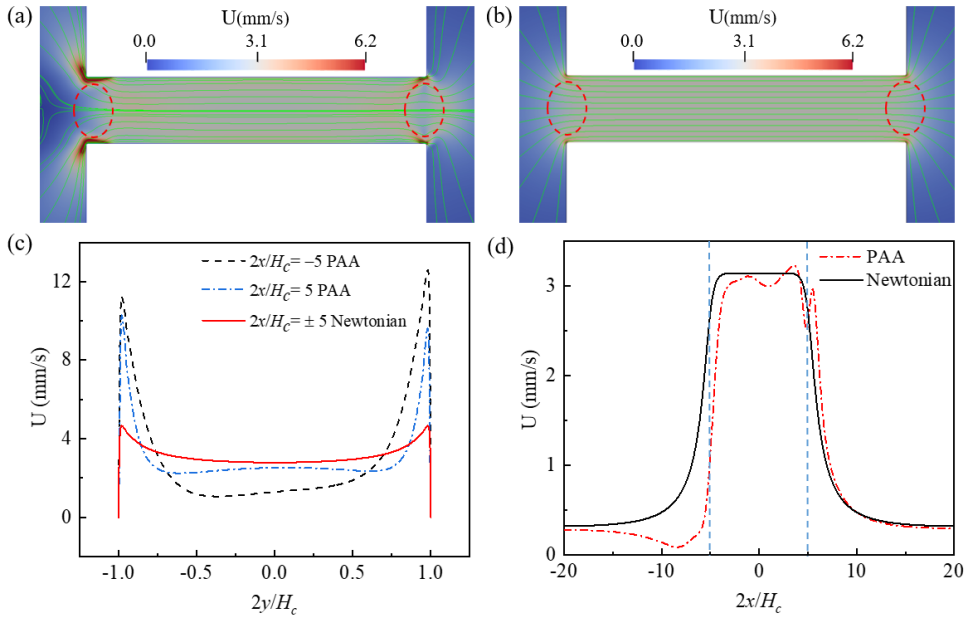

Figure 3.14 Streamlines and velocity magnitude for c_p = 150 ppm and E_{app} = 600 V/cm and Newtonian fluid at t = 1.78 s: (a) 150 ppm PAA solution, (b) Newtonian fluid with same total viscosity at 150 ppm PAA solution, (c) velocity magnitude profiles at $2x/H_C = \pm 5$, (d) velocity magnitudes profiles at y = 0 (The blue dash lines show the position of the contraction microchannel). The color bar represents the velocity magnitude U.

The generated elastic normal stress τ_{xx} was typically used to explain the formation of vortices in pressure-driven viscoelastic flows within curved geometries [27, 185, 186]. It has been reported that the development of the polymeric elastic stresses is caused by the flow-induced changes of the polymer conformation in the solution. Such changes of the polymer conformation are strain-dependent, anisotropic, and dependent on the flow. The extra elastic stresses are nonlinear under shear and can alter the flow behavior. At low Reynolds numbers where inertia is negligible, when the elastic normal stress exceeds by a certain amount the local shear stress, the flow transits from stable to unstable, and the vortices form at upstream of the constriction microchannel. Such elastic instabilities are often observed in flows with sufficient curvature [187-189], and some argue that curvature is necessary for infinitesimal perturbations to be amplified by the normal stress imbalances in the viscoelastic flows [34]. However, other theoretical studies reported that viscoelastic flows also showed a nonlinear instability in parallel shear flows, such as in viscoelastic flows within straight pipes at low Reynolds numbers [190]. Although the formation of the upstream vortices in the viscoelastic EOF shares the same mechanism as the pressure-driven flow, the locations of the vortices found in this study are distinct from the typical lip and corner vortices accruing in pressure-driven viscoelastic flows. This is probably because of the different velocity profiles in the pressure-driven flow and the EOF. In pressure-driven flow, the velocity is zero at solid walls and increases to a maximum at the centerline of the geometry. However, the EOF velocity profile is nearly a plug flow as shown in Figure 3.5b. The velocity increases from zero to a plateau within the EDL thickness, which is only on the order of a few nanometers. For the pressure-driven flow, the highest velocity is at the centerline of the geometry and the velocity near the wall is relatively low, resulting in the stagnant region near the solid boundaries (lips and corners). However, EOF velocity in the vicinity of the charged wall is almost the same as that in

the channel centerline. For the extensional flow of viscoelastic fluids, the stretched polymer molecules lead to large elastic stresses, which significantly depend on the geometry and velocity profile. The induced elastic stresses render the primary flow unstable and cause an irregular secondary flow. The flow subsequently acts back on the polymer molecules and stretches them further, causing a strong disturbance of the EOF and yielding a time-dependent EOF.

3.5.2 Elastic Instabilities under Various E_{app} and c_p

In order to study the effects of E_{app} and c_p on the instabilities of viscoelastic EOF, c_p is varied from 100 ppm to 500 ppm and E_{app} is varied from 100 V/cm to 600 V/cm. Flow patterns under different conditions of E_{app} and c_p are shown in Figure 3.15-Figure 3.18. At certain E_{app} (c_p), EOF becomes more unstable with the increase of c_p (E_{app}). Figure 3.15 shows the streamlines for different PAA concentrations under E_{app} = 600 V/cm, and Figure 3.16 shows the streamlines within the constriction microchannel with the color bar representing pressure for Newtonian fluid and τ_{xx} for PAA solutions. As shown in Figure 3.15 and Figure 3.16, when c_p increases, the polymeric stress τ_{xx} at the entrance of the constriction microchannel increases rapidly, resulting in the fluctuation of the streamlines upstream of the microchannel. When c_p is relatively low (100 ppm), EOF of viscoelastic fluid is similar to that of Newtonian fluid, and the flow is in a steady state. With an increase in the PAA concentration up to 150 ppm, significant curvature of the centerline streamlines is observed, and the streamlines become asymmetric about the x-axis and y-axis. As c_p continuously increases up to 200 ppm, a pair of upstream vortices in opposite flow directions are induced at upstream of the constriction microchannel, forming a stagnant region as shown in Figure 3.15d. The width and length of the pair of vortices are about 1.6 times the constriction microchannel height (i.e., $1.6H_C$). Such vortices are found to grow significantly in size with increasing c_p, which is in qualitative agreement with the experimental observations of Ko [171].

Within the constriction microchannel, as shown in Figure 3.16d, nearly 1/4 of the microchannel length (i.e., 1/4L_C) from the entrance shows a significant increase of τ_{xx}. Near the downstream lips of the microchannel, a local maximum of the polymeric stress τ_{xx} is observed. When c_p increases to 250 ppm, the fluctuation of the streamlines and the size of the vortices grow dramatically as shown in Figure 3.15e, in which the width and length of the vortices are about 2.9 times the microchannel height (i.e., 2.9H_C). The region with significant value of τ_{xx} is near 1/3 of the microchannel length (i.e., 1/3L_C), as shown in Figure 3.16e. When c_p further increases to 500 ppm, as shown in Figure 3.15f, the vortices grow to 4.4 times of the constriction microchannel height (i.e., 4.4H_C). More than half of the microchannel length shows a significant increase in τ_{xx}. Furthermore, a small vortex is induced near the downstream lip of the microchannel, which is also reported in experimental studies of Ko [171].

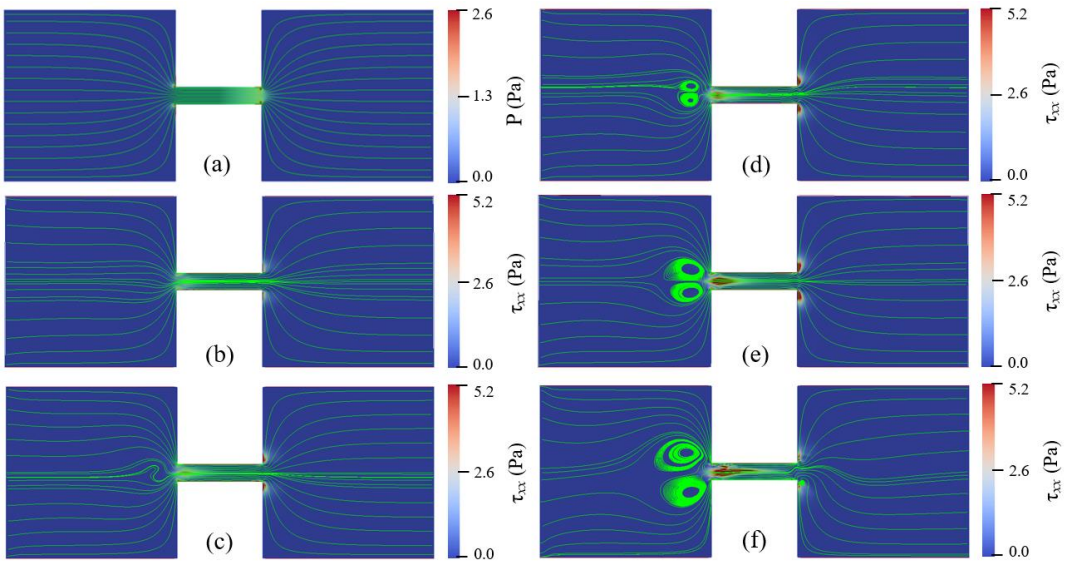

Figure 3.15 Streamlines of Newtonian fluid and PAA solutions with different concentrations under E_{app} = 600 V/cm at 1.70 s: (a) Newtonian fluid, (b) c_p = 100 ppm, (c) c_p = 150 ppm, (d) c_p = 200 ppm, (e) c_p = 250 ppm, and (f) c_p = 500 ppm. The color bar represents the elastic normal stress τ_{xx}.

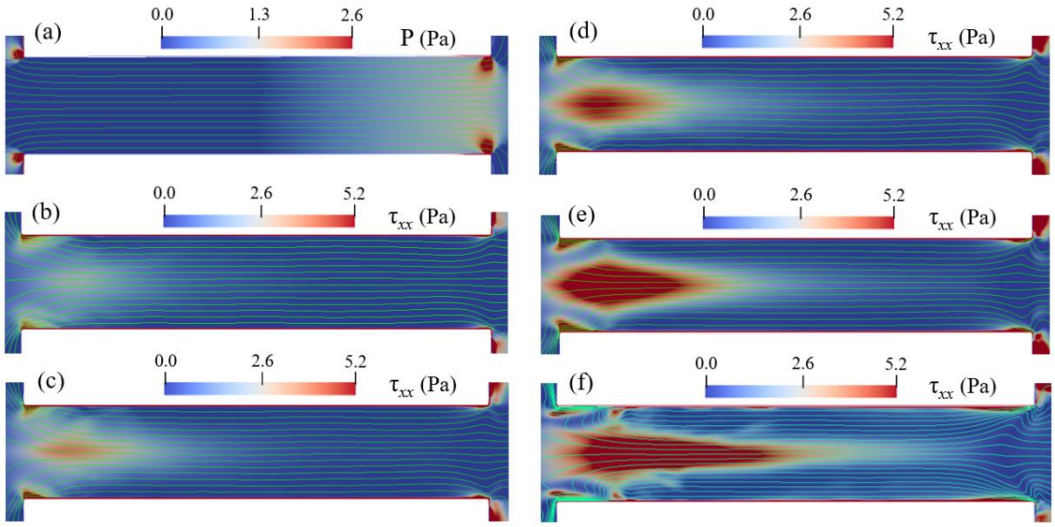

Figure 3.16 Streamlines in microchannel of Newtonian fluid and PAA solutions with different concentrations under E_{app} = 600 V/cm at 1.70 s: (a) Newtonian fluid, (b) c_p = 100 ppm, (c) c_p = 150 ppm, (d) c_p = 200 ppm, (e) c_p = 250 ppm, and (f) c_p = 500 ppm. The color bar represents the elastic normal stress τ_{xx}.

Figure 3.17 and Figure 3.18 show the streamlines for c_p = 150 ppm when E_{app} is varied from 100 V/cm to 600 V/cm with the color bar representing the magnitude of τ_{xx}. At a relatively low electric field such as E_{app} = 100 V/cm, EOF of PAA solution is similar to the Newtonian fluid, and the flow is in a steady state and symmetric about channel centerline. In addition, the induced polymeric stress τ_{xx} in the constriction microchannel is relatively small. When E_{app} increases up to 400 V/cm, centerline streamlines start to show notable fluctuation and become asymmetric about the x-axis. At the entrance of the microchannel, microchannel, a slight increase of τ_{xx} is observed, however, significant increase of τ_{xx} is observed near the microchannel walls and the downstream lips, as shown in Figure 3.18d. When E_{app} increases to 500 V/cm, a pair of upstream vortices are induced upstream microchannel, and the size of the vortices is about the height of the constriction microchannel. Additionally, as shown in Figure 3.18e, significant τ_{xx} is induced near the entrance

of the constriction microchannel. However, when E_{app} further increases to 600 V/cm, the size of the upstream vortices does not show a notable increase in comparison with that of E_{app} = 500 V/cm. The results clearly show that the increase of c_p and/or E_{app} can magnify the elastic instabilities of the viscoelastic EOF. However, the increase of c_p has a more significant enhancing effect on the elastic instabilities of the viscoelastic EOF than the increase of E_{app}.

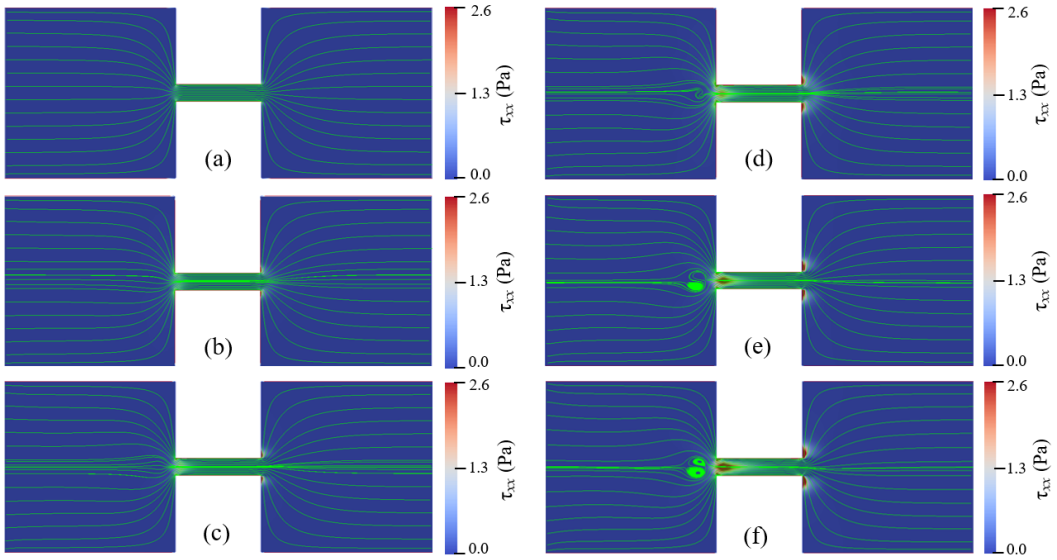

Figure 3.17 Streamlines of 150 ppm PAA solution under different E_{app} at 1.78 s: (a) 100 V/cm, (b) 200 V/cm, (c) 300 V/cm, (d) 400 V/cm, (e) 500 V/cm, and (f) 600 V/cm. The color bar represents the elastic normal stress τ_{xx}.

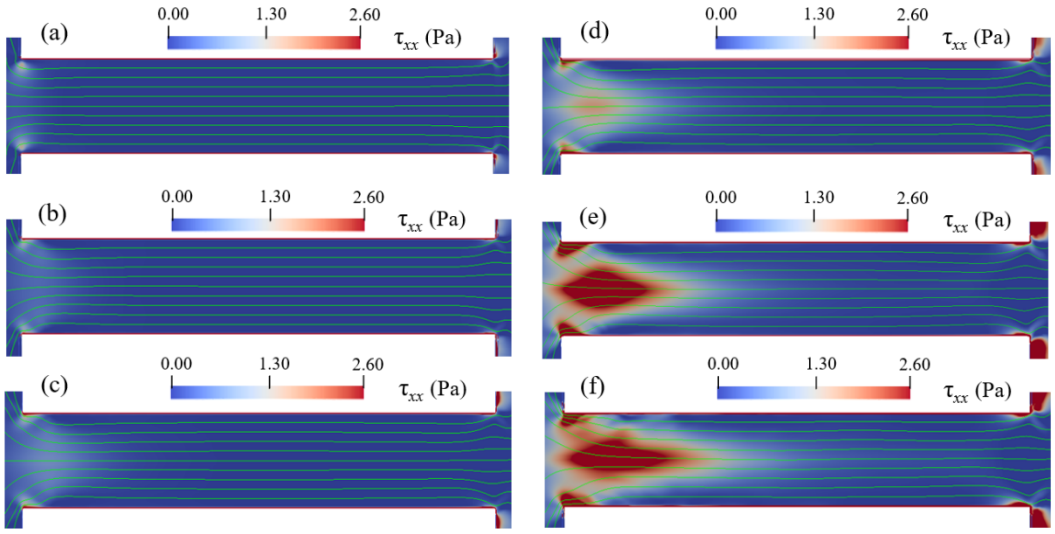

Figure 3.18 Streamlines in microchannel of 150 ppm PAA solution under different E_{app} at 1.78 s: (a) 100 V/cm, (b) 200 V/cm, (c) 300 V/cm, (d) 400 V/cm, (e) 500 V/cm, and (f) 600 V/cm. The color bar represents the elastic normal stress τ_{xx}.

Figure 3.19 depicts a flow map for the onset of vortices in unstable EOF as functions of c_p and E_{app}. At a fixed c_p (E_{app}), vortices and unstable EOF occur when E_{app} (c_p) exceeds a specific threshold value. For example, for c_p = 200 ppm, the flow becomes unstable with the occurrence of vortices when E_{app} is above 300 V/cm. For a relatively low PAA concentration (i.e., c_p = 100 ppm), it requires a very high electric field (up to 850 V/cm) to yield unstable EOF with upstream vortices. In contrast, for a relatively high c_p (i.e., c_p = 500 ppm), the vortices occur at E_{app} between 50 V/cm and 100 V/cm. An asymptotic curve fitting is implemented to illustrate the transition condition from no upstream vortices to the formation of upstream vortices, which is given as $E_{app} = 47.79 + 2892.25 \times 0.987^{cp}$, where c_p represents the polymer concentration in ppm, and E_{app} is the apparent electric field in V/cm. Above the curve in Figure 3.19, the EOF becomes time-dependent with upstream vortices, and no vortex forms under the conditions below the curve. Note that the flow map is only valid for the geometry considered in this study with the zeta potential of −100

mV. The instabilities of the viscoelastic EOF are dependent on the value of zeta potential. A comparison of the flow patterns of lower zeta potential (−70 mV) and higher zeta potential (−150 mV) is presented in section 3.5.4.

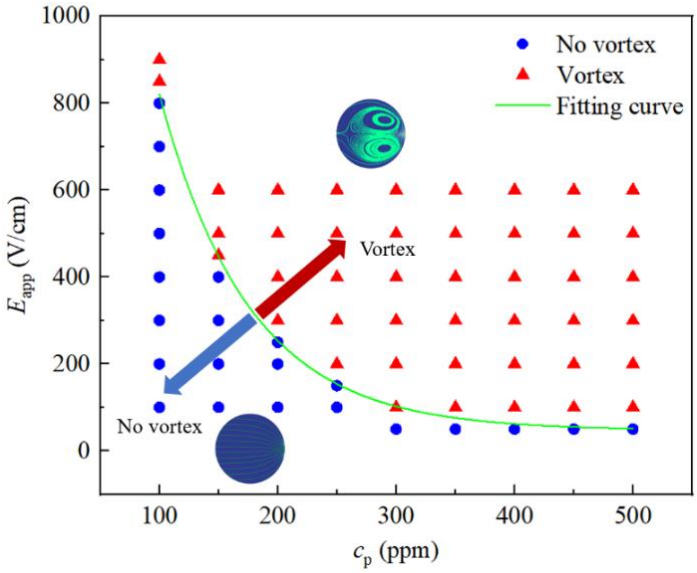

Figure 3.19 Flow map in c_p-E_{app} space for EOF of PAA solutions through a 10:1:10 constriction/expansion microchannel. Up-right of the fitting curve are the conditions that trigger the vortex in the EOF.

Since the flow velocity is time dependent, we first calculate the cross-sectional average velocity over a period of $\Delta t = t_2 - t_1$, and then take the time-average to obtain the averaged velocity as,

$$\bar{U} = \frac{\int_{t_1}^{t_2} \int_{-H_C/2}^{H_C/2} U(0, y)\, dy dt}{\Delta t \cdot H_C}. \tag{3.3}$$

Δt = 1 s is used in this study. Figure 3.20 shows the average velocity at the center of the constriction as a function of c_p at different values of E_{app}. In comparison, it also shows the result of Newtonian fluid whose viscosity is the same as the total viscosity of PAA solution under E_{app} = 600 V/cm. Under the same E_{app} = 600 V/cm, the average velocity in the constriction microchannel

of the Newtonian flow is about 6 -12% higher than that of the PAA solution. The decrease of the average velocity in PAA solution is attributed to the induced polymeric stress at the entrance of the constriction microchannel. For Newtonian fluid, the average velocity decreases as c_p increases, which is due to the increase of viscosity to make its viscosity be the same as that of PAA solution with the concentration of c_p. For PAA solutions, under the same E_{app}, average velocity exponentially decreases as the polymer concentration increases. One reason is attributed to the increase of total viscosity with the increase in c_p. In addition, the induced polymer stress within the constriction increases with the increase of polymer concentration, as show in Figure 3.16, and the induced polymer stress slows down the flow.

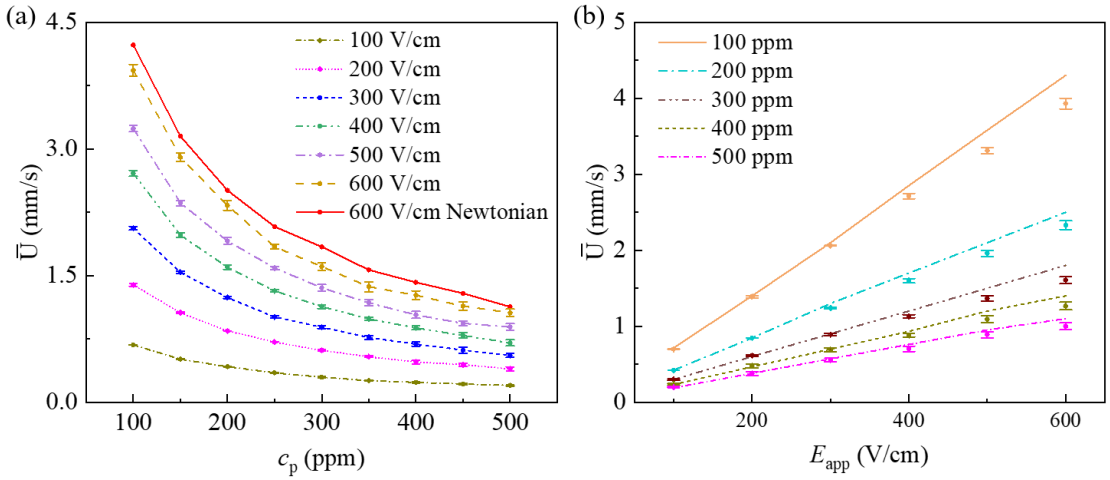

Figure 3.20 Time averaged cross-sectional average velocity at the center of the constriction microchannel (x = 0): (a) average velocity, (b) comparison of average velocity (with deviation) and Helmholtz-Smoluchowski velocity (lines).

Under the considered condition of c_0 = 0.01 mM, the EDL thickness is only 95 nm, which is much smaller than the height of the constriction. In Newtonian fluid, the EOF velocity can be approximated by the well-known Helmholtz-Smoluchowski velocity formula as described in

Equation (3.1). We wonder if the average velocity of PAA solutions can still be approximated with the Helmholtz-Smoluchowski velocity formula. Since the actual local electric field within the constriction is much higher than the apparent electric field E_{app}, time-averaged electric field in the x-direction at the center of the constriction is used in the calculation of the Helmholtz-Smoluchowski velocity. Figure 3.20b shows the average velocity as a function of the apparent electric field under various PAA concentrations. The lines in Figure 3.20b represent the corresponding EOF velocity predicted by the Helmholtz-Smoluchowski velocity formula. At a fixed c_p, as expected, the EOF velocity increases with an increase in the applied electric field. In general, the Helmholtz-Smoluchowski formula over predicts the velocity, and at a fixed c_p, the relative error increases with the increasing E_{app}. For example, for c_p = 100 ppm, the relative errors under E_{app} = 100 V/cm and 600 V/cm are, respectively, 1.2% and 8.6%. At a fixed E_{app}, the absolute error, which is the difference between the Helmholtz-Smoluchowski approximated velocity and the average velocity obtained from the full numerical simulation, increases with the increasing PAA concentration. However, the relative error shows no notable change with the increasing c_p. For example, at E_{app} = 600 V/cm, the relative errors for c_p = 100 ppm, 300 ppm, and 500 ppm are, respectively, 8.7%, 9.6%, and 9.0%. To evaluate the applicability of the Helmholtz-Smoluchowski formula to approximate the velocity of viscoelastic fluids for cp ranging from 100 ppm to 500 ppm, the minimum, average, and maximum relative errors at different E_{app} are calculated as shown in Table 1. When $E_{app} \leq 300$ V/cm, the relative error is less than 5%. However, when $E_{app} \geq 400$ V/cm, the relative error is larger than 5%, and the Helmholtz-Smoluchowski formula failed to predict the velocity of the viscoelastic fluids accurately. In this study, the largest relative error is 9.6% when c_p = 300 ppm and E_{app} = 600 V/cm.

Table 3.1 Relative error between the Helmholtz-Smoluchowski velocity and the average velocity from the full mathematic method.

E_{app} (V/cm)	100	200	300	400	500	600
Minimum relative error	1.0%	1.3%	1.8%	5.5%	7.0%	8.5%
Average relative error	1.3%	1.6%	2.3%	5.9%	7.7%	8.9%
Maximum relative error	1.5%	1.9%	2.8%	6.5%	8.2%	9.6%

3.5.3 Dimensionless numbers

Dimensional analysis is a useful tool to fully characterize the flow and identify the dominant forces in complex flow of polymeric materials. Reynolds number (*Re*) is commonly used in rheological studies to determine whether the inertial force or the viscous force is dominating the flow, which is given by: $Re = \rho u l / \eta$, where ρ is the fluid density, u is the average velocity in the microchannel, l is the characteristic length scale (H_C), and η is the fluid viscosity. In addition, the Weissenberg number (*Wi*) is used to assess the flow elasticity of the PAA solutions, which is defined as: $Wi = \lambda u / l$, where λ is the relaxation time. Based on our results, the *Re* is nearly zero, indicating that the inertial force of the EOF is negligible. The *Wi* is on the order of 1, which indicates that the elastic effect in the flow is significant.

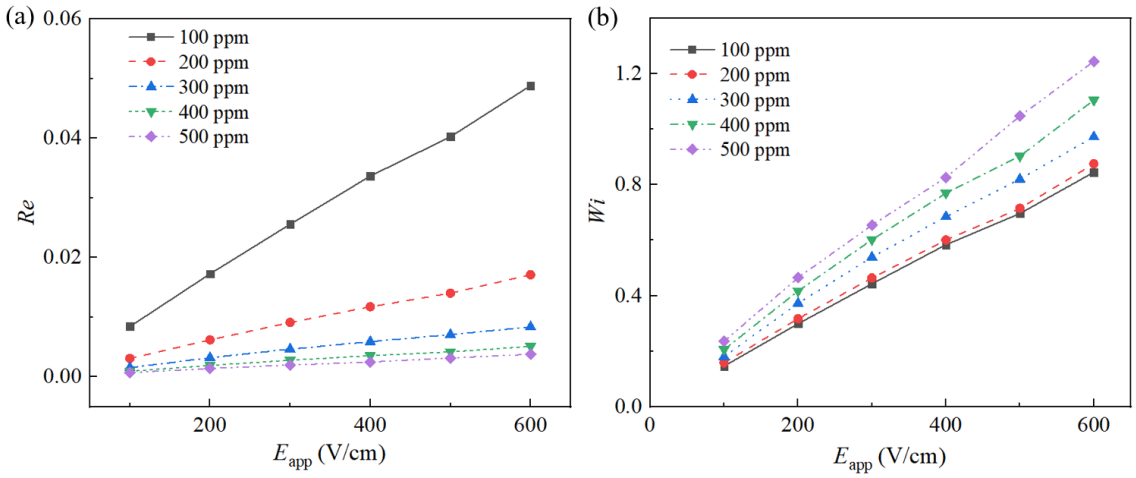

Figure 3.21 Reynolds number (a) and Weissenberg number (b) of the viscoelastic EOF.

3.5.4 Results for other Zeta potentials

Two other different zeta potentials (−70 mV and −150 mV) are studied for 150 ppm PAA solution under E_{app} = 600 V/cm. Figure 3.22 shows the results of −70 mV zeta potential. Significant curvatures of the centerline streamlines are observed. However, at other places, no significant disturbance is observed. Figure 3.23 shows the results of −150 mV zeta potential. Similar to the results of −110 mV zeta potential, strong disturbance is induced in the viscoelastic EOF. Upstream vortices form and disappear. An increase of elastic normal stress is observed within the constriction microchannel. Figure 3.24 shows the velocity magnitude at the center of constriction channel (i.e., (0,0)). When the zeta potential is low (−70 mV), the velocity magnitude is almost steady state. However, when the zeta potential is high (−150 mV), the velocity magnitude shows strong fluctuation. The results for zeta potentials of −70 mV, −110 mV, and −150 mV show that the elastic instabilities of the EOF of PAA solutions are dependent on the value of zeta potential. Higher zeta potential induces larger electroosmotic velocity, and therefore stronger stretching of the polymers at the entrance of the constriction microchannel. Higher velocity and polymer normal stress lead to stronger instabilities of the viscoelastic flow.

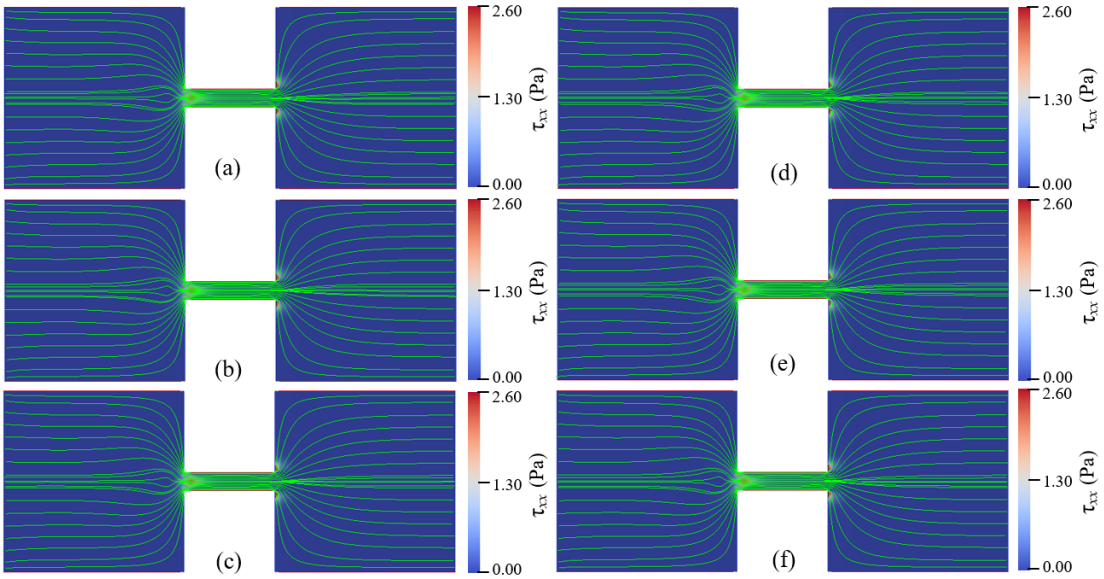

Figure 3.22 Streamlines of 150 ppm PAA solution under at E_{app} = 600 V/cm at different times: (a) 1.70 s, (b) 1.72 s, (c) 1.74 s, (d) 1.76 s, (e) 1.78 s, (f) 1.80 s. Zeta potential is −70 mV. The color bar represents the elastic normal stress τ_{xx}.

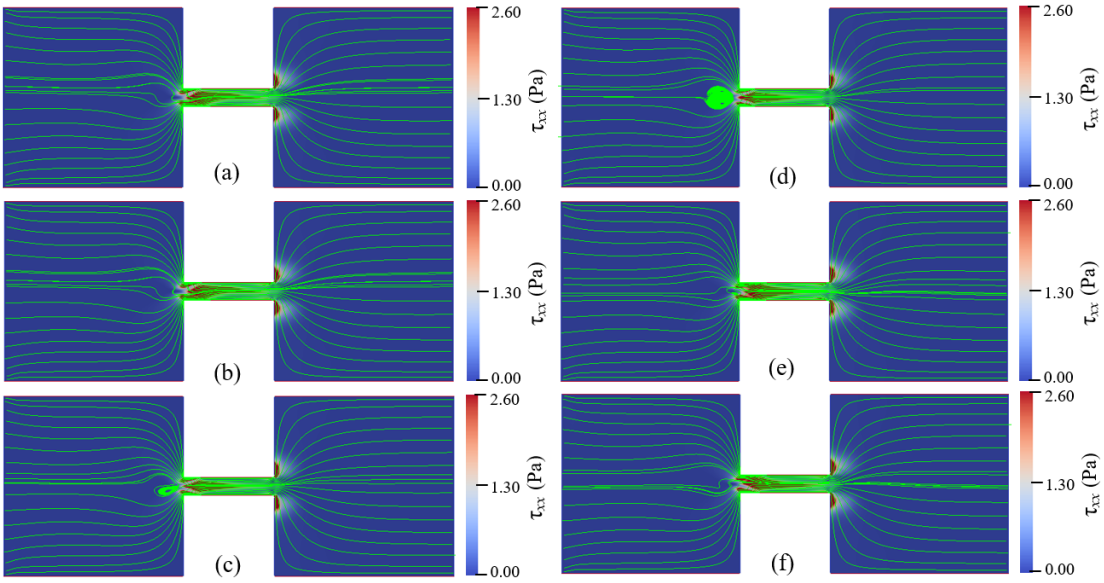

Figure 3.23 Streamlines of 150 ppm PAA solution under at E_{app} = 600 V/cm at different times: (a) 1.70 s, (b) 1.72 s, (c) 1.74 s, (d) 1.76 s, (e) 1.78 s, (f) 1.80 s. Zeta potential is −150 mV. The color bar represents the elastic normal stress τ_{xx}.

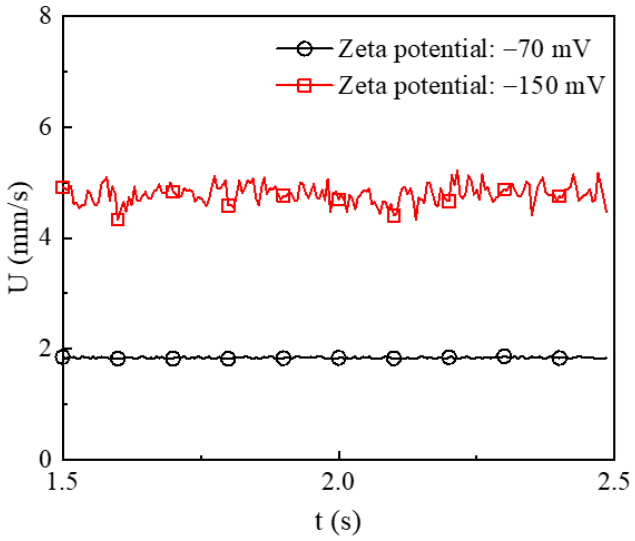

Figure 3.24 Velocity magnitudes at (0,0) for 150 ppm PAA solution with zeta potentials of −70 mV and −150 mV under E_{app} = 600 V/cm.

3.6 Conclusions

Electroosmotic flow (EOF) of viscoelastic fluid through a 10:1:10 constriction microchannel is numerically investigated as function of the applied electric field and the polymer concentration. In the current study, we neglect the effect of the polymer concentration on the zeta potential of the channel walls. Compared to the EOF of Newtonian fluid, the following distinct results for viscoelastic EOF through a 10:1:10 constriction microchannel are obtained:

(1) When polyacrylamide (PAA) concentration (applied electric field) exceeds a critical value, the EOF of viscoelastic fluid becomes time-dependent with upstream vortices occurring in the inlet reservoir near the entrance of the constriction microchannel. In contrast, the EOF of Newtonian fluid is always in a steady state without vortices.

(2) For the viscoelastic EOF, significant polymer stress is induced near the entrance within the constriction and near the downstream lips of the constriction, causing the elastic instabilities of the viscoelastic EOF. The induced polymer stress is dramatically magnified with the

increase of polymer concentration and applied electric field. However, the increase of polymer concentration shows a more significant enhancing effect on the polymer stress than the increase of the applied electric field.

(3) The EOF velocity of viscoelastic fluid within the constriction becomes temporally and spatially dependent. Near the exit of the constriction, due to the extrudate swell effect of the polymers, the velocity at the centerline first decreases at the exit followed by an increase in the outlet reservoir.

(4) The velocity at the exit of the constriction is higher than that at the entrance of the constriction because of the formation of upstream vortices, which is in qualitative agreement with experimental observation obtained from the literature.

(5) Under the same total viscosity and applied electric field, the velocity of Newtonian fluid is higher than that of viscoelastic fluid, which is attributed to the induced polymeric stress within the constriction. When the applied electric field is less than 300 V/cm, the Helmholtz-Smoluchowski velocity formula can predict the cross-sectional average velocity of viscoelastic fluid with PAA concentration up to 500 ppm, and the relative error is less than 5%. At a fixed PAA concentration, in general, the relative error of the Helmholtz-Smoluchowski approximation increases with an increase in the applied electric field.

CHAPTER 4

ELECTROOSMOTIC FLOW OF VISCOELASTIC FLUID THROUGH A MICROCHANNEL WITH 90° BENDS UNDER PULSATING ELECTRIC FIELDS

4.1 Introduction

Most previous research on electro-elastic instabilities is restricted to microchannels with straightforward geometries driven by direct current (DC) electric fields. However, the electro-elastic instabilities are found to be strongly related to high local velocity gradients in the microchannel, which can be resulted from special structures of the microchannel and the externally applied electric field. Therefore, based on the study in Chapter 3, the EOF of viscoelastic fluids through a microchannel with 90-degree bends is numerically studied. A constant DC electric field combined with AC electric fields with various amplitudes and frequencies are applied to the microchannel. OB model is adopted to describe the constitutive characteristics of PAA solutions and PB model is used to describe the electrokinetic phenomenon. Solutions with both low and high polymer concentrations are investigated. The polymer concentration, the amplitude and frequency of the AC electric field are shown to be correlated with the electro-elastic instabilities.

4.2 Geometry and mathematical model

The computational domain has the dimensions shown in Figure 4.1 in the O*xy* plane. Only 2D geometry is considered to reduce the computational burdens imposed by the unsteadiness. The working fluid is treated as incompressible monovalent binary electrolyte solution comprising ions such as K^+ and Cl^- with bulk concentration c_0 mixed with PAA polymer solution of concentration c_p. The solid walls of the microchannel and the reservoirs are assumed to carry a constant negative zeta potential, ξ_0. Two electrodes are placed at both ends of the reservoirs, and an external potential bias $U = U_0 + U_A\sin(2f_E\pi t)$ is applied between the inlet (Anode) and outlet (Cathode). The apparent

electric field between the inlet and outlet is defined as $E_{app} = U/(2L_r + L_C)$. The reservoir height H_r and the reservoir length L_r are 400 μm. The length of the microchannel is L_C = 200 μm, and the height of the microchannel is H_C = 20 μm.

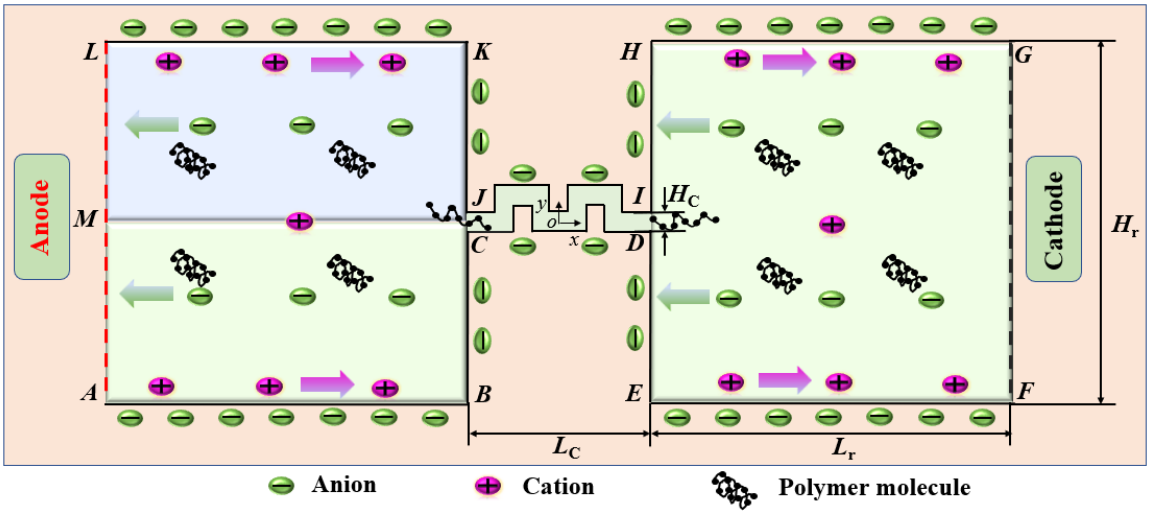

Figure 4.1 Schematic diagram of a microchannel with bends connecting two reservoirs at both ends. The solid walls of the reservoirs and the microchannel are negatively charged. DC and AC electric fields are imposed by applying a potential difference between anode and cathode positioned in two fluid reservoirs.

The set of governing equations of the problem are mostly the same as in Chapter 3, including the mass conservation equation, momentum equation, and the OB model. In addition, the dye concentration dynamics is numerically modeled as the transport of a passive scalar. The following convective-diffusive equation is solved to track the dye concentration in the computational domain,

$$\frac{\partial C}{\partial t} + \mathbf{u} \cdot \nabla C = D_{dye} \nabla^2 C, \tag{4.1}$$

where C is the dye concentration and D_{dye} is the diffusivity of the dye. In this study, D_{dye} is relatively small (4×10^{-11} m^2/s) and the Peclet number ($Pe = Hu/ D_{dye}$) is much large than one so that the convection effect dominates over the diffusion. A relatively low bulk concentration c_0 =

0.0001 mM is used in this study. The EDL thickness is 954 nm. The boundary conditions are given as follows (boundary conditions for study 2 are shown in Figure D.1 in Appendix D):

(1) At the Anode (edge AML in Figure 4.1): $\mathbf{n}\cdot\nabla\mathbf{u} = 0$; $p = 0$; $\boldsymbol{\tau} = \mathbf{0}$; $\phi_{Ext} = U_0 + U_A\sin(2f_E\pi t)$; $\mathbf{n}\cdot\nabla\psi = 0$; $\boldsymbol{\Theta} = \mathbf{0}$; $C = 1$ at edge ML; C = 0 at edge AM; where **n** denotes the normal unit vector on the surface.

(2) At the Cathode (edge FG in Figure 4.1): $\mathbf{n}\cdot\nabla\mathbf{u} = 0$; $p = 0$; $\mathbf{n}\cdot\nabla\boldsymbol{\tau} = 0$; $\phi_{Ext} = 0$; $\mathbf{n}\cdot\nabla\psi = 0$; $\mathbf{n}\cdot\nabla\boldsymbol{\Theta} = 0$; $\mathbf{n}\cdot\nabla C = 0$.

(3) On the reservoir walls and the microchannel walls: $\mathbf{u} = \mathbf{0}$; $\mathbf{n}\cdot\nabla\phi_{Ext} = 0$; $\psi = \xi_0$; $\mathbf{n}\cdot\nabla\boldsymbol{\Theta} = 0$; $\mathbf{n}\cdot\nabla C = 0$; $\mathbf{n}\cdot\nabla p$ is obtained from the momentum equation; the components of $\boldsymbol{\tau}$ are linearly extrapolated.

The following initial conditions are specified within the domain: $\mathbf{u} = \mathbf{0}$; $p = 0$; $\boldsymbol{\tau} = \mathbf{0}$; $\phi_{Ext} = 0$; $\psi = 0$; $\boldsymbol{\Theta} = \mathbf{0}$; $C = 1$ in the upper half of the inlet reservoir (the shaded area of the inlet reservoir in Figure 4.1); and $C = 0$ in the rest of the computational domain.

The meshing tool blockMesh provided in OpenFOAM is used to create structural mesh in the computational domain as seen in Figure 4.2. The geometry at the 90° corners is slightly rounded to prevent the electric field singularity at corners of the geometry. Refined mesh is dispersed close to the charged walls, and the cells are compressed toward the walls, assuring the employment of at least 10 cells within the EDL to resolve the strong gradients that have emerged inside the EDL in the proximity of the charged walls. The EDL thickness is 954 nm in this study. The edge size of the layer of cells adjacent to the walls is 25 nm and there are 15 cells inside the EDL. The mesh has a total of 543,976 cells. A mesh independence study, described in the next section, is performed to ensure the accuracy of the simulation.

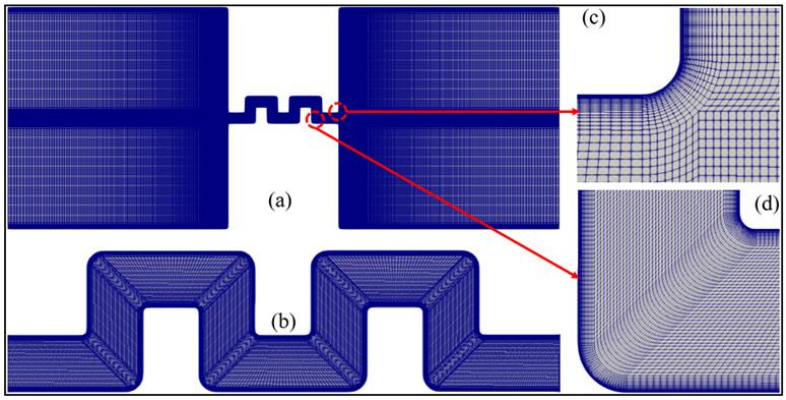

Figure 4.2 Computational mesh used in the numerical simulations. Mesh of the whole geometry (a) and detailed view of the mesh in the microchannel (b), at the channel corner (c), and at the 90° bends of the microchannel (d).

In this work, the adopted η_p and λ for 100 ppm, 250 ppm, and 500 ppm PAA-water solutions were experimentally measured [183], and the slow retraction method was used to measure the relaxation time. The values of η_p and λ used in this work are listed in Table 1. The zeta potential ξ_0 is −110 mV. The solvent dynamic viscosity η_s is 0.001 kg/(m·s). The external potential bias is $U = U_0 + U_A\sin(2f_E\pi t)$. And the apparent electric field is defined as $E_{app} = U/(2L_r + L_C) = E_0 + E_A\sin(2f_E\pi t)$, where E_0 is the EC electric field (i.e., V/cm); E_A is the amplitude of the AC electric field (i.e., $0.1E_0$, $0.2E_0$, and $0.4E_0$); f_E is frequency of the AC electric field (i.e., 4 Hz, 6 Hz, 8 Hz, and 10 Hz). A thorough code validation of the solver was performed in Chapter 3.

Table 4.1 Parameters of PAA-solutions.

c_p (ppm)	100	250	500
η_p (kg/(m·s))	0.00222	0.00555	0.0111
λ (s)	0.0086	0.0196	0.0476

4.3 Mesh Independence Study

Three different meshes are used to perform a mesh independence study for c_p = 100 ppm, E_A = 0.1E_0 and f_E = 10 Hz. There are 543976, 610656, and 748236 cells in mesh 1, mesh 2, and mesh 3, respectively. Figure 4.3 shows the detailed views near the charged walls of the three meshes. For mesh 1, the meshes near the charged walls are 25 nm, and there are 15 cells within the EDL thickness. In mesh 2, the cells within the EDL thickness are the same as mesh 1, however the cells far away from the charged walls are slightly refined. In mesh 3, the cells near the charged walls are 20 nm, and there are 20 cells within the EDL thickness. The cells far away from the charged walls are the same as mesh 2. Figure 4.4 shows the spatial distribution of the dye concentration and the streamlines of three different meshes at t = 1 s. The results of three different meshes show no notable difference.

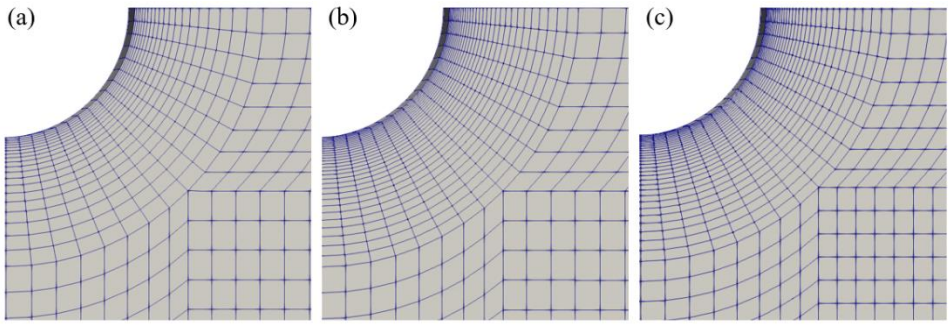

Figure 4.3 Detailed views near the charged wall of the three different meshes used for the mesh independence study: (a) mesh 1: 543976 cells, (b) mesh 2: 610656 cells, (c) mesh 3: 748236 cells.

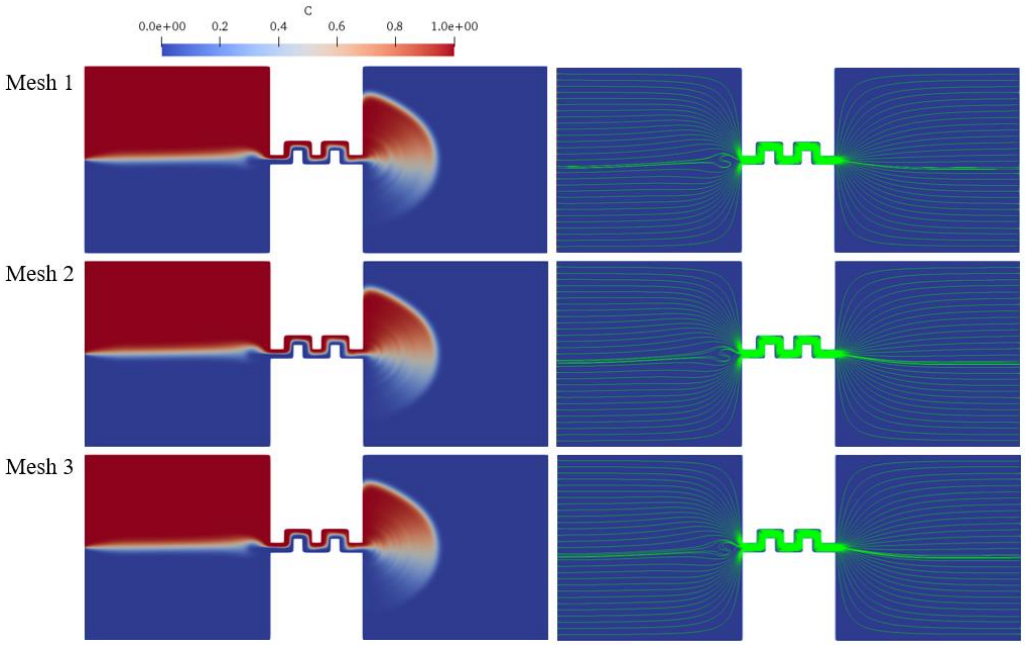

Figure 4.4 Spatial distribution of dye concentrations (left column) and streamline (right column) for mesh 1 (the top row), mesh 2 (the middle row), and mesh 3 (the bottom row) at t = 1 s.

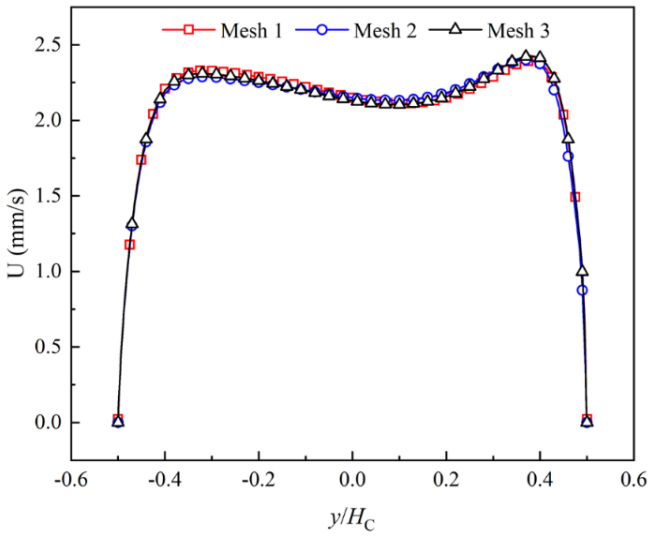

Figure 4.5 Velocity profile at x = 0, t = 1 s of the three different meshes.

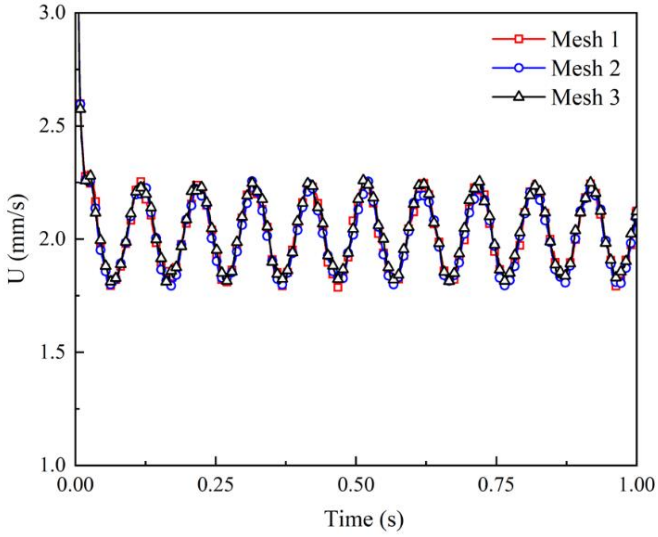

Figure 4.6 Plot of cross-sectional average velocities at $x = 0$ in the microchannel of three different meshes.

Figure 4.5 plots the velocity profiles at $x = 0$ for three different meshes at $t = 1$ s, which show great consistency in the cross-section. Comparing with mesh 1, the maximum relative difference is 1.42 % at $y/H_C = 0.4$ for mesh 2 and 1.67 % at $y/H_C = -0.3$ for mesh 3. The average relative differences for mesh 2 and mesh 3 are 0.94 % and 0.75 %, respectively. Figure 4.6 shows the cross-sectional average velocities at $x = 0$ in the microchannel of the three different meshes from $t = 0$ s to $t = 1$ s, which is calculated by $U = \int_{-H_C/2}^{H_C/2} U(0, y)\,dy / H_C$. Within 1 s, the three average velocities are nearly identical with a maximum relative difference of 3.92 % for mesh 2 and 3.76 % for mesh3. The average relative differences for mesh 2 and mesh 3 are 0.91% and 1.03 %, respectively. The three different meshes show great agreement in predicting the velocity field in the microchannel. Therefore, mesh 1 is used for other simulations.

4.4 Results and discussions

In this section, the flow characteristics of the EOF through a constriction micro-channel with 90° bends are attained when imposed to constant and pulsating electric fields for Newtonian and viscoelastic fluids. Under a steady electric field, elastic instabilities are observed in the viscoelastic EOF, and the pulsating electric fields amplify the instabilities even more. The following analysis discusses the elastic instabilities from three aspects: (a) velocity fluctuation and energy spectra of the velocity fluctuation, (b) flow patterns revealed by the streamlines, (c) particle trajectories in the downstream reservoir. The strength and frequency of the pulsating electric field are given particular focus.

4.4.1 Velocity and energy spectra of velocity fluctuations

We first analyze the velocity of the EOF at the center of the microchannel (i.e., (0,0)). The EOF of a Newtonian fluid with the same total viscosity as 200 ppm PAA solution is studied as a reference. Figure 4.7 shows a plot of the velocities of the Newtonian fluid and PAA solutions when the microchannel is under DC electric field. The Weissenberg numbers of the viscoelastic EOF investigated in this study are all around 1, namely, Wi = 0.86, 0.98, and 1.19 for 100 ppm, 250 ppm, and 500 ppm PAA solutions, respectively. As shown in Figure 4.7a, under DC electric field, the velocity of the Newtonian fluid is steady and time independent while all velocities of the PAA solutions show fluctuations. PAA solution with less polymer concentration has higher velocity due to less viscosity. Figure 4.7b shows the energy spectra of velocity fluctuations at the center of the microchannel. The three energy spectra curves share the same general appearance: there is a plateau at low frequency followed by two continuous power-law decay regions separated by a distinct inflection point. The exponents are rather close for all three energy spectra curves, around

−2.6 at lower frequencies and around −6.3 in the high-frequency region. Apart from the inflection points, none of the curves exhibit any significant peaks.

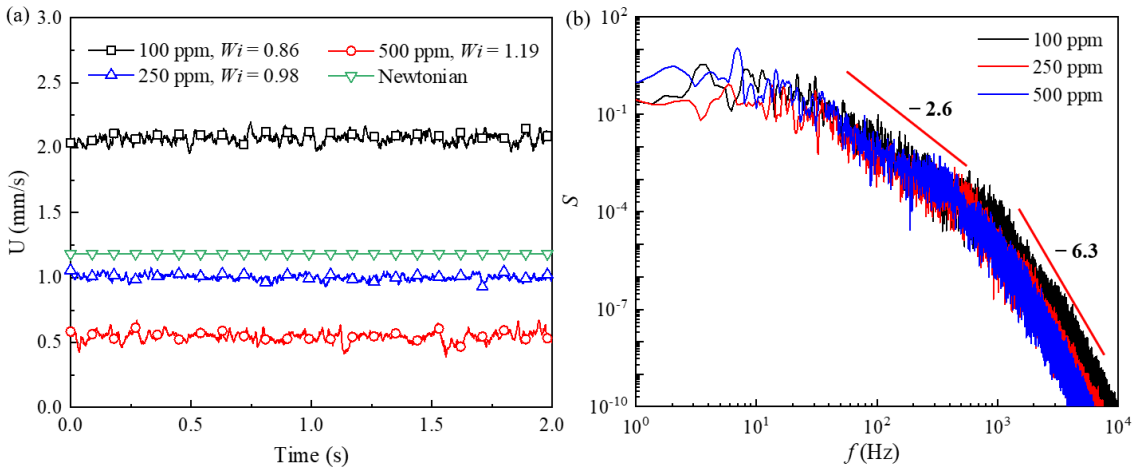

Figure 4.7 Velocities at the center of the microchannel of Newtonian fluid with the same total viscosity as 250 ppm PAA solution, and c_p = 100 ppm, 250 ppm, 500 ppm PAA solutions under DC electric field: (a) velocity magnitude plots at the center of the microchannel, (b) energy spectra of the velocity fluctuations.

In Figure 4.8 we plot the velocities of 100 ppm PAA solution when f_E is 10 Hz and E_A varies from 0 to 0.4E_0. When AC electric field is applied, the velocity at the center of the microchannel fluctuates in the same frequency as the AC electric field. In the upper left of Figure 4.8, a closer view of the velocities reveals that, in addition to electric field's influence, there are small fluctuations in the velocities originating from the elastic instabilities, which will be discussed in the following sections. In the following discussions, to distinguish between the large velocity fluctuation due to the AC electric field and the small velocity fluctuation originating from the elastic instabilities, the former is referred to as the main fluctuation and the latter is called the minor fluctuation. The statistical outcomes of the velocities in Figure 4.8 are shown in Figure 4.9. As shown in Figure 4.9a, for AC electric field with different amplitudes, the averages of the

velocities show no significant difference (i.e., < 2%). The amplitudes of the velocities increase linearly as the increasing of the amplitudes of the AC electric field. Figure 4.9b shows the energy spectra of the velocity magnitude fluctuations. A distinct peak at 10 Hz is observed in the energy spectra, which is due to the main frequency of the AC electric field. The peak energy at 10 Hz increases with the increasing amplitude of the AC electric field. Except for the main peak, the energy spectra curves share similar features. Two continuous power-law decay regions are observed with exponents of about −2.6 at lower frequencies and −5.5 at higher frequencies.

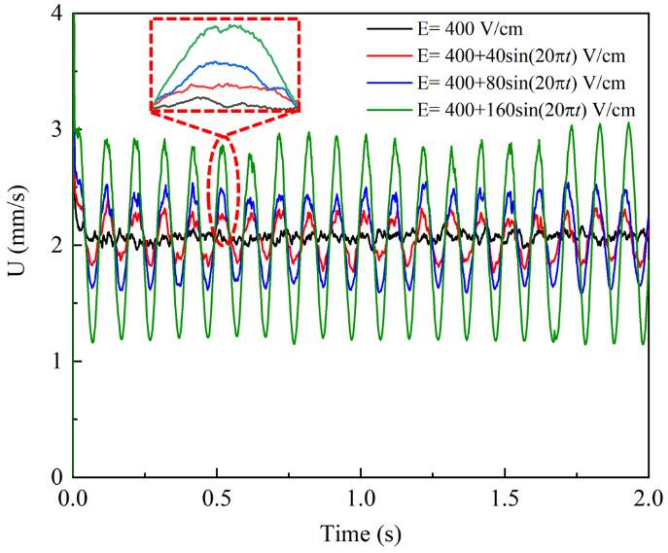

Figure 4.8 Velocities at the center of the microchannel for c_p = 100 ppm at f_E = 10 Hz, and E_A = 0, 0.1E_0, 0.2E_0, 0.4E_0.

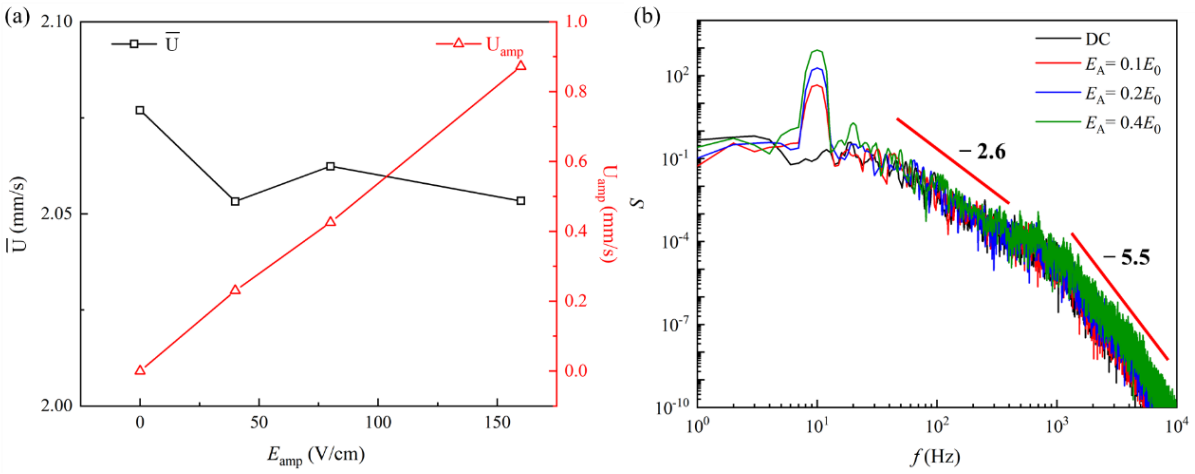

Figure 4.9 Statistical results for c_p = 100 ppm at f_E = 10 Hz, and $E_A = 0.1E_0$, $0.2E_0$, and $0.4E_0$: (a) average velocities and the velocity amplitudes, (b) energy spectra of the velocity fluctuations.

Additionally, the velocities of 250 ppm PAA solution at the center of the microchannel (i.e., (0,0)) under DC and AC electric fields are presented in Figure 4.10. The amplitude of AC electric field is $E_A = 0.1E_0$, and the frequency f_E varies from 4 Hz to 10 Hz. The velocities show minor fluctuation for both DC and AC electric fields. The minor fluctuation is more significant under DC electric field and AC electric field with relatively low frequencies (i.e., 4 Hz and 6 Hz). With the increase of the frequency of the AC electric field, the minor fluctuation of the velocity becomes unsignificant. The statistical outcomes of the velocities in Figure 4.10 are displayed in Figure 4.11a. When the amplitude of the AC electric field is fixed and the frequency varies, the relative difference of the average velocity is less than 1%, which is negligible. The main fluctuation, however, exhibits the opposite tendency from the minor fluctuation in that its amplitude grows as the frequency rises. Figure 4.11b plots the energy spectra of the velocity fluctuations. Except for the distinct peak of the main frequency of the AC electric field, the energy spectra curves are rather similar to under DC electric fields, a plateau at low-frequency region followed by two continuous power-law decay regions separated by an inflection point. The exponents are very close for

different frequencies, around −2.7 at lower frequencies, and around −5.7 at the high-frequency region. The energy spectra of the 500 ppm PAA solution's velocity fluctuation are presented in Figure 4.12. Figure 4.12a shows the general characteristics of the energy spectra at three different points in the microchannel. At low frequencies, the exponents are around −3.2 and at high frequencies, they are roughly −5.7. Figure 4.12b presents the energy spectra of the velocity fluctuations when the amplitude of the AC electric field is relatively high (E_A = 0.4E_0), which shows similar features as in Figure 4.12a, with exponents around −2.9 at lower frequencies, and around −4.1 at high frequencies.

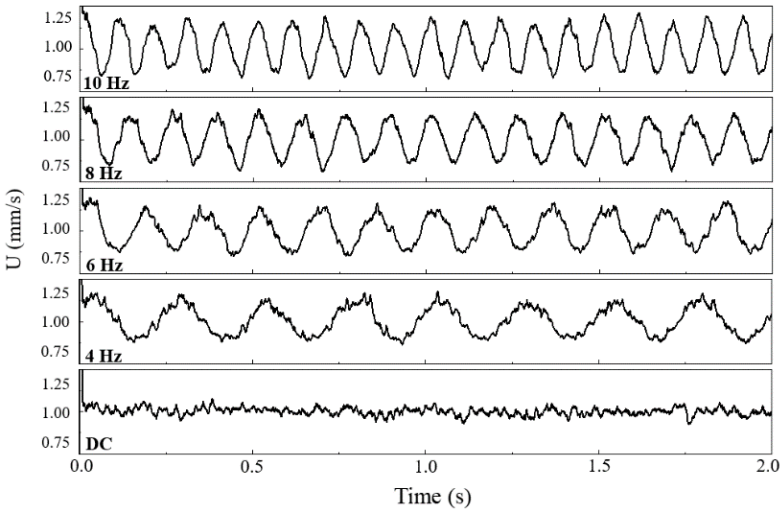

Figure 4.10 Velocities at the center of the microchannel for c_p = 250 ppm under DC electric field and AC electric fields at E_A = 0.1E_0, and f_E = 4, 6, 8, and10 Hz.

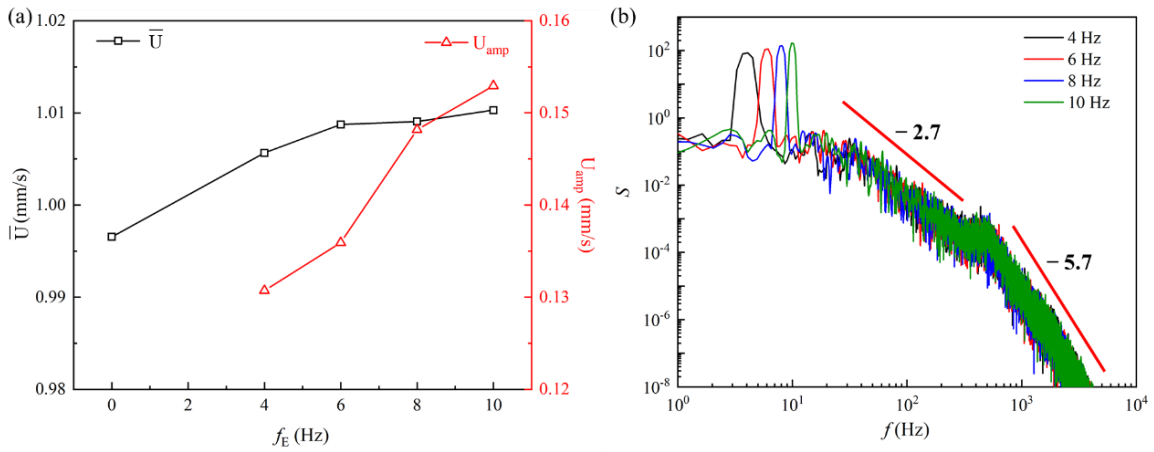

Figure 4.11 Analysis of velocity for c_p = 250 ppm under AC electric field at $E_A = 0.1E_0$ and f_E = 4, 6, 8, and10 Hz: (a) statistical results of average velocity and velocity amplitude, (b) energy spectra of velocity fluctuation.

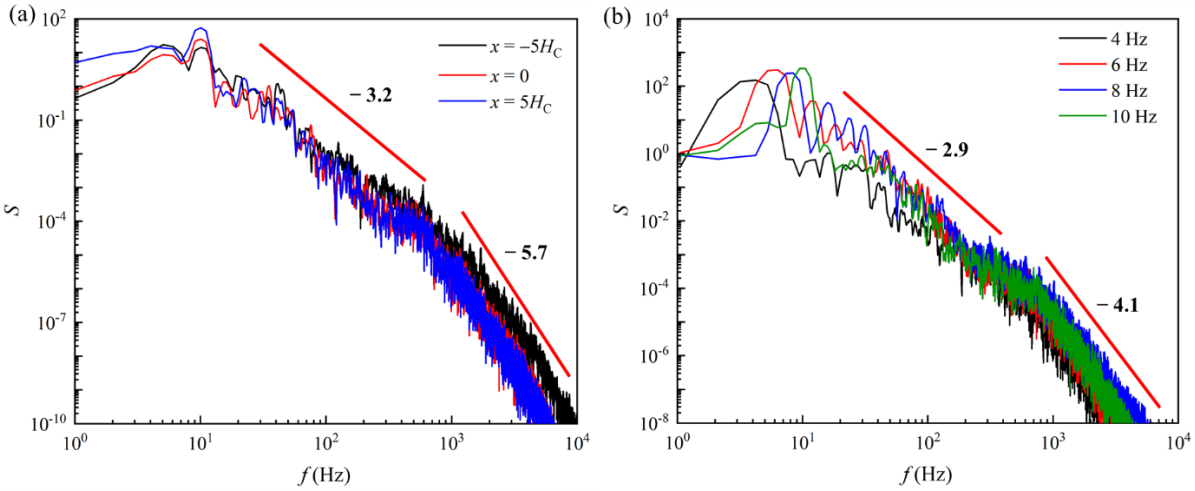

Figure 4.12 Energy spectra of the velocity fluctuation for c_p = 500 ppm: (a) energy spectra at three locations in the microchannel at $E_A = 0.1E_0$ and f_E = 10 Hz, (b) energy spectra at $E_A = 0.4E_0$ and f_E = 4, 6, 8, and10 Hz.

All energy spectra curves investigated in this study display power-law decay over a wide range of frequencies, with exponents varying from −2.3 to −3.2 at low frequencies and from −4.1 to −6.3

at high frequencies. According to Groisman and Steinberg [191], elastic turbulence is characterized by flow perturbations over a wide range of temporal and spatial scales with increasing transfer rate of standard quantities (momentum, heat and mass). In their study, Groisman and Steinberg [191] observed evidence of the first feature: the energy spectra of velocity fluctuations displayed a power-law decay over a wide range of frequencies and wavelengths with exponents between −2 and −4. Several later works claimed that exponent larger than 3 in spectral analysis is a characteristic of the elastic turbulence [192, 193], which was also reported in theoretical studies [194, 195]. The energy spectra curves of the velocity fluctuations in this study show similar features as aforementioned literatures, which indicates the existence of elastic turbulence regime in the viscoelastic EOF.

4.4.2 Flow patterns

In Chapter 3, the flow patterns of a constriction straight channel are found to be highly dependent on the polymer concentrations and the applied electric field. In this study, the AC electric field shows a similar influence on the flow pattern of the viscoelastic EOF. Due to the existence of the DC and AC electric fields, the absolute value of E_{app} is not fixed but changes rapidly, which magnifies the instabilities in the flow. Figure 4.13 depicts the streamlines for 100 ppm PAA solution under DC electric field at E_{app} = 400 V/cm from 1 s to 1.1 s. Two small time-dependent vortices are observed in the inlet reservoir near the inlet of the microchannel. The diameter of the vortices is about the height of the microchannel (i.e., 20 μm). Such vortices were reported and analyzed in the study in Chapter 3. Apart from the formation and disappearance of the upstream vortices, slight fluctuations of the streamlines along the centerline of the inlet and outlet reservoirs are observed. In comparison, Figure 4.14 shows the streamlines for 500 ppm PAA solution under DC electric field at E_{app} = 400 V/cm from 1 s to 1.1 s. Compared with 100 ppm

PAA solution, two much larger circulations with diameters about 3.5 times of the height of the microchannel (i.e., 70 μm) are observed in the inlet reservoir near the entrance of the microchannel. The direction of the circulation is marked by red curved lines. The pair of vortices are in opposite directions and a large stagnant region is formed right before the entrance of the microchannel. At different times the pair of vortices show no significant change in size. The streamlines are smooth in the inlet reservoir far from the microchannel and in the whole outlet reservoir. However, stronger fluctuation can be observed in the streamlines along the centerline of the two reservoirs. The fluctuation of the streamlines in the inlet reservoir is due to the instability induced by the vortices, while the fluctuation in the outlet reservoir is caused by the instability at the outlet of the microchannel. Compared with 100 ppm PAA solution, 500 ppm PAA solution displayed stronger instability under the same DC electric field at E_{app} = 400 V/cm. Figure 4.15 shows the streamlines for 500 ppm PAA solution under DC and AC electric fields at $E_A = 0.4E_0$ and f_E = 10 Hz from 1 s to 1.1 s. Within 0.1 s, the size of the vortices grows first and then decreases dramatically due to existence of the AC electric field. Apart from the change of size, the orientation of the vortices shows strong fluctuation, which can also be observed in the fluctuation of the streamlines upstream the vortices. In the outlet reservoir, fluctuation in the streamlines along the center line of the reservoir is observed. The application of the AC electric field induces stronger instabilities in the streamlines compared with DC electric field only.

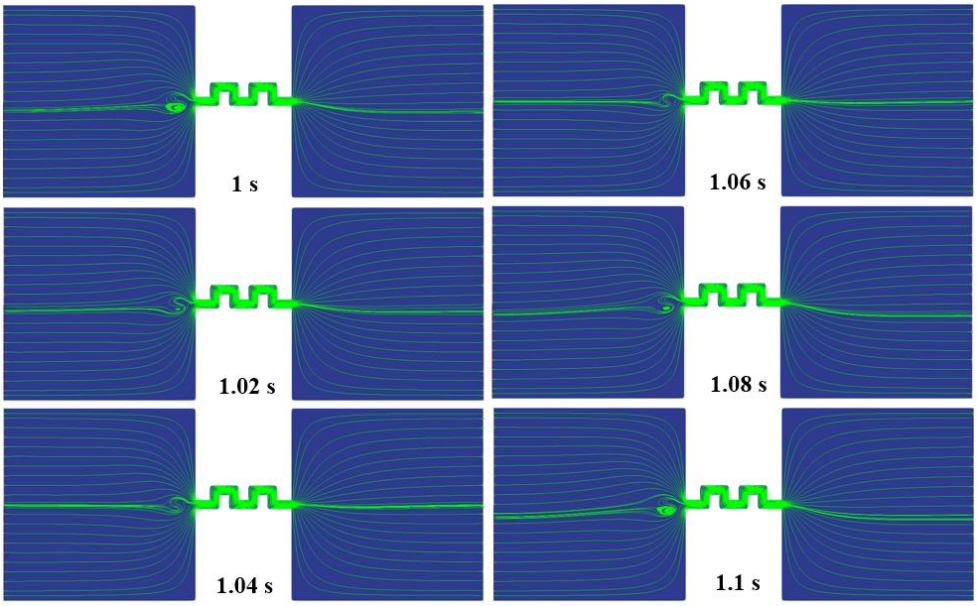

Figure 4.13 Streamlines for c_p = 100 ppm under DC electric field at $E_{app} = E_0$ from 1 s to 1.1 s.

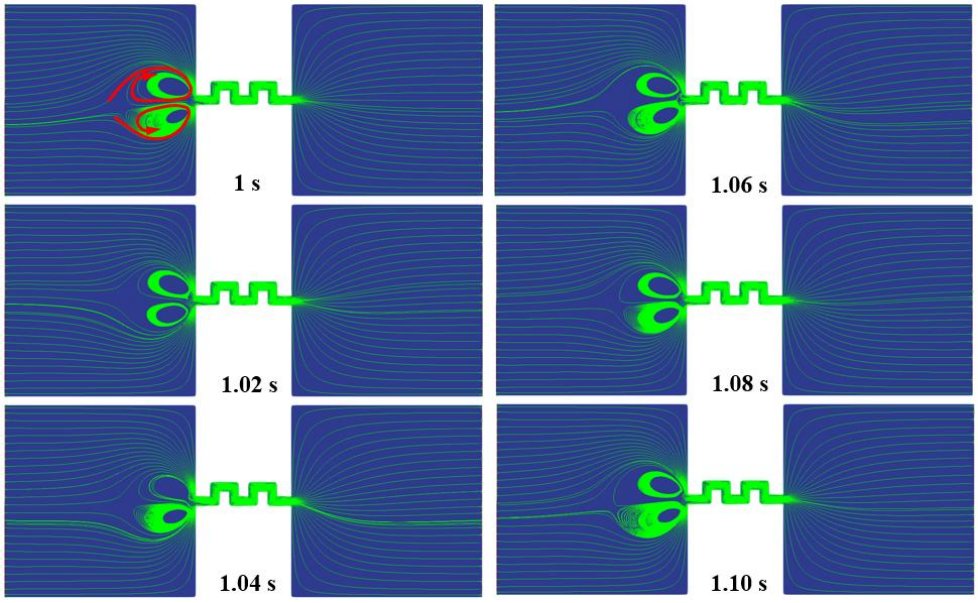

Figure 4.14 Streamlines for c_p = 500 ppm under DC electric field at $E_{app} = E_0$ from 1 s to 1.1 s.

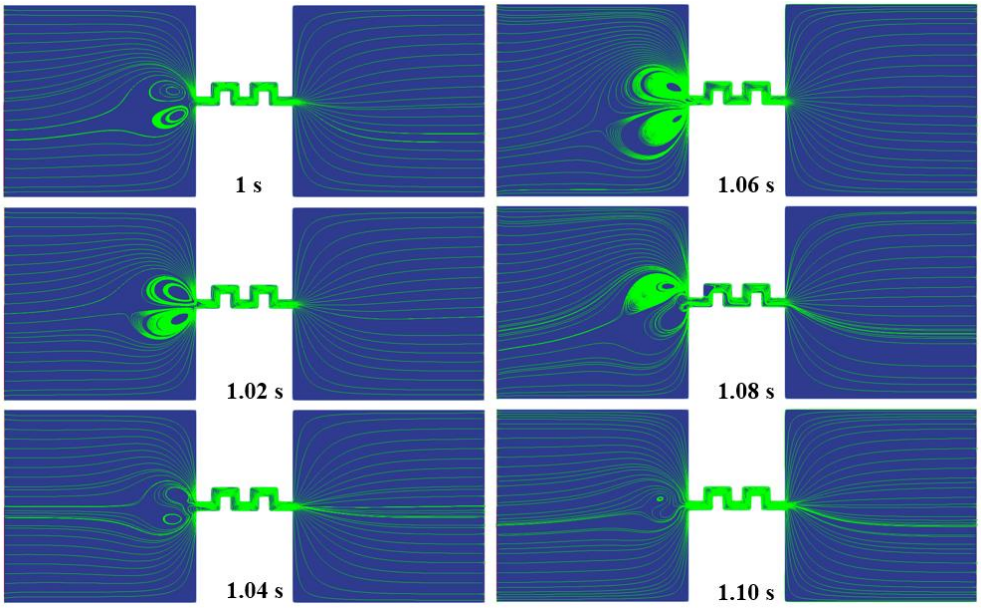

Figure 4.15 Streamlines for c_p = 500 ppm under AC electric field at $E_A = 0.4E_0$ and f_E = 10 Hz from 1 s to 1.1 s.

To better visualize the flow behavior and the elastic turbulence regime, the upper half of the inlet reservoir is mixed with a dye of finite concentration, whereas the fluid in the lower half of the inlet reservoir has a zero-dye concentration. A relatively small diffusivity (D_{dye}) is adopted in this study so that the convection effect dominates over the diffusion. Figure 4.16 shows the dye patterns of Newtonian fluid with the same total viscosity as 250 ppm PAA solution at different times. The EOF of Newtonian fluid shows no instability. The upper half of the microchannel is filled with dyed fluids, while the lower half of the microchannel is filled with fluids with zero dye concentration. A distinctive, smooth, and time-independent dividing line can be observed in the microchannel between the dyed and undyed fluids, which implies that the EOF of Newtonian fluid is steady and time-independent. Figure 4.17 shows the dye patterns for c_p = 250 ppm at $E_A = 0.4E_0$ and f_E = 10 Hz. Compared with the dye patterns of the Newtonian fluid, the dye patterns in Figure 4.17 show less stable and distinctive dividing lines in the microchannel between the dyed and

undyed fluids. In the left half of the microchannel, a relatively clearer dividing line can be observed compared with the right half of the microchannel due to the 90° bends of the microchannel, which generate curvilinear streamlines in the microchannel and induce the elastic instabilities. Such elastic instabilities are often observed in flows with sufficient curvature, and some argue that curvature is necessary for infinitesimal perturbations to be amplified by the normal stress imbalances in the viscoelastic flows [34, 187, 189]. In order to describe the change of dye patterns at different locations in the microchannel, Figure 4.18 presents the statistical results of dye concentration distribution for PAA solutions and Newtonian fluid at three different cross-sections of the microchannel. For all the solutions investigated, the dyed fluid flows from the inlet reservoir to the outlet reservoir through the microchannel in less than 1 s. Therefore, a time average of the dye concentration C is calculated from 1 s to 3 s to avoid the influence of the flow fluctuation. As shown in Figure 4.18a, at the first cross-section (x = −80 μm) PAA solutions and Newtonian fluid share similar dye concentration distribution: C starts from 0 near the lower channel wall (y = −10 μm) with a sharp increase to 1 near the upper channel wall. For the Newtonian fluid, at the second and third cross sections (x = 0 μm and −80 μm) C is nearly zero at the lower channel wall (y = −10 μm) and increases to 1 with a relatively smaller slope compared with the at the first cross-section. However, the dye patterns for the Newtonian fluid at three cross-sections show no significant differences. For the 250 ppm and 500 ppm PAA solutions, however, the dye concentration distribution is found to be strongly related to the position of cross-sections. At the second cross-section (x = 0 μm), C is more evenly distributed than at the first cross-section, and at the third cross-section (x = −80 μm), C shows the most even distribution. Such a trend is more observable in the 500 ppm PAA solution than in the 250 ppm PAA solution, which is due to the stronger viscoelastic effect. In Figure 4.18b, we plot the standard deviation of the dye concentration (S_C) at

the three cross-sections. A smaller standard deviation implies a more even dye concentration distribution across the microchannel. S_C decreases with the increasing section number (i.e., increasing 90° bends) and polymer concentrations. The dye patterns in the outlet reservoir of PAA solutions also show difference from the Newtonian fluid. The dye concentration for Newtonian fluid changes smoothly in the outlet reservoir and no significant perturbation is observed. However, for the 250 ppm PAA solution, under the AC electric field, the dyed fluid is in a wavy appearance in the outlet reservoir, which originates from the flow fluctuation at the outlet of the microchannel.

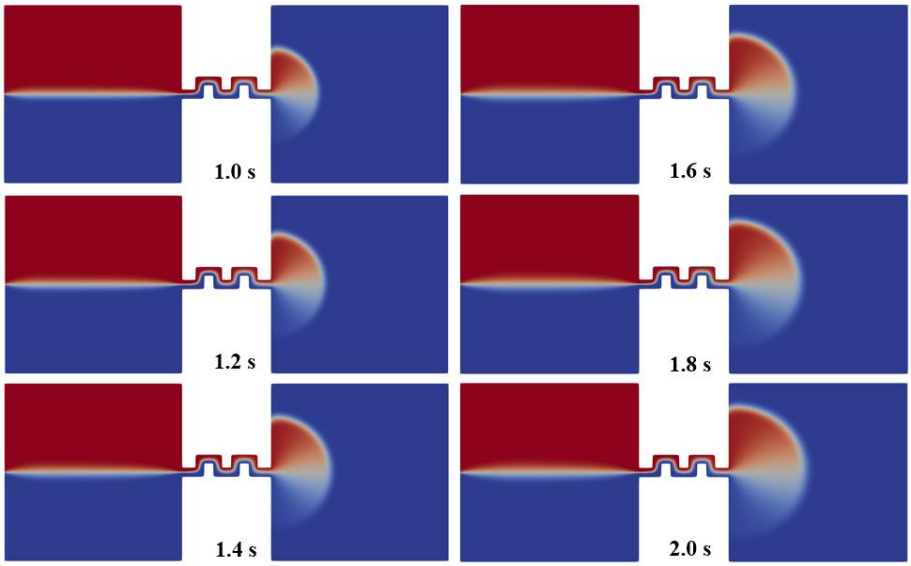

Figure 4.16 Dye patterns for Newtonian fluids with the same total viscosity as 250 ppm PAA solution at different times.

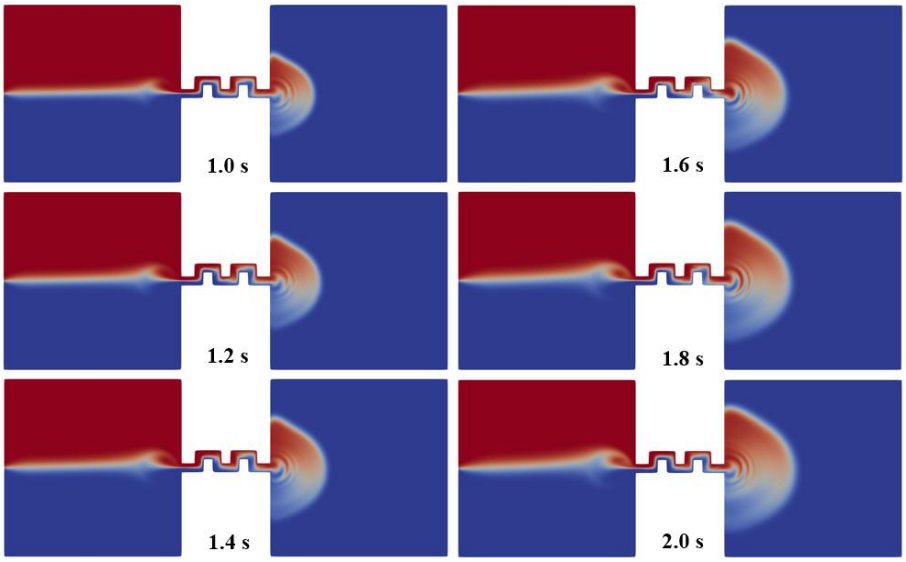

Figure 4.17 Numerical dye patterns for c_p = 250 ppm at $E_A = 0.4E_0$, f_E = 10 Hz.

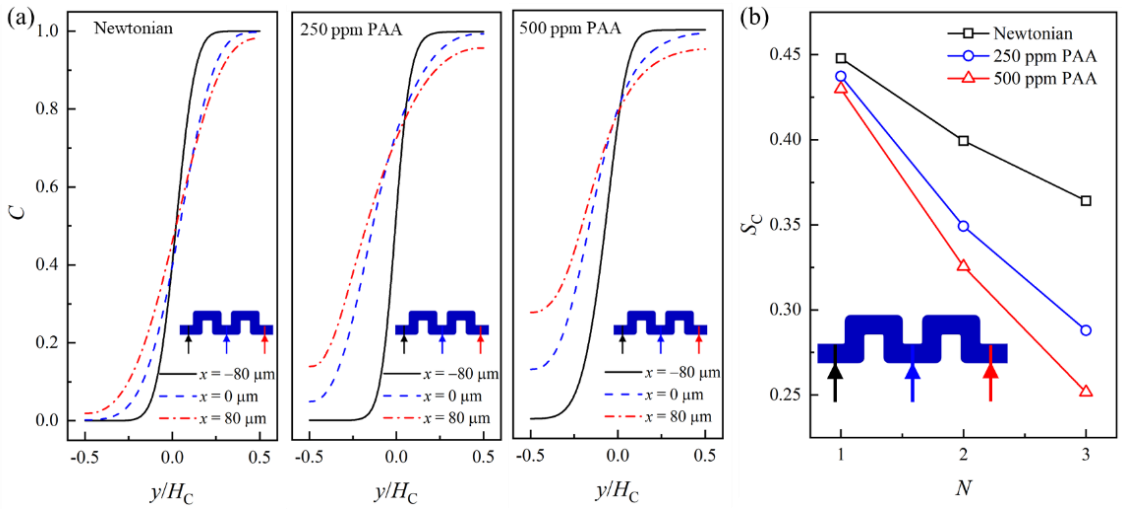

Figure 4.18 Dye concentration profile at different cross-sections of the micro channel: (a) dye concentration distribution of Newtonian fluid with same total viscosity as 250 ppm PAA solution, 250 ppm PAA solution, and 500 ppm PAA solution at three different cross-sections of the microchannel at $E_A = 0.4E_0$, f_E = 10 Hz, (b) standard deviation of the dye concentration C.

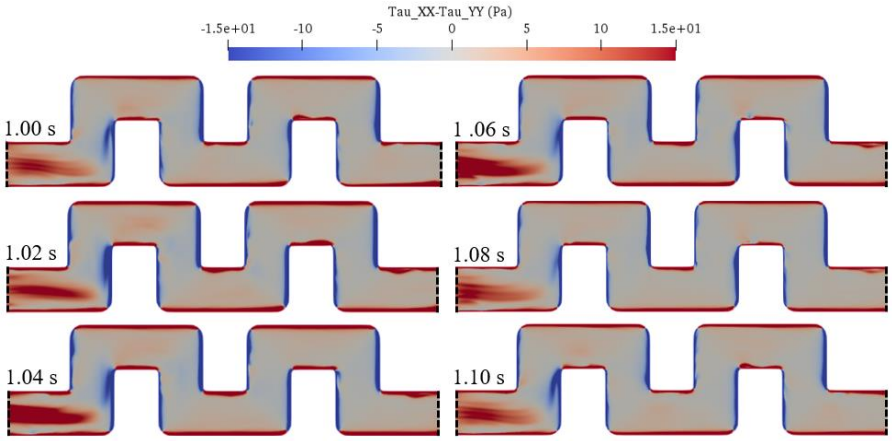

Figure 4.19 First normal stress difference N1 for c_p = 500 ppm at $E_A = 0.4E_0$, f_E = 10 Hz from 1 s to 1.1 s.

Figure 4.19 depicts the spatial distribution of the first normal stress difference N1($\tau_{xx} - \tau_{yy}$) in the microchannel of 500 ppm PAA solution at different times. Near the entrance of the microchannel, a significant positive increase of N1 is induced, which implies that the polymer molecules experience strong extension in the *x*-axis direction, whereas in the *y*-axis direction, the polymer molecules are relatively compressed. Such distribution of N1 near the entrance of the microchannel is due to the high velocity gradient at the entrance originating from the contraction geometry. When the microchannel is parallel to the *x*-axis, a rapid positive increase of N1 is observed in the adjacent to the walls of the microchannel, and such increase of N1 is negative when the microchannel is parallel to the *y*-axis. The distribution of N1 near the walls of the microchannel suggests that the polymer molecules are intensively stretched in the flow direction near the channel walls within a rather thin layer. Such phenomenon is due to the existence of EDL in the EOF. Within the EDL, which is a rather thin layer near the charged walls of the microchannel, the EOF velocity rapidly increases from zero to the maximum, resulting in a high velocity gradient in the flow direction. Therefore, the polymer molecules are always stretched in the flow direction near the charged channel walls. In the microchannel far away from the entrance and the channel

walls, N1 shows slightly positive, meaning that the polymer molecules are relatively more stretched in the *x*-axis direction than in the *y*-axis direction. The regions with high values of N1 in the microchannel fluctuate significantly with the changing of the E_{app}, which amplifies the instabilities of the viscoelastic EOF.

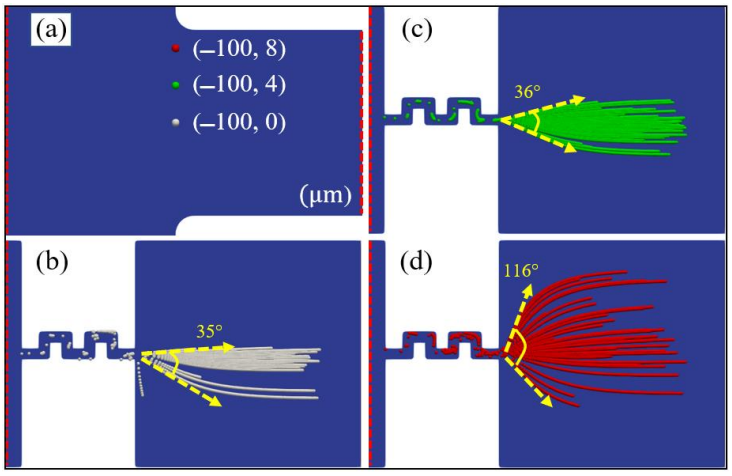

Figure 4.20 Particle path from three locations in the microchannel for c_p = 100 ppm at $E_{app} = E_0$: (a) coordinates of the three source points in the microchannel, (b) particle paths originating from (−100 μm, 0 μm), (c) particle paths originating from (−100 μm, 4 μm), (d) particle paths originating from (−100 μm, 8 μm).

Particle paths through the microchannel are extracted to study the instabilities of the viscoelastic EOF. As shown in Figure 4.20a, three locations are selected to generate the particle paths. Figure 4.20b, c, and d show the particle paths of 100 ppm PAA solution under DC electric field. The particle paths show a jet-like appearance in the outlet reservoir with different opening angles related to the location of the source point. For example, in Figure 4.20, the opening angles of the flow jet are measured to be 35°, 36°, and 116° for the three locations. The particles originating from the location far from the center line of the microchannel show a larger opening angle in the

outlet reservoir than the particles near the centerline, suggesting that the viscoelastic EOF experiences stronger perturbation at locations far from the center line of the microchannel and near the walls of the microchannel. Figure 4.21 depicts the particle paths of 100 ppm PAA solution originating from (−100 μm, 4 μm) under AC electric fields with different amplitudes (E_A = 0, 0.1E_0, 0.2E_0, and 0.4E_0) but the same frequency (f_E = 8 Hz). The opening angles of the particle paths in the outlet reservoir are measured to be 36°, 57°, 73°, and 123°, which are found to increase with the increasing amplitude of the AC electric field. Within the microchannel, the particles are more evenly distributed in the cross direction of the microchannel when under AC electric field with a higher amplitude. And the same trend can also be observed after particles passing through more 90° bends of the microchannel. For example, in Figure 4.21d, particles in the microchannel are more scattered than in Figure 4.21a, b, and c. In the right half of the microchannel, particles fill more of the microchannel than in the left half of the microchannel. The result in Figure 4.21 implies that the elastic instabilities of the EOF are significantly amplified by the increasing amplitude of the AC electric field and the 90° bends of the microchannel. Similar features are also found in the particle paths originating from the center of the microchannel (−100 μm, 0 μm) as shown in Figure 4.22. It should be mentioned that in Figure 4.22b, the opening angle is 140°. However, the majority of the particles are within a smaller angle (104°) as indicated by the red lines in Figure 4.22b.

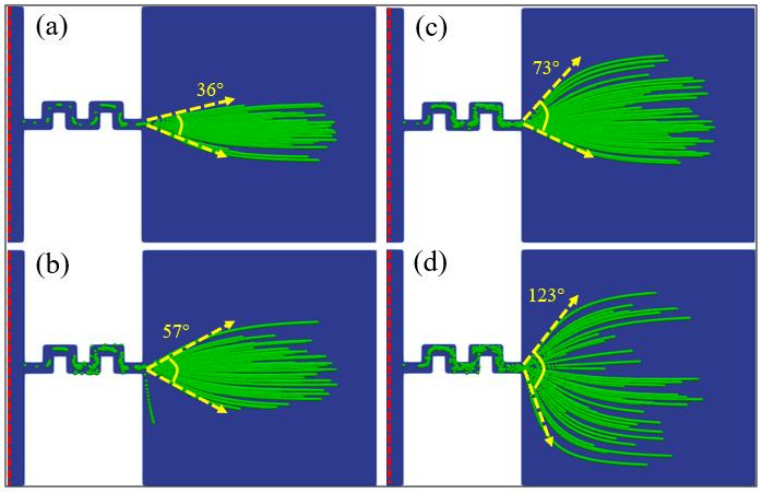

Figure 4.21 Particle paths of 100 ppm PAA solutions originating from (−100 μm, 4 μm) at: (a) $E_{app} = E_0$, (b) $E_A = 0.1E_0$, $f_E = 8$ Hz, (c) $E_A = 0.2E_0$, $f_E = 8$ Hz, (d) $E_A = 0.4E_0$, $f_E = 8$ Hz.

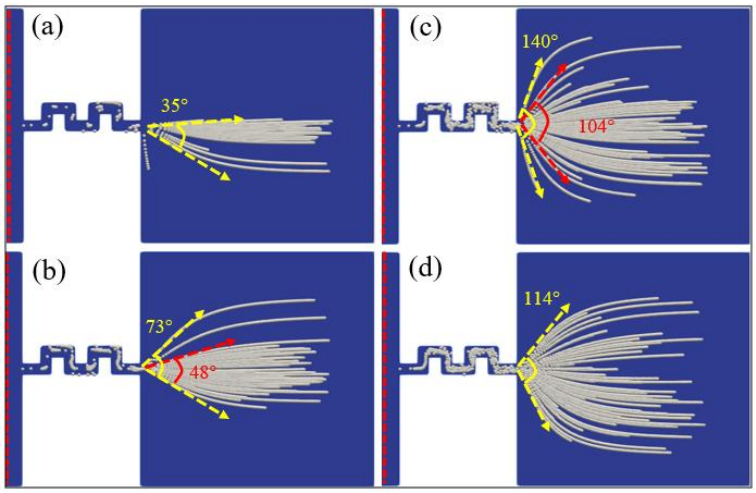

Figure 4.22 Particle paths of 100 ppm PAA solutions originating from (−100 μm, 0 μm) at: (a) $E_{app} = E_0$, (b) $E_A = 0.1E_0$, $f_E = 8$ Hz, (c) $E_A = 0.2E_0$, $f_E = 8$ Hz, (d) $E_A = 0.4E_0$, $f_E = 8$ Hz.

Figure 4.23 shows the particle path of 500 ppm PAA solutions originating from three different locations under DC electric field. The particle paths at three locations are all with relatively large opening angles (i.e., 76°, 67°, and 97°), and no strong relevance between opening angles and the locations of the source points is observed. Such result implies that for 500 ppm PAA solution,

elastic instabilities are widely triggered in the microchannel due to the stronger viscoelastic effect. Figure 4.24 presents the particle paths of 500 ppm PAA solution under AC electric fields with different amplitudes but the same frequency, same as in Figure 4.21. The particle paths are all with large opening angles: 72°, 87°, 92°, and 118°. Same as 100 ppm PAA solution, the opening angles increase with increasing amplitudes of the AC electric fields.

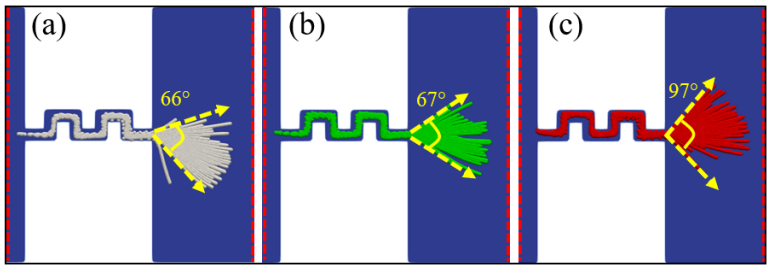

Figure 4.23 Particle paths of 500 ppm PAA solutions under DC electric field originating from: (a) (−100 μm, 0 μm), (b) (−100 μm, 4 μm), (c) (−100 μm, 8 μm).

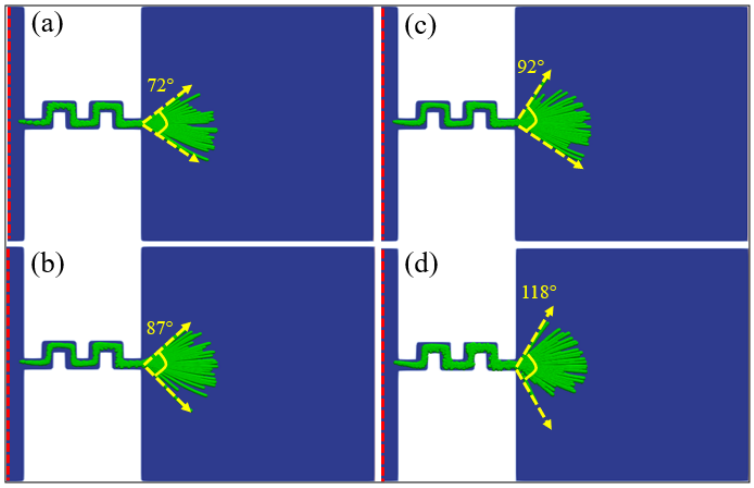

Figure 4.24 Particle paths of 500 ppm PAA solutions originating from (−100 μm, 4 μm) at: (a) $E_{app} = E_0$, (b) $E_A = 0.1E_0$, $f_E = 8$ Hz, (c) $E_A = 0.2E_0$, $f_E = 8$ Hz, (d) $E_A = 0.4E_0$, $f_E = 8$ Hz.

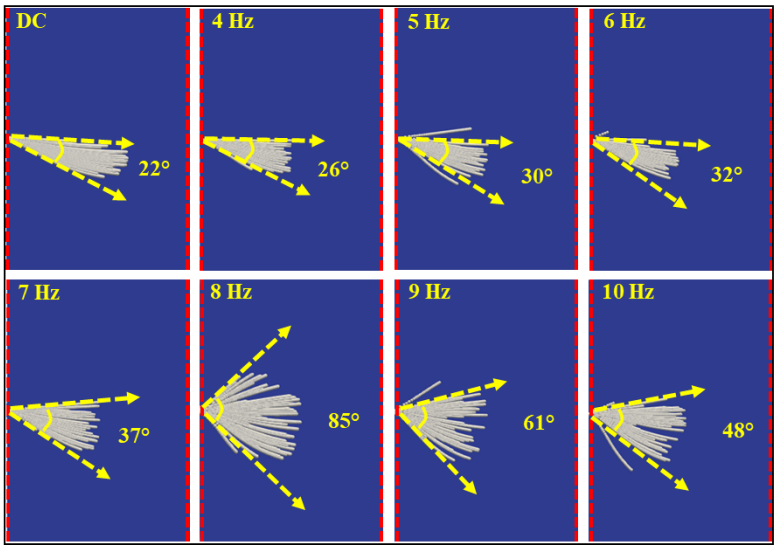

Figure 4.25 Particle paths of 250 ppm PAA solutions originating from (−100 μm, 0 μm) under DC electric field ($E_{app} = E_0$) and AC electric field at $E_A = 0.2E_0$, and f_E = 4, 5, 6, 7, 8, 9, and10 Hz.

Figure 4.25 presents the particle paths of 250 ppm PAA solution originating from (−100 μm, 0 μm) under DC electric field and AC electric field with the same amplitude ($E_A = 0.2E_0$) but different frequencies (4, 5, 6, 7, 8, 9, and10 Hz). The opening angles of the particle paths show differences under different frequencies. An opening angle of 22° is observed under DC electric field. Under AC electric field, when the frequency is relatively low, the opening angle slightly increases with the increase of frequency and the particle path shows the largest opening angle at 8 Hz. However, when the frequency is higher than 8 Hz, the opening angle of the particle path decreases as the increasing of frequency. Figure 4.26a shows the opening angles of particle paths originating from (−100 μm, 0 μm) of 100 ppm, 250 ppm, and 500 ppm PAA solutions under DC electric field and AC electric fields. For 100 ppm PAA solution, the opening angle of the particle path is relatively small under DC electric field, and the largest opening angle is observed at 5 Hz. When the frequency exceeds than 5 Hz, the particle paths remain a comparably large opening angle as 5 Hz. For 500 ppm PAA solution, under DC electric field, a much larger opening angle of the

particle path is observed compared with 100 ppm and 250 ppm PAA solutions. Under AC electric field, when the frequency is relatively low, larger opening angles of the particle paths are observed compared with DC electric field and the largest opening angle is observed at 5 Hz. However, when the frequency is relatively high, the opening angle decreases dramatically to a level smaller than DC electric field. Unlike Newtonian fluids, the existence of elasticity of viscoelastic fluid engenders its flow to have a characteristic frequency related to its elasticity. Such characteristic frequency can be identified by analyzing velocity fluctuations in DC driven EOF. Figure 4.26b shows the power spectra curves of velocity fluctuations under DC electric field at low frequencies. For 250 ppm PAA solution, the power spectra curve shows a peak at 9.2 Hz, while for 100 ppm and 500 ppm PAA solutions, the power spectra curves show peaks around a relatively lower frequency (i.e., 7 Hz) compared with 250 ppm PAA solution. The frequencies of the power spectra peaks in Figure 4.26b show a slight difference from the frequencies of opening angle peaks in Figure 4.26a. In order to induce the largest opening angle of the particle path originating from the centerline near the entrance of the microchannel, a frequency slightly lower than the characteristic frequency of the EOF obtained from DC driven flow is needed for the AC electric field. Moreover, when the frequency of the AC electric field is larger than the characteristic frequency, the opening angles of the particle path remain at the same level as the largest opening angle obtained. However, both 250 ppm and 500 ppm solutions show much smaller opening angles when the frequency exceeds the optimal frequency, and particularly the opening angles of 500 ppm PAA solution decrease to a level smaller than under DC electric field. Such result implies that for PAA solution with a low concentration (i.e., 100 ppm), stronger elastic instabilities are triggered in a pulsating EOF when the frequency exceeds the optimal value and such enhancing effect on the elastic instabilities remains observable for larger frequencies to a certain level. However, for PAA

solutions with a relatively high concentration (i.e., 250 ppm), an optimal frequency is needed to magnify the elastic instabilities to the highest level, and when the frequency exceeds the optimal value, such enhancing effect becomes insignificant. Furthermore, for PAA solutions with rather high concentration (i.e., 500 ppm), an optimal frequency is needed to fully magnify the elastic instabilities, while the elastic instabilities are restrained when the frequency to a certain degree is larger than the optimal value. The different effects of the AC electric field on the PAA solutions with different concentrations are probably due to the different relaxation time of the PAA solutions. PAA solution with higher concentration has a larger relaxation time, which means a longer time is needed for the EOF to react to the changes in the flow due to the changing electric field. Therefore, when the frequency of the AC electric field is too high, the polymers in the EOF do not have enough time to fully react and thus the enhancing effect on the elastic instabilities is insignificant. However, geometry is also a factor that is possibly related to the optimal frequency, such as the contraction ratio, length of the microchannel, and shape of the microchannel.

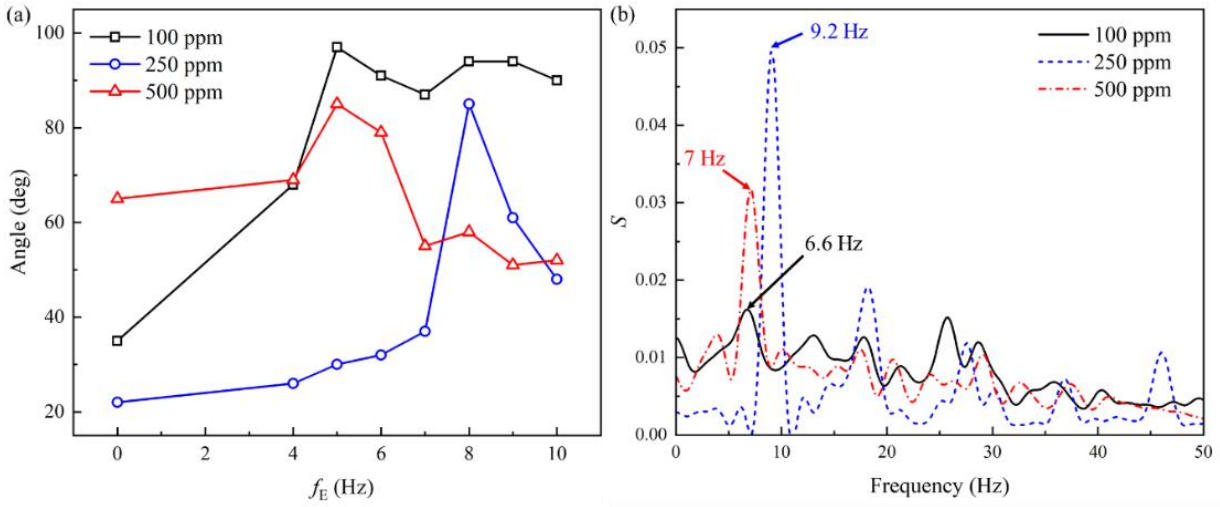

Figure 4.26 Statistical results of 100 ppm, 250 ppm and 500 ppm PAA solutions: (a) opening angle of particle paths originating from (−100 μm, 0 μm), (b) power spectra of velocity fluctuations under DC electric field.

4.5 Conclusions

Electroosmotic flow (EOF) of viscoelastic fluid through a 20:1:20 constriction microchannel with 90° bends under DC/AC electric fields is studied. Three different concentrations of the polymer solution under AC electric fields with various amplitudes and frequencies show the following distinct results:

(1) Under DC electric field, the velocity of Newtonian fluid is steady and time independent, however, the velocities of PAA solution show fluctuations. The power spectra of the velocity fluctuations under both DC and AC electric fields show power-law decay over a wide range of frequencies, which is a typical characteristic of elastic turbulence.

(2) Under AC electric field, the velocity of PAA solution fluctuates in the same frequency as the electric field. Apart from the main fluctuation, a minor fluctuation can also be observed. The frequency and amplitude of the electric field show no significant influence on the

average of the velocity at the center of the microchannel. However, when the amplitude of the electric field is fixed, the amplitude of the velocity increases with the increase of the frequency.

(3) A pair of upstream vortices are observed for PAA solutions. The sizes of the vortices are much larger for the highly concentrated PAA solution, and the vortices are significantly altered by the AC electric field.

(4) The dye pattern of the PAA solution fluctuates in the microchannel. Under AC electric field, a distinct wavy dye pattern is observed in the outlet reservoir. The dye pattern in the microchannel is affected by the 90° bends. At the downstream of the 90° bends the dye concentration is more evenly distributed than upstream the 90° bends.

(5) The particle path from the same location at the entrance of the microchannel shows a jet-like shape in the outlet reservoir with an opening angle. The opening angle of the particle path is highly related to the polymer concentration and the AC electric field. An optimal frequency is needed to get the largest opening angle for all PAA solutions. However, frequencies higher than the optimal value still show enhancing effects for the low-concentrated PAA solution, while a higher frequency for high-concentrated PAA solution tends to restrain the elastic instabilities.

CHAPTER 5

FREQUENCY STUDY OF TIME-PERIODIC ELECTROOSMOTIC FLOW OF VISCOELASTIC FLUID THROUGH SHORT CONSTRICTION MICROCHANNEL

5.1 Introduction

In actuality, a DC electric field is employed in EOF to drive the fluid in microchannels. However, due to the bubble formation issue in electrolyte near electrodes that the DC electric field experiences recently, periodic EOF is gaining more and more attention as a substitute way for microfluidic control and transport in the microchannels. It has been discovered that some natural chemical processes, such as the electroosmosis of the human epidermal membrane [196] are associated to periodic EOF. Periodic electroosmosis, in contrast to steady electroosmosis, has a velocity profile that wavers with time and has been used to improve fluid mixing and flow rate control in microchannels [197, 198]. Dutta and Beskok [199] were among the early researchers investigating the time-periodic EOF between two parallel plates. Their analytical solution of velocity revealed near-wall inflection points with localized velocity extrema, which may have an impact on the stability properties of time-periodic EOF. Ramos et al.'s theoretical investigation [200] has demonstrated that EOF is frequency-dependent, with the velocity being a function of both space and frequency across micro-electrodes. Experimental research of Minor et al. [201] on the electromobility of colloidal particles revealed that the bulk electroosmosis could be stopped by applying an AC electric field with a specific frequency. Microfluidic pumps based on AC EOF have been the subject of research studies since the discovery of the AC EOF conveyance mechanism. Studer et al. [202] fabricated microfluidic AC EOF pump and the velocity was found to be dependent on the frequency of the electric field. Within a wide range of frequencies from 0.1 kHz to 100 kHz, the maximum velocity of the pump was seen at 5 kHz. According to Olesen et

al.'s experimental investigation [203, 204], AC electrokinetic micropumps are more effective at pumping microflows when the voltage is low.

Newtonian fluids were the primary focus of all the pulsating EOF research work mentioned above. With only a small body of literature, the impact of periodic EOFs on non-Newtonian fluids is not well understood. The analytical solutions for time-periodic EOF of general Maxwell fluids between micro-parallel plates were initially examined by Liu et al. [205] utilizing the separation of variables approach, where the velocity profile and volume flow rate showed a strong dependence on the flow parameters. The analytical solution for the analogous flow in the rectangular microchannel was researched by Jian et al. [206]. Recent research by Moghadam and Akbarzadeh [207] into the time-periodic EOF of power-law fluid in a circular microchannel revealed that the flow was constrained to a thin region near the channel wall at extremely high dimensionless frequencies. Later, a study based on the Carreau-Yasuda model, which combines pressure gradient and time-periodic electroosmosis, was also carried out by the same author [208]. The improved mixing effect of AC EOF in a T-junction micromixer was examined using a power-law model in Alipanahrostami and Ramiar's numerical work [209]. Based on the PTT model, Sayantan and Sandip [210] employed time-periodic EOF to regulate the mass flow rate of viscoelastic fluids. It was discovered that the mass flow rate amplitude and the phase lag were connected to the fluid's viscoelastic properties.

The mechanism of time-periodic EOF of viscoelastic fluids is still unknown due to the relatively few investigations that have been undertaken. Therefore, the time-periodic EOF of viscoelastic fluids is investigated in the current study using 10:1:10 contraction microchannels. The viscoelastic properties of the PAA water solution are simulated using the OB model, and the electrokinetic phenomenon is described using the Poisson-Boltzmann (PB) model. The

microchannel is subjected to both a continuous DC electric field and AC electric fields with different frequencies. The effects of the AC electric field frequency on the viscoelastic time-periodic EOF are investigated.

5.2 Geometry and parameters

Short microchannels with three different lengths (L_C = 10 μm, 15 μm, and 20 μm) connecting two reservoirs on either side are investigated as shown in Figure 5.1. The height of the channel is H_C = 40 μm. The height and the length of the reservoirs are H_r = 400 μm and L_r = 400 μm, respectively. A DC and AC electric potential bias $U = U_0 + U_A\sin(2f_E\pi t)$ is applied between the inlet (Anode) and outlet (Cathode). The apparent electric field between the inlet and outlet is defined as $E_{app} = U/(2L_r + L_C)$. In this study, U_0 = 40 V, U_A = 16 V, and f_E is investigated from 0 Hz to 20 Hz. The governing equations are the same as in chapter 3. The bulk ion concentration $c_0 = 0.0001$ mM, and the EDL thickness is 954 nm. The EOF of 500 ppm PAA water solution is investigated. The polymer viscosity is η_p = 0.0111 kg/(m·s) and the relaxation time is λ = 0.0476 s. The boundary conditions are given as follows (shown in Figure D.2 in Appendix D):

(1) At the Anode (edge AL in Figure 5.1): $\mathbf{n}\cdot\nabla\mathbf{u} = 0$; $p = 0$; $\boldsymbol{\tau} = \mathbf{0}$; $\phi_{Ext} = U_0 + U_A\sin(2f_E\pi t)$; $\mathbf{n}\cdot\nabla\psi = 0$; $\boldsymbol{\Theta} = \mathbf{0}$; where **n** denotes the normal unit vector on the surface.

(2) At the Cathode (edge FG in Figure 5.1): $\mathbf{n}\cdot\nabla\mathbf{u} = 0$; $p = 0$; $\mathbf{n}\cdot\nabla\boldsymbol{\tau} = 0$; $\phi_{Ext} = 0$; $\mathbf{n}\cdot\nabla\psi = 0$; $\mathbf{n}\cdot\nabla\boldsymbol{\Theta} = 0$.

(3) On the reservoir walls (edges ABC, DEF, GHI, and JKL in Figure 5.1) and the microchannel walls (Edges CD and IJ in Figure 5.1): $\mathbf{u} = \mathbf{0}$; $\mathbf{n}\cdot\nabla\phi_{Ext} = 0$; $\psi = \xi_0$; $\mathbf{n}\cdot\nabla\boldsymbol{\Theta} = 0$; $\mathbf{n}\cdot\nabla p$ is obtained from the momentum equation; the components of $\boldsymbol{\tau}$ are linearly extrapolated.

The following initial conditions are specified within the domain: $\mathbf{u} = \mathbf{0}$; $p = 0$; $\boldsymbol{\tau} = \mathbf{0}$; $\phi_{Ext} = 0$; $\psi = 0$; $\boldsymbol{\Theta} = \mathbf{0}$.

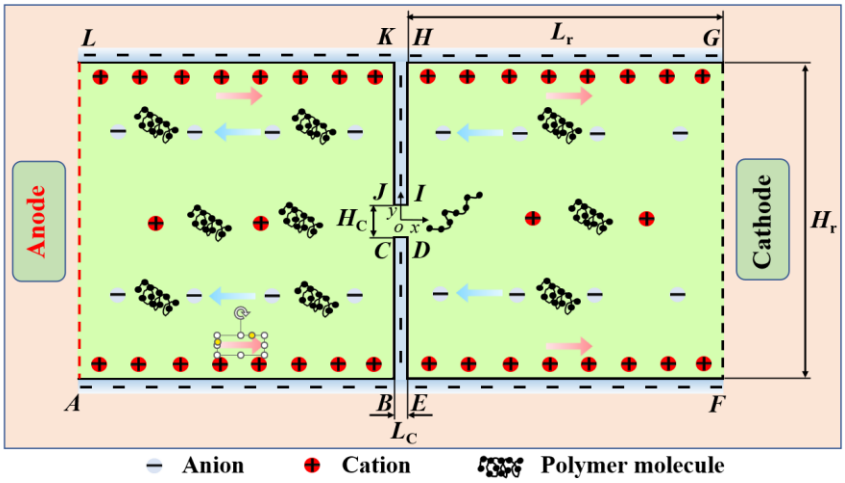

Figure 5.1 Schematic diagram of a constriction microchannel connecting two reservoirs at both ends.

The structural mesh used to discretize the 2D computational domain is shown in Figure 5.2. The geometry at 90° corners is slightly rounded to avoid the electric field singularity. The edge size of the layer of cells adjacent to the walls is 25 nm and there are 15 cells in the EDL. The mesh for 10 μm microchannel has a total of 526560 cells as shown in Figure 5.2, and there are 530780 and 535000 cells for the 15 μm microchannel and 20 μm microchannel, respectively.

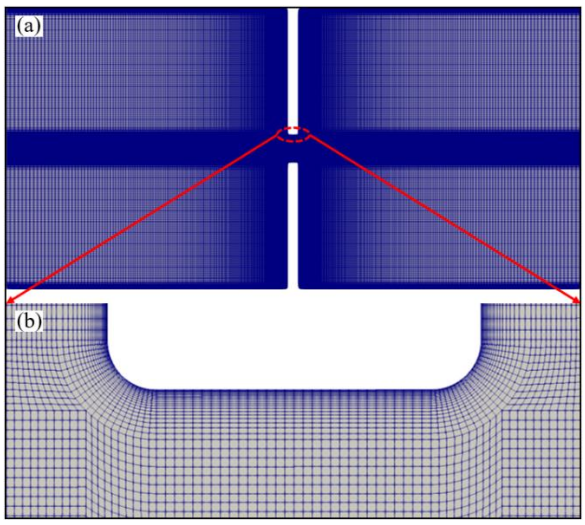

Figure 5.2 Computational mesh used in the numerical simulations for microchannels with length of 15 um. Mesh of the whole geometry (a) and detailed view of the mesh at channel (b).

5.3 Mesh independence study

Three different meshes are used to perform a mesh independence study for each microchannel for the 500 ppm PAA solution as shown in Figure 5.3. For mesh 1, the meshes near the charged walls are 25 nm, and there are 15 cells within the EDL thickness. In mesh 2, there are 20 cells within the EDL thickness and the size of the cells near the charged walls is 20 nm. The cells outside the EDL thickness are the same for mesh 1 and mesh 2. In mesh 3, the cells within the EDL thickness are the same as mesh 1. However, the cells outside the EDL thickness are slightly finer than mesh 1. The number of cells in each mesh for the three microchannels is listed in Table 5.1.

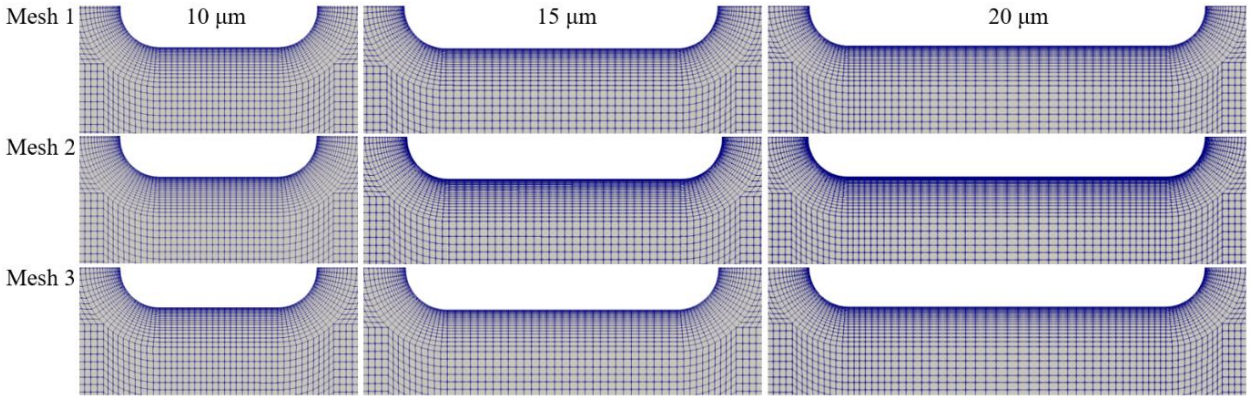

Figure 5.3 Detailed views near the charged wall of the three different meshes for the three microchannels used for the mesh independence study.

Table 5.1 Number of cells in each mesh used for mesh independence study.

Number of cells	10 μm	15 μm	20 μm
Mesh 1	526560	530780	535000
Mesh 2	547580	552100	556620
Mesh 3	632400	636620	640840

Figure 5.4 plots the cross-sectional average velocities at $x = 0$ in the microchannel of the three different meshes from $t = 0$ s to $t = 1$ s, which is calculated by $U_{\text{ave}} = \int_{-H_C/2}^{H_C/2} U(0, y)dy / H_C$. Within

1 s, the cross-sectional average velocities show no significant difference for the three different meshes considering the large fluctuations in the viscoelastic EOF. The time averaged cross-sectional average velocities are plotted in Figure 5.4d. For the 3 meshes of the microchannels with different lengths, the time averaged cross-sectional average velocities are very close. Relative errors of mesh 2 and mesh 3 are calculated compared with mesh 1 as shown in Table 5.2. The relative errors are all smaller than 5%.

The three different meshes show great consistency in predicting the velocity field in the microchannel. In order to save the computational cost, mesh 1 is used to perform other simulations.

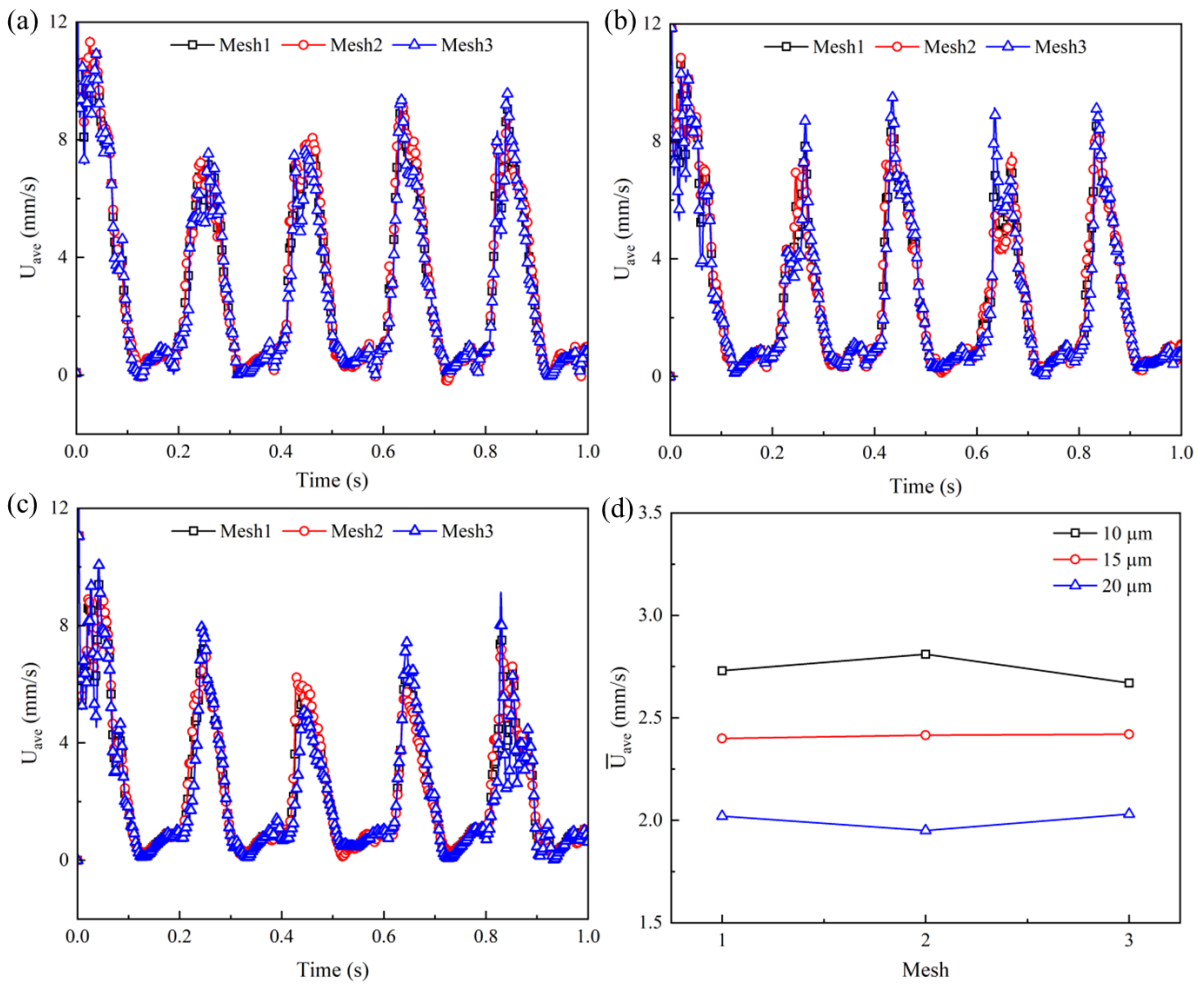

Figure 5.4 Cross-sectional average velocities at $x = 0$ in the microchannel: (a) velocities in the 10 μm microchannel, (b) velocities in the 15 μm microchannel, (c) velocities in the 10 μm microchannel, (d) time averaged cross-sectional average velocities.

Table 5.2 Relative errors of cross-sectional average velocity of mesh 2 and mesh 3.

Relative error	10 μm	15 μm	20 μm
Mesh 2	2.93%	0.63%	3.47%
Mesh 3	1.47%	0.83%	0.49%

5.4 Results and discussion

In this section, flow features of viscoelastic EOF through short constriction microchannels are obtained when imposed to constant and pulsating electric fields. Three different lengths (i.e., 10 μm, 15 μm and 20 μm) of the microchannel are studied. Newtonian fluid is investigated for the 10 μm microchannel to provide reference flow characteristics. The frequency of the pulsating electric field is investigated from 1 Hz to 20 Hz. The instabilities of the viscoelastic EOF are described. The energy spectra of the viscoelastic EOF under a constant electric field shows a main frequency. Finally, the influence of the frequency of the pulsating electric field on the viscoelastic EOF is analyzed.

5.4.1 Instability of the EOF under constant electric field

The results of Newtonian fluid with the same total viscosity as 500 ppm PAA solution are first presented as a reference for the viscoelastic fluid. Under DC electric field, the EOF reaches a steady state for Newtonian fluids. As shown in Figure 5.5, the streamlines of Newtonian fluid show excellent symmetry about the *x*-axis and *y*-axis. Figure 5.6a shows the velocities at the center of the microchannel (i.e., (0,0)) for Newtonian fluid under DC electric field and AC electric fields (f_E = 4 Hz and 10 Hz). Under DC electric field, the velocity is time independent, and no fluctuation is observed. Under AC electric field, the velocity fluctuates in the same frequency as the electrical driving force. No minor fluctuation is observed in the velocity other than the fluctuation in the main frequency. Under different frequencies, the amplitude of the velocity fluctuation and the cross-sectional time-averaged velocity show no significant difference. However, for PAA solution, the velocity at the center of the microchannel fluctuates dramatically even under DC electric field as shown in Figure 5.6b.

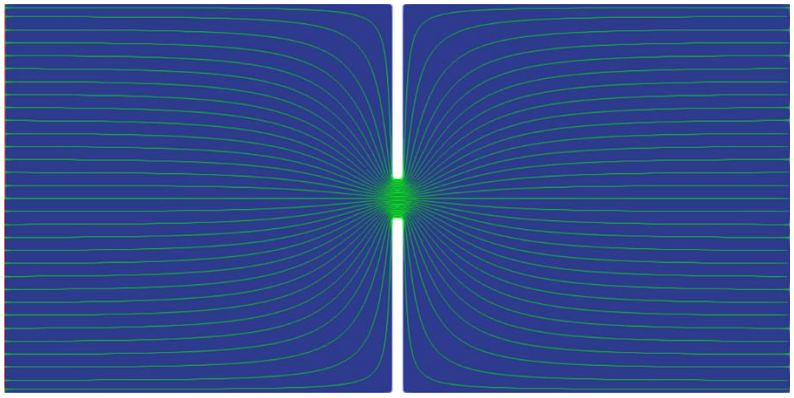

Figure 5.5 Time-independent streamlines of Newtonian fluid under DC electric field for 10 μm microchannel.

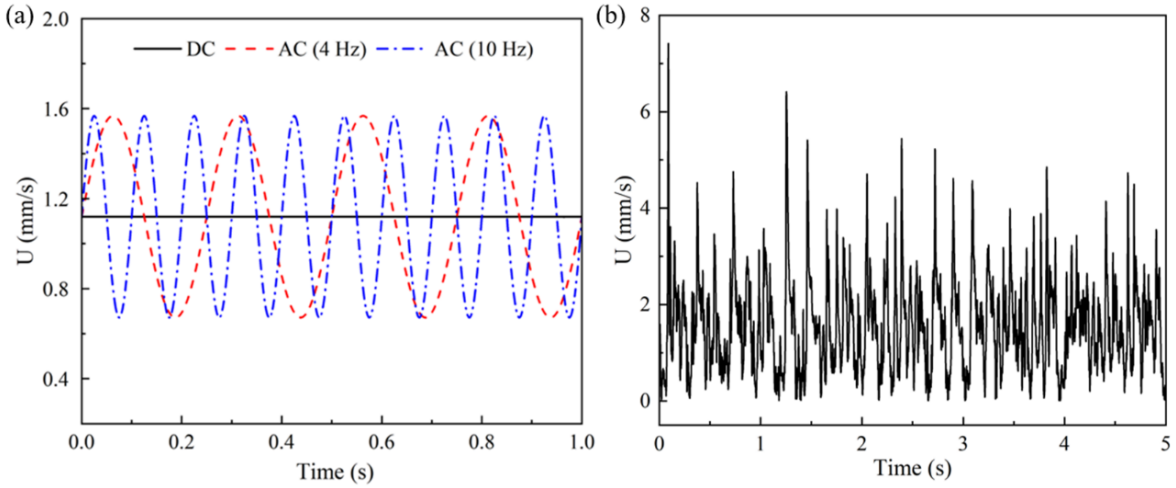

Figure 5.6 Velocity at the center of 10 μm microchannel (i.e., (0,0)): (a) Newtonian fluid under DC electric field and AC electric field (f_E = 4 Hz and 10 Hz), (b) 500 ppm PAA solution under DC electric field.

Figure 5.7 displays the streamlines of the PAA solution at different times when subjected to DC electric field. Different from the static flow state of the Newtonian EOF, the viscoelastic EOF is time dependent. Strong fluctuation of the velocity field is observed in the left inlet reservoir near the entrance of the constriction microchannel. A pair of unstable vortices are observed to fluctuate

in both size and location. As shown in Figure 5.7, from 1 s to 1.08 s, the size of the vortices gradually decreases until the vortices disappear at 1.08 s, after which the vortices form again and grow in size. At 1 s, the pair of vortices is oriented to the direction above the centerline of the microchannel. However, at 1.04 s, an opposite orientation of the pair of vortices is observed. Due to the existence of the stagnation area and the fluctuation of vortices orientation, the flow along the centerline in the right outlet reservoir is affected and fluctuates. Unlike Newtonian fluids, the existence of elasticity is a unique feature of viscoelastic fluids, which results in the existence of a characteristic frequency (f_C) in the viscoelastic flow. In order to have a deeper understanding of the instabilities observed in the viscoelastic EOF under DC electric field, the power spectra of the velocity fluctuation are obtained by conducting Fast Fourier transformation. Figure 5.8 shows the kinetic energy spectra of the velocity fluctuations at the center of the microchannel (i.e., (0,0)) in the frequency domain. For the microchannel with 3 different lengths, the energy spectra curves exhibit similar characteristics. The majority energy of the velocity fluctuation is distributed in the range 0-20 Hz. Under DC electric field, a clear dominant frequency between 5 Hz and 7 Hz is observed in the energy spectra of the velocity fluctuations, which indicates the characteristic frequency of the viscoelastic flow.

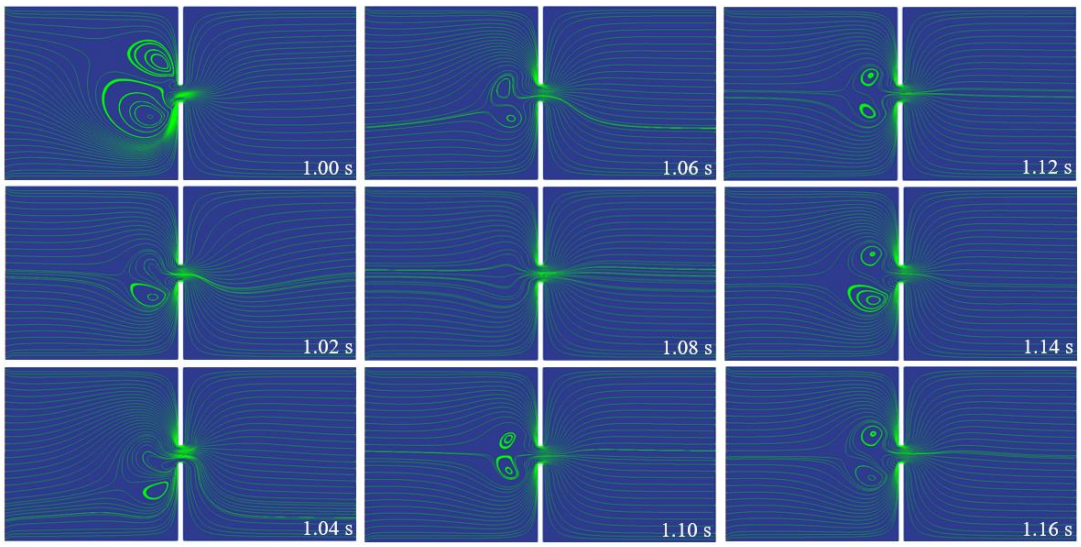

Figure 5.7 Streamlines of 500 ppm PAA solution in 10 μm microchannel under DC electric field.

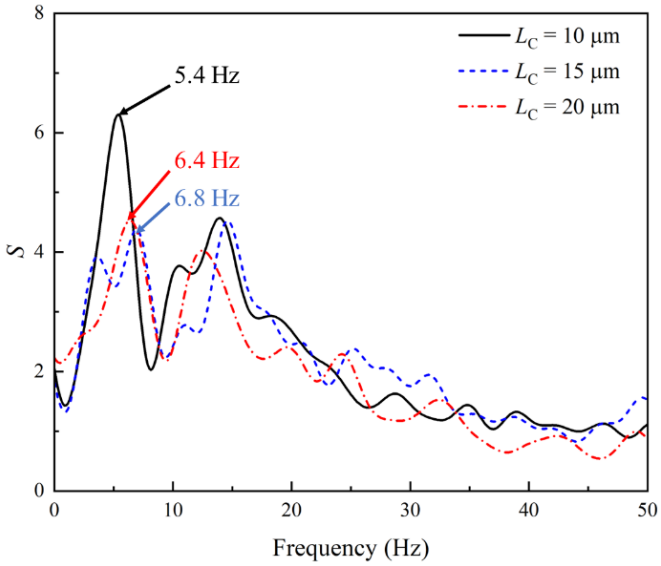

Figure 5.8 Energy spectra of the velocity fluctuation in the viscoelastic EOF at the center of the microchannel (i.e., (0,0)) when under DC electric field.

5.4.2 Effects of the frequency on the instabilities of the viscoelastic EOF

To investigate the effects of the characteristic frequency on the viscoelastic EOF, pulsating electric field is applied to the microchannel. The energy spectra of the velocity fluctuation under

DC electric field show that the majority energy of the fluctuation is distributed under 20 Hz in the frequency domain, and the characteristic frequency of the viscoelastic EOF is between 5 Hz and 7 Hz. Therefore, the frequency of the externally applied electric field is studied from 1 Hz to 20 Hz. The velocity at the center of the microchannel (i.e., (0,0)) is used for the frequency analysis. As shown in Figure 4a, in the Newtonian pulsating EOF, the amplitude of the velocity keeps constant for different pulsating frequencies. However, in the viscoelastic pulsating EOF, the amplitude of the velocity and the cross-sectional time-averaged velocity show a significant difference when under AC electric field with different frequencies.

Figure 5.9 shows the velocity and the energy spectra of the velocity fluctuation of the viscoelastic EOF at the center of the microchannel under pulsating electric field with different frequencies (i.e., 5 Hz, 10 Hz, 15 Hz, and 20 Hz), among which significant difference can be observed. As shown in Figure 5.9a, when the frequency of the pulsating electric field is 5 Hz, which is close to the characteristic frequency of the viscoelastic fluid, a clear periodic velocity profile in the same frequency as the electrical driving force is obtained with relatively large and uniform velocity amplitudes. However, when the frequency of the electric field is much larger than the characteristic frequency of the viscoelastic fluid, the fluctuation of the velocity is more random. For example, when the frequency is 10 Hz, the amplitude of each peak in the velocity-time profile varies dramatically. Within the first 2 seconds, 7 relatively large peaks are observed, while other peaks are extremely small. For the velocities under 15 Hz and 20 Hz electric field, the amplitudes of the velocity fluctuation are more uniform than under 10 Hz electric field, however, the amplitudes are still generally much smaller than under 5 Hz electric field. To have a deeper insight in the frequency distribution of the velocity fluctuation, Figure 5.9b shows the energy spectra of the velocity fluctuations at the center of the microchannel. For the viscoelastic EOF under

pulsating electric field with different frequencies, the power spectra curves share the same general appearance: there is a plateau at low frequencies followed by a power-law decay region at higher frequencies, which is a unique feature of elastic turbulence. The exponent is around 2.4 for all the energy spectra curves. In the power spectra of the velocity fluctuation under 5 Hz pulsation electric field, a clear peak is observed at 5 Hz. However, for the energy spectra curves under pulsating electric field with higher frequencies, although the highest energy appears at the frequencies of the electric driving force, no significant peaks are observed in the rest energy spectra curves in Figure 5.9b compared with under 5 Hz electric field.

Figure 5.10 shows the streamlines of the viscoelastic fluid in 10 μm microchannel under 5 Hz pulsating electric field. Compared with the streamlines under DC electric field as shown in Figure 5.7, more chaotic streamlines are observed under pulsating electric field. At t = 1 s, a pair of large vortices are observed in the left inlet reservoir before the entrance of the constriction microchannel, resulting in a stagnation area along the centerline of the microchannel. Then due to the changing electric field, the pair of vortices disappear and at t = 1.08 s the vortices form again. However, at t = 1.10 s, the pair of vortices move away from the centerline of the microchannel to the corner of the left inlet reservoir forming a stagnation in the flow near the upstream lips of the constriction microchannel and the fluid at the centerline of the inlet reservoir flows through the constriction microchannel. Moreover, in the right outlet reservoir, two small vortices form near the downstream lips of the constriction microchannel. The upstream lip vortices are unstable and move to the centerline of the microchannel with the change of the pulsating electric field as shown in the streamlines at t = 1.12 s and t = 1.14 s, resulting in the fluid near the charged walls of the inlet reservoir flows through the constriction microchannel. At t = 1.16 s, the streamlines are even more chaotic, in which two small unsymmetric vortices form before the entrance of the constriction

microchannel and lead to the fluid flowing through only the lower half of the microchannel. And in the outlet reservoir the fluid flows near the charged walls forming a large circulation near the centerline of the reservoir. The upstream lip vortices and the downstream vortices observed under pulsating electric field are unique and not observed under DC electric field. Figure 5.11 shows the first normal stress difference N1($\tau_{xx} - \tau_{yy}$) of 500 ppm PAA solution in 10 μm microchannel under 5 Hz pulsating electric field at different times. A significant positive increase of N1 is induced, which indicates that the polymer molecules are strongly stretched in the *x*-axis direction, whereas in the *y*-axis direction, the polymer molecules are relatively compressed. The increase of N1 is due to the high velocity gradient at the entrance of the microchannel. Due to the relaxation time of the polymer molecules, the stretched polymer molecules take time to relax. Therefore, the positive N1 is observed at the downstream of the constriction microchannel.

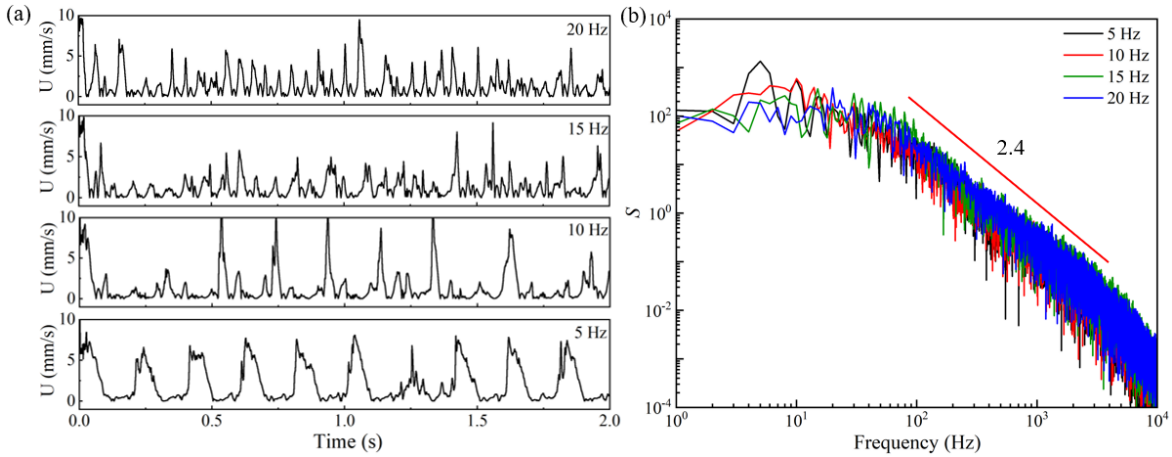

Figure 5.9 Velocity at the center of the 10 μm microchannel under pulsating electric field with different frequencies (i.e., f_E = 5, 10, 15, and 20 Hz): (a) velocity-time profile, (b) energy spectra of the velocity fluctuations.

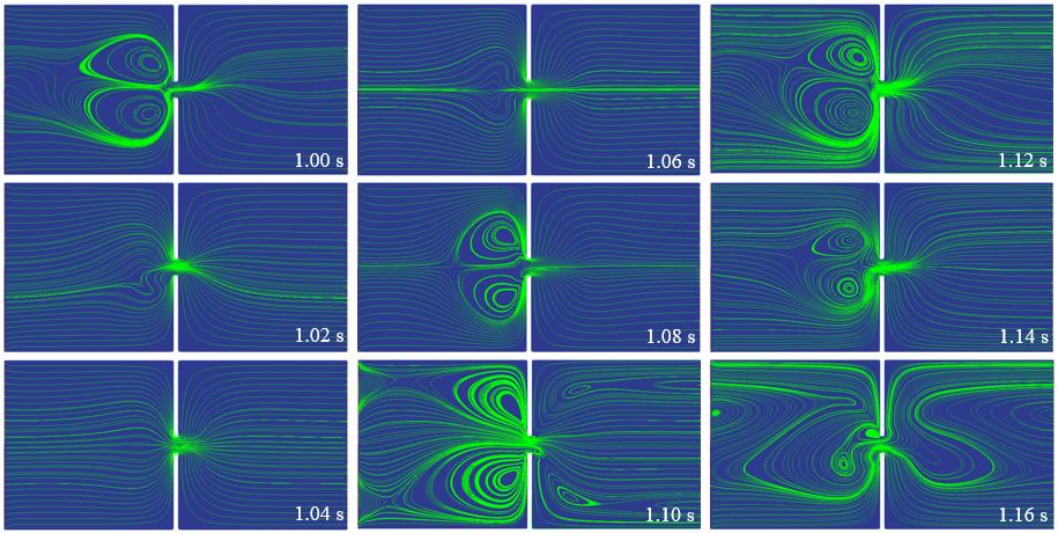

Figure 5.10 Streamlines of 500 ppm PAA solution in 10 μm microchannel under 5 Hz pulsating electric field.

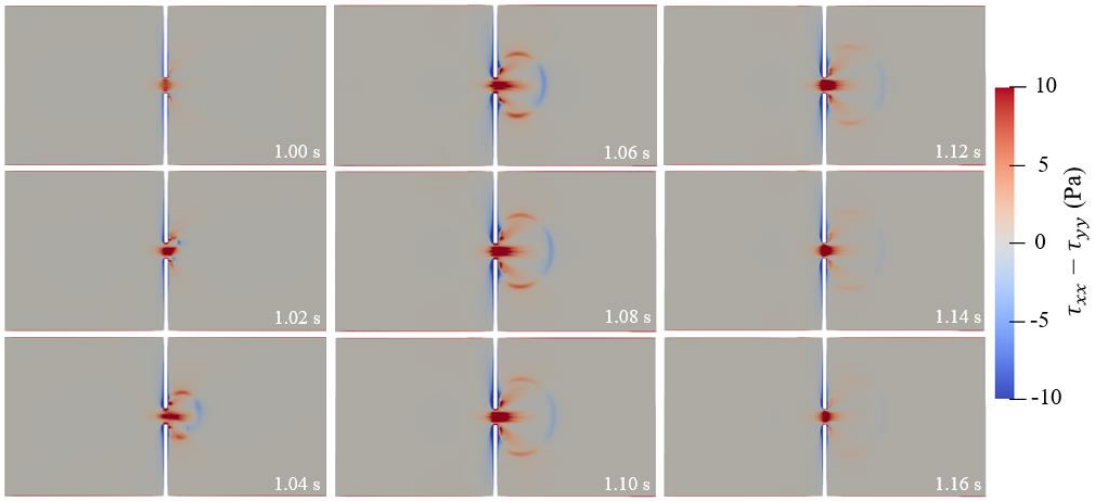

Figure 5.11 First normal stress difference of 500 ppm PAA solution in 10 μm microchannel under 5 Hz pulsating electric field.

Figure 5.12 shows the statistical results of the viscoelastic EOF under pulsating electric field with frequencies from 1 Hz to 20 Hz. Figure 5.12a plots the magnitude of the energy spectra at the dominant frequency, which is the frequency of the pulsating electric field. For the 10 μm

microchannel, the highest energy magnitude appears at f_E = 5 Hz, while for the 15 μm and 20 μm microchannels, the highest energy magnitude appears at f_E = 6 Hz. Such result show consistency with the energy spectra curves in Figure 5.8, which shows the characteristic frequency of the viscoelastic fluid under DC electric field. When the pulsating electric field is at the same frequency as the characteristic frequency of the viscoelastic fluid, the magnitude of the energy spectra at the dominant frequency is much higher than when the pulsating electric field is at frequencies far from the characteristic frequency of the viscoelastic fluid, which indicates that the energy of the velocity fluctuation is highly distributed near the characteristic frequency and resonance takes place. Figure 5.12b shows the cross-sectional average velocities of the three microchannels. Since the flow velocity is time-dependent, the cross-average velocity over a period of $\Delta t = t_2 - t_1$ is calculated. The time-averaged velocity is calculated as:

$$\bar{U} = \frac{\int_{t_1}^{t_2} \int_{-H_C/2}^{H_C/2} U(0, y)\, dy dt}{\Delta t \cdot H_C}, \tag{5.1}$$

where Δt = 2 s is adopted in the current study. Intriguing characteristics of the statistical outcome of the average velocities can be seen in the following aspects: (1) the length of the microchannel shows significant influence on the pulsating viscoelastic EOF; the average velocity is generally higher in shorter microchannels; (2) the average velocity in the microchannel is highly dependent on the frequency of the pulsating electric field, the average velocity increases dramatically under pulsating electric field with increasing f_E until f_E reaches a certain value close to the characteristic frequency of the viscoelastic fluid, however, with the further increasing of f_E, the average velocity decreases dramatically until f_E = 9 Hz; when f_E is relatively high (> 9 Hz), the average velocity decreases to a level smaller than the average velocity under DC electric field; (3) the highest average velocity is obtained when f_E = 4 Hz for 10 μm and 15 μm microchannels, and the highest

average velocity in the 20 μm microchannel is observed at f_E = 5 Hz, which are slightly smaller than the frequencies observed for the highest energy amplitude in Figure 5.12a.

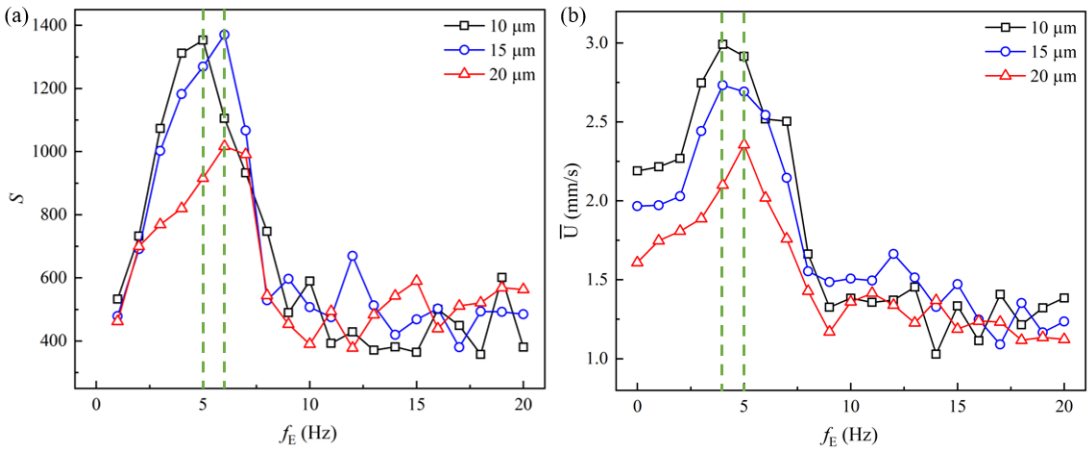

Figure 5.12 Statistical results of the viscoelastic EOF: (a) magnitude of the energy spectra at the frequency of the pulsating electric field, (b) cross-sectional average velocity.

5.5 Conclusions

Electroosmotic flow (EOF) of viscoelastic fluid through short 10:1:10 constriction microchannels is numerically investigated as a function of the frequency of the pulsating electric field. Three lengths of the constriction microchannel are studied. The frequency of the pulsating electric field is varied from 1 Hz to 20 Hz. The EOF of Newtonian fluid under pulsating electric field is studied for reference. Compared with Newtonian EOF and viscoelastic EOF under DC electric field, the pulsating viscoelastic EOF shows the following distinct results:

(1) Under DC electric field, the Newtonian EOF is time independent. Under pulsating electric field with the same amplitude, the amplitude of the velocity and the average velocity in Newtonian EOF is independent on the frequency of the pulsating electric field. However,

the viscoelastic EOF shows significant fluctuations under DC electric field and strong dependence on the frequency of the pulsating electric field.

(2) For the viscoelastic EOF under DC electric field, the dynamic energy spectra of the velocity fluctuation at the center of the microchannel viscoelastic EOF shows a dominant frequency, which indicates the existence of the characteristic frequency of the viscoelastic fluid.

(3) Under pulsating electric fields with various frequencies, strong instabilities are triggered in the viscoelastic EOF with random upstream and downstream vortices observed. The energy spectra curves of the velocity fluctuations share similar general features with a peak at the dominant frequency and a power-law decay over a wide range of frequencies, which is a typical characteristic of elastic turbulence.

(4) The highest magnitude of the energy spectra is observed at the frequency of the pulsating electric field. However, the highest magnitude varies with the exciting frequency and resonance occurs in the EOF when the frequency of the pulsating electric field is near the characteristic frequency of the viscoelastic fluid observed under DC electric field.

(5) The average velocity in the microchannel is highly dependent on the frequency of the pulsating electric field. When the frequency is relatively low, the average velocity increases with the increasing frequency and the highest average velocity is observed near the characteristic frequency of the viscoelastic fluid. However, at relatively high frequencies, the average velocity decreases to a level even smaller than under DC electric field.

CHAPTER 6

CONCLUSIONS AND FUTURE WORK

6.1 Conclusions

Microfluidics has been widely used in many applications, especially in bioengineering, where electroosmotic flow plays an important role due to the unique advantages over pressure-driven flow. Many biofluids used in bioresearch show strong viscoelastic effects due to the existence of large molecular chains. Therefore, understanding the mechanism of viscoelastic EOF in microchannels is of practical importance. Numerical simulation provides a powerful tool for investigating the intriguing flow phenomenon in viscoelastic EOF, such as the electro-elastic turbulence, and has been widely utilized.

In this dissertation, the EOF of viscoelastic fluid in contraction microchannels is intensively investigated using a viscoelastic solver based on OpenFOAM. First, the viscoelastic EOF in a 10:1:10 contraction/expansion microchannel is investigated for a wide range of applied electric fields and polymer concentrations. The elastic instabilities are found to be highly dependent on both the electric field and the polymer concentration. The elastic instabilities in the viscoelastic EOF can be observed from the velocity fluctuation and the formation of upstream vortices. The upstream vortices are related to the level of the induced elastic stress within the contraction microchannel near the entrance. And the flow conditions that will trigger the upstream vortices are shown in a polymer concentration and electric field domain flow map.

Next, the viscoelastic EOF in the microchannel with 90° bends under DC and AC electric fields is investigated. The energy spectra of the velocity fluctuations at the center of the microchannel show power-law decay over a wide range of frequencies, which indicates the existence of elastic turbulence. Such characteristic is observed both under DC electric field only and the combination

of DC and AC electric field. A characteristic frequency in the energy spectra is observed at relatively low frequencies under DC electric field. The 90° bends show influence on the dye concentration profile across the microchannel cross-section. The dye concentration is more evenly distributed with increasing numbers of 90° bends and increasing polymer concentration. The opening angle of the particle path at the outlet of the microchannel show dependency on the frequency of the AC electric field. The largest opening angle is observed at a frequency slightly lower than the characteristic frequency.

Finally, a frequency study of the viscoelastic EOF is performed in short constriction microchannels. Majority of the energy is distributed at the frequencies smaller than 20 Hz in the energy spectra of the velocity fluctuation under DC electric field, and the peak in the energy spectra indicates that the characteristic frequency of the viscoelastic EOF is around 6 Hz. Under AC electric field, the amplitude of the energy spectra and the average velocity show strong dependency on the frequency of the AC electric field. The highest amplitude of the energy spectra and average velocity are obtained when the frequency is around 5 Hz, which is very close to the characteristic frequency. However, when the frequency is higher than 10 Hz, the fluctuation is suppressed and the average velocity decreases to a level smaller than under DC electric field.

6.2 Future work

In this dissertation, the numerical investigations of the viscoelastic EOF in microchannels consider relatively simple conditions and reveal some intriguing flow phenomena. In the future, the study can be further extended in the following aspects to obtain a better understanding of the elastic instabilities in viscoelastic EOF.

(1) To save computational resources, only 2D geometry is considered in the current study. However, a 3D geometry introduces more complexity to the viscoelastic EOF. Therefore,

the simulation of viscoelastic EOF in 3D microchannels is of great importance in understanding the conditions that will induce elastic instabilities. By comparing the results of 2D simulation and 3D simulation, the necessary geometries of the microchannel for triggering elastic instabilities can be better understood and therefore experimental study of viscoelastic EOF in microchannel can be guided.

(2) In the current study, a constant wall zeta potential is used for the microchannel and reservoirs. The EOF velocity is highly related to the wall zeta potential. Therefore, a constant wall zeta potential predicts relatively simple flow conditions. Viscoelastic EOF in microchannels with varying wall zeta potentials can be investigated in triggering the elastic instabilities, which can be applied to the mixing of fluids in microchannels with rather straightforward geometries.

(3) Only OB model is used in the current study to describe the elastic effect of the polymer. Different viscoelastic constitutive models take into account different properties of the polymers, which can show a significant influence on the behavior of the viscoelastic EOF. Therefore, more constitutive models can be investigated by numerical simulations of the EOF in microchannels. Comparing the results of different constitutive models can reveal the effects of the polymeric microstructure on the elastic instabilities.

REFERENCES

1. Whitesides, G.M., *The origins and the future of microfluidics.* nature, 2006. **442**(7101): p. 368-373.
2. Beebe, D.J., G.A. Mensing, and G.M. Walker, *Physics and applications of microfluidics in biology.* Annual review of biomedical engineering, 2002. **4**(1): p. 261-286.
3. Nguyen, N.-T., S.T. Wereley, and S.A.M. Shaegh, *Fundamentals and applications of microfluidics*. 2019: Artech house.
4. Sackmann, E.K., A.L. Fulton, and D.J. Beebe, *The present and future role of microfluidics in biomedical research.* Nature, 2014. **507**(7491): p. 181-189.
5. Tian, W.-C. and E. Finehout, *Microfluidics for biological applications*. Vol. 16. 2009: Springer Science & Business Media.
6. Gomez, F.A., *Biological applications of microfluidics*. 2008: John Wiley & Sons.
7. Weibel, D.B. and G.M. Whitesides, *Applications of microfluidics in chemical biology.* Current opinion in chemical biology, 2006. **10**(6): p. 584-591.
8. Ohno, K.i., K. Tachikawa, and A. Manz, *Microfluidics: applications for analytical purposes in chemistry and biochemistry.* Electrophoresis, 2008. **29**(22): p. 4443-4453.
9. Abou‐Hassan, A., O. Sandre, and V. Cabuil, *Microfluidics in inorganic chemistry.* Angewandte Chemie International Edition, 2010. **49**(36): p. 6268-6286.
10. Kirby, B.J., *Micro-and nanoscale fluid mechanics: transport in microfluidic devices*. 2010: Cambridge university press.
11. Weng, C.-H., et al., *A suction-type, pneumatic microfluidic device for liquid transport and mixing.* Microfluidics and nanofluidics, 2011. **10**(2): p. 301-310.
12. Lee, C.-Y., et al., *Microfluidic mixing: a review.* International journal of molecular sciences, 2011. **12**(5): p. 3263-3287.
13. Suh, Y.K. and S. Kang, *A review on mixing in microfluidics.* Micromachines, 2010. **1**(3): p. 82-111.
14. Ward, K. and Z.H. Fan, *Mixing in microfluidic devices and enhancement methods.* Journal of Micromechanics and Microengineering, 2015. **25**(9): p. 094001.
15. Amato, L., et al., *Integrated three-dimensional filter separates nanoscale from microscale elements in a microfluidic chip.* Lab on a Chip, 2012. **12**(6): p. 1135-1142.

16. Salafi, T., K.K. Zeming, and Y. Zhang, *Advancements in microfluidics for nanoparticle separation.* Lab on a Chip, 2017. **17**(1): p. 11-33.
17. Karle, M., et al., *Microfluidic solutions enabling continuous processing and monitoring of biological samples: A review.* Analytica chimica acta, 2016. **929**: p. 1-22.
18. Olanrewaju, A., et al., *Capillary microfluidics in microchannels: from microfluidic networks to capillaric circuits.* Lab on a Chip, 2018. **18**(16): p. 2323-2347.
19. Cubaud, T. and T.G. Mason, *Capillary threads and viscous droplets in square microchannels.* Physics of fluids, 2008. **20**(5): p. 053302.
20. Yang, D., et al., *Dynamics of capillary-driven flow in open microchannels.* The Journal of Physical Chemistry C, 2011. **115**(38): p. 18761-18769.
21. Duncombe, T.A., A.M. Tentori, and A.E. Herr, *Microfluidics: reframing biological enquiry.* Nature Reviews Molecular Cell Biology, 2015. **16**(9): p. 554-567.
22. Lu, C. and S.S. Verbridge, *Microfluidic Methods for Molecular Biology*. Vol. 1. 2016: Springer.
23. Hopwood, A.J., et al., *Integrated microfluidic system for rapid forensic DNA analysis: sample collection to DNA profile.* Analytical chemistry, 2010. **82**(16): p. 6991-6999.
24. Cao, H., et al., *Gradient nanostructures for interfacing microfluidics and nanofluidics.* Applied Physics Letters, 2002. **81**(16): p. 3058-3060.
25. Neethirajan, S., et al., *Microfluidics for food, agriculture and biosystems industries.* Lab on a Chip, 2011. **11**(9): p. 1574-1586.
26. Ferry, J.D., *Viscoelastic properties of polymers*. 1980: John Wiley & Sons.
27. Bird, R.B., R.C. Armstrong, and O. Hassager, *Dynamics of polymeric liquids. Vol. 1: Fluid mechanics.* 1987.
28. Morozov, A.N. and W. van Saarloos, *An introductory essay on subcritical instabilities and the transition to turbulence in visco-elastic parallel shear flows.* Physics Reports, 2007. **447**(3-6): p. 112-143.
29. De Gennes, P., X. Hua, and P. Levinson, *Dynamics of wetting: local contact angles.* Journal of fluid mechanics, 1990. **212**: p. 55-63.
30. Larson, R.G., E.S. Shaqfeh, and S.J. Muller, *A purely elastic instability in Taylor–Couette flow*. Journal of Fluid Mechanics, 1990. **218**: p. 573-600.

31. Arratia, P.E., et al., *Elastic instabilities of polymer solutions in cross-channel flow.* Physical review letters, 2006. **96**(14): p. 144502.
32. McKinley, G.H., R.C. Armstrong, and R. Brown, *The wake instability in viscoelastic flow past confined circular cylinders.* Philosophical Transactions of the Royal Society of London. Series A: Physical and Engineering Sciences, 1993. **344**(1671): p. 265-304.
33. Shaqfeh, E.G., *Purely elastic instabilities in viscometric flows.* Annual Review of Fluid Mechanics, 1996(28): p. 129-185.
34. Pakdel, P. and G.H. McKinley, *Elastic instability and curved streamlines.* Physical Review Letters, 1996. **77**(12): p. 2459.
35. Rayleigh, L., *On the stability, or instability, of certain fluid motions.* Proc. London Math. Soc., 1880. **9**: p. 57-70.
36. Lam, Y., et al., *Micromixer based on viscoelastic flow instability at low Reynolds number.* Biomicrofluidics, 2009. **3**(1): p. 014106.
37. Nguyen, N.-T., *Micromixers: fundamentals, design and fabrication*. 2011: William Andrew.
38. Whalley, R., et al., *Enhancing heat transfer at the micro-scale using elastic turbulence.* Theoretical and Applied Mechanics Letters, 2015. **5**(3): p. 103-106.
39. Amini, H., W. Lee, and D. Di Carlo, *Inertial microfluidic physics.* Lab on a Chip, 2014. **14**(15): p. 2739-2761.
40. Zhang, H.-N., et al., *Characteristics and generation of elastic turbulence in a three-dimensional parallel plate channel using direct numerical simulation.* Chinese Physics B, 2016. **25**(9): p. 094701.
41. Kim, J.-H., A. Öztekin, and S. Neti, *Instabilities in viscoelastic flow past a square cavity.* Journal of non-newtonian fluid mechanics, 2000. **90**(2-3): p. 261-281.
42. Li, X.-B., et al., *Measuring elasticity-induced unstable flow structures in a curved microchannel using confocal micro particle image velocimetry.* Experimental Thermal and Fluid Science, 2016. **75**: p. 118-128.
43. Poole, R., A. Lindner, and M. Alves, *Viscoelastic secondary flows in serpentine channels.* Journal of Non-Newtonian Fluid Mechanics, 2013. **201**: p. 10-16.

44. Muller, S., E. Shaqfeh, and R. Larson, *Experimental studies of the onset of oscillatory instability in viscoelastic Taylor-Couette flow.* Journal of non-newtonian fluid mechanics, 1993. **46**(2-3): p. 315-330.
45. Gan, H.Y., et al., *Efficient mixing of viscoelastic fluids in a microchannel at low Reynolds number.* Microfluidics and Nanofluidics, 2007. **3**(1): p. 101-108.
46. Alves, M., F. Pinho, and P.J. Oliveira, *Visualizations of Boger fluid flows in a 4: 1 square–square contraction.* AIChE journal, 2005. **51**(11): p. 2908-2922.
47. Quinzani, L.M., R.C. Armstrong, and R.A. Brown, *Birefringence and laser-Doppler velocimetry (LDV) studies of viscoelastic flow through a planar contraction.* Journal of Non-Newtonian Fluid Mechanics, 1994. **52**(1): p. 1-36.
48. Gardner, K., et al., *Photon-correlation velocimetry of polystyrene solutions in extensional flow fields.* Polymer, 1982. **23**(10): p. 1435-1442.
49. Chow, A., et al., *Entanglements in polymer solutions under elongational flow: a combined study of chain stretching, flow velocimetry and elongational viscosity.* Macromolecules, 1988. **21**(1): p. 250-256.
50. Soulages, J., et al., *Investigating the stability of viscoelastic stagnation flows in T-shaped microchannels.* Journal of Non-Newtonian Fluid Mechanics, 2009. **163**(1-3): p. 9-24.
51. McKinley, G.H., P. Pakdel, and A. Öztekin, *Rheological and geometric scaling of purely elastic flow instabilities.* Journal of Non-Newtonian Fluid Mechanics, 1996. **67**: p. 19-47.
52. Larson, R.G., *Instabilities in viscoelastic flows.* Rheologica Acta, 1992. **31**(3): p. 213-263.
53. Owens, R.G. and T.N. Phillips, *Computational rheology*. 2002: World Scientific.
54. Fattal, R. and R. Kupferman, *Constitutive laws for the matrix-logarithm of the conformation tensor.* Journal of Non-Newtonian Fluid Mechanics, 2004. **123**(2-3): p. 281-285.
55. Crochet, M. and R. Keunings, *Finite element analysis of die swell of a highly elastic fluid.* Journal of Non-Newtonian Fluid Mechanics, 1982. **10**(3-4): p. 339-356.
56. Crochet, M. and R. Keunings, *Die swell of a Maxwell fluid: numerical prediction.* Journal of Non-Newtonian Fluid Mechanics, 1980. **7**(2-3): p. 199-212.
57. Lee, J., et al., *Practical comparison of differential viscoelastic constitutive equations in finite element analysis of planar 4: 1 contraction flow.* Rheologica Acta, 2004. **44**(2): p. 188-197.

58. Fattal, R. and R. Kupferman, *Time-dependent simulation of viscoelastic flows at high Weissenberg number using the log-conformation representation.* Journal of Non-Newtonian Fluid Mechanics, 2005. **126**(1): p. 23-37.

59. Renardy, M., *Current issues in non-Newtonian flows: a mathematical perspective.* Journal of non-newtonian fluid mechanics, 2000. **90**(2-3): p. 243-259.

60. Hulsen, M.A., R. Fattal, and R. Kupferman, *Flow of viscoelastic fluids past a cylinder at high Weissenberg number: stabilized simulations using matrix logarithms.* Journal of Non-Newtonian Fluid Mechanics, 2005. **127**(1): p. 27-39.

61. Vaithianathan, T. and L.R. Collins, *Numerical approach to simulating turbulent flow of a viscoelastic polymer solution.* Journal of Computational Physics, 2003. **187**(1): p. 1-21.

62. Lozinski, A. and R.G. Owens, *An energy estimate for the Oldroyd B model: theory and applications.* Journal of non-newtonian fluid mechanics, 2003. **112**(2-3): p. 161-176.

63. Afonso, A., F. Pinho, and M. Alves, *The kernel-conformation constitutive laws.* Journal of Non-Newtonian Fluid Mechanics, 2012. **167**: p. 30-37.

64. Kwack, J., A. Masud, and K. Rajagopal, *Stabilized mixed three‐field formulation for a generalized incompressible Oldroyd‐B model.* International Journal for Numerical Methods in Fluids, 2017. **83**(9): p. 704-734.

65. Martins, F., et al., *A numerical study of the kernel-conformation transformation for transient viscoelastic fluid flows.* Journal of Computational Physics, 2015. **302**: p. 653-673.

66. Napoli, M., J.C. Eijkel, and S. Pennathur, *Nanofluidic technology for biomolecule applications: a critical review.* Lab on a Chip, 2010. **10**(8): p. 957-985.

67. Masliyah, J.H. and S. Bhattacharjee, *Electrokinetic and colloid transport phenomena*. 2006: John Wiley & Sons.

68. Ichiyanagi, M., et al. *Spatial distribution of electrokinetically driven flow measured by micro-PIV (an evaluation of electric double layer in microchannel)*. in *12th International Symposium on Application of Laser Technology to Fluid Mechanics (CD-ROM)*. 2004.

69. Rathore, A.S., *Theory of electroosmotic flow, retention and separation efficiency in capillary electrochromatography.* Electrophoresis, 2002. **23**(22‐23): p. 3827-3846.

70. Yang, R.-J., L.-M. Fu, and Y.-C. Lin, *Electroosmotic flow in microchannels.* Journal of colloid and interface science, 2001. **239**(1): p. 98-105.

71. Reuss, F., *Charge-induced flow*. Proceedings of the Imperial Society of Naturalists of Moscow, 1809, 1809. **3**: p. 327-344.
72. Tang, Z., et al., *Electrokinetic flow control for composition modulation in a microchannel.* Journal of Micromechanics and Microengineering, 2002. **12**(6): p. 870.
73. Prabhakaran, R.A., et al., *Induced charge effects on electrokinetic entry flow*. Physics of Fluids, 2017. **29**(6): p. 062001.
74. Sadr, R., et al., *An experimental study of electro-osmotic flow in rectangular microchannels.* Journal of fluid mechanics, 2004. **506**: p. 357-367.
75. Tavares, M.F. and V.L. McGuffin, *Theoretical model of electroosmotic flow for capillary zone electrophoresis.* Analytical Chemistry, 1995. **67**(20): p. 3687-3696.
76. Wang, C., et al., *Characterization of electroosmotic flow in rectangular microchannels.* International journal of heat and mass transfer, 2007. **50**(15-16): p. 3115-3121.
77. Wang, J., M. Wang, and Z. Li, *Lattice Poisson–Boltzmann simulations of electro-osmotic flows in microchannels.* Journal of colloid and interface science, 2006. **296**(2): p. 729-736.
78. Fu, L.-M., J.-Y. Lin, and R.-J. Yang, *Analysis of electroosmotic flow with step change in zeta potential.* Journal of Colloid and Interface Science, 2003. **258**(2): p. 266-275.
79. Reuss, F.F., *Sur un nouvel effet de l'électricité galvanique.* Mem. Soc. Imp. Natur. Moscou, 1809. **2**: p. 327-337.
80. Dutta, P. and A. Beskok, *Analytical solution of combined electroosmotic/pressure driven flows in two-dimensional straight channels: finite Debye layer effects.* Analytical chemistry, 2001. **73**(9): p. 1979-1986.
81. Gao, Y., et al. *Theoretical investigation of two-fluid electroosmotic flow in microchannels*. in *Journal of Physics: Conference Series*. 2006. IOP Publishing.
82. Gao, Y., et al., *Numerical simulation of two-fluid electroosmotic flow in microchannels.* International journal of heat and mass transfer, 2005. **48**(25-26): p. 5103-5111.
83. Helmholtz, H.v., *Studien über electrische Grenzschichten.* Annalen der Physik, 1879. **243**(7): p. 337-382.
84. Von Smoluchowski, M., *Elektrische endosmose und stromungsstrome.* Handbuch del Elektrizitat und des Magnetismus, 1921. **2**: p. 366.
85. Rice, C.L. and R. Whitehead, *Electrokinetic flow in a narrow cylindrical capillary.* The Journal of Physical Chemistry, 1965. **69**(11): p. 4017-4024.

86. Levine, S., J.R. Marriott, and K. Robinson, *Theory of electrokinetic flow in a narrow parallel-plate channel.* Journal of the Chemical Society, Faraday Transactions 2: Molecular and Chemical Physics, 1975. **71**: p. 1-11.

87. Herr, A., et al., *Electroosmotic capillary flow with nonuniform zeta potential.* Analytical chemistry, 2000. **72**(5): p. 1053-1057.

88. Ghosal, S., *Lubrication theory for electro-osmotic flow in a microfluidic channel of slowly varying cross-section and wall charge.* Journal of Fluid Mechanics, 2002. **459**: p. 103-128.

89. Kim, M., A. Beskok, and K. Kihm, *Electro-osmosis-driven micro-channel flows: A comparative study of microscopic particle image velocimetry measurements and numerical simulations.* Experiments in Fluids, 2002. **33**(1): p. 170-180.

90. Kang, Y., C. Yang, and X. Huang, *Dynamic aspects of electroosmotic flow in a cylindrical microcapillary.* International Journal of Engineering Science, 2002. **40**(20): p. 2203-2221.

91. Xuan, X. and D. Li, *Electroosmotic flow in microchannels with arbitrary geometry and arbitrary distribution of wall charge.* Journal of colloid and interface science, 2005. **289**(1): p. 291-303.

92. Yan, D., C. Yang, and X. Huang, *Effect of finite reservoir size on electroosmotic flow in microchannels.* Microfluidics and Nanofluidics, 2007. **3**(3): p. 333-340.

93. Bianchi, F., R. Ferrigno, and H. Girault, *Finite element simulation of an electroosmotic-driven flow division at a T-junction of microscale dimensions.* Analytical Chemistry, 2000. **72**(9): p. 1987-1993.

94. Patankar, N.A. and H.H. Hu, *Numerical simulation of electroosmotic flow.* Analytical Chemistry, 1998. **70**(9): p. 1870-1881.

95. Zu, Y. and Y. Yan, *Numerical simulation of electroosmotic flow near earthworm surface.* Journal of Bionic Engineering, 2006. **3**(4): p. 179-186.

96. Chang, C. and R.-J. Yang, *Computational analysis of electrokinetically driven flow mixing in microchannels with patterned blocks.* Journal of Micromechanics and Microengineering, 2004. **14**(4): p. 550.

97. Keh, H.J. and Y.C. Liu, *Electrokinetic flow in a circular capillary with a surface charge layer.* Journal of colloid and interface science, 1995. **172**(1): p. 222-229.

98. Yang, R.-J., L.-M. Fu, and C.-C. Hwang, *Electroosmotic entry flow in a microchannel.* Journal of Colloid and Interface Science, 2001. **244**(1): p. 173-179.

99. Park, H., J. Lee, and T. Kim, *Comparison of the Nernst–Planck model and the Poisson–Boltzmann model for electroosmotic flows in microchannels.* Journal of colloid and interface science, 2007. **315**(2): p. 731-739.

100. D'Alessio, S. and J. Pascal, *Steady flow of a power-law fluid past a cylinder.* Acta Mechanica, 1996. **117**(1): p. 87-100.

101. Andersson, H., et al., *Flow of a power-law fluid film on an unsteady stretching surface.* Journal of Non-Newtonian Fluid Mechanics, 1996. **62**(1): p. 1-8.

102. Tripathi, A., R.P. Chhabra, and T. Sundararajan, *Power law fluid flow over spheroidal particles.* Industrial & engineering chemistry research, 1994. **33**(2): p. 403-410.

103. Hayat, T., et al., *Numerical simulation of heat transfer in MHD stagnation point flow of Cross fluid model towards a stretched surface.* Results in physics, 2017. **7**: p. 1824-1827.

104. Zimmerman, W., J. Rees, and T. Craven, *Rheometry of non-Newtonian electrokinetic flow in a microchannel T-junction.* Microfluidics and Nanofluidics, 2006. **2**(6): p. 481-492.

105. Akbar, N.S. and S. Nadeem, *Carreau fluid model for blood flow through a tapered artery with a stenosis.* Ain Shams Engineering Journal, 2014. **5**(4): p. 1307-1316.

106. Ellahi, R., et al., *Peristaltic flow of Carreau fluid in a rectangular duct through a porous medium.* Mathematical problems in Engineering, 2012. **2012**.

107. Das, M., V. Jain, and P. Ghoshdastidar, *Fluid flow analysis of magnetorheological abrasive flow finishing (MRAFF) process.* International Journal of Machine Tools and Manufacture, 2008. **48**(3-4): p. 415-426.

108. Frigaard, I., S. Howison, and I. Sobey, *On the stability of Poiseuille flow of a Bingham fluid.* Journal of Fluid Mechanics, 1994. **263**: p. 133-150.

109. Lipscomb, G. and M. Denn, *Flow of Bingham fluids in complex geometries.* Journal of Non-Newtonian Fluid Mechanics, 1984. **14**: p. 337-346.

110. Zhao, C., et al., *Analysis of electroosmotic flow of power-law fluids in a slit microchannel.* Journal of colloid and interface science, 2008. **326**(2): p. 503-510.

111. Vasu, N. and S. De, *Electroosmotic flow of power-law fluids at high zeta potentials.* Colloids and Surfaces A: Physicochemical and Engineering Aspects, 2010. **368**(1-3): p. 44-52.

112. Das, S. and S. Chakraborty, *Analytical solutions for velocity, temperature and concentration distribution in electroosmotic microchannel flows of a non-Newtonian bio-fluid.* Analytica chimica acta, 2006. **559**(1): p. 15-24.

113. Zhao, C. and C. Yang, *Electro-osmotic mobility of non-Newtonian fluids.* Biomicrofluidics, 2011. **5**(1): p. 014110.

114. Chakraborty, S., *Electroosmotically driven capillary transport of typical non-Newtonian biofluids in rectangular microchannels.* Analytica Chimica Acta, 2007. **605**(2): p. 175-184.

115. Olivares, M.L., L. Vera - Candioti, and C.L. Berli, *The EOF of polymer solutions.* Electrophoresis, 2009. **30**(5): p. 921-928.

116. Zhao, C. and C. Yang, *An exact solution for electroosmosis of non-Newtonian fluids in microchannels.* Journal of Non-Newtonian Fluid Mechanics, 2011. **166**(17-18): p. 1076-1079.

117. Park, H. and W. Lee, *Helmholtz–Smoluchowski velocity for viscoelastic electroosmotic flows.* Journal of colloid and interface science, 2008. **317**(2): p. 631-636.

118. Park, H. and W. Lee, *Effect of viscoelasticity on the flow pattern and the volumetric flow rate in electroosmotic flows through a microchannel.* Lab on a Chip, 2008. **8**(7): p. 1163-1170.

119. Afonso, A., M. Alves, and F. Pinho, *Analytical solution of mixed electro-osmotic/pressure driven flows of viscoelastic fluids in microchannels.* Journal of Non-Newtonian Fluid Mechanics, 2009. **159**(1-3): p. 50-63.

120. Afonso, A., M. Alves, and F. Pinho, *Electro-osmotic flow of viscoelastic fluids in microchannels under asymmetric zeta potentials.* Journal of Engineering Mathematics, 2011. **71**(1): p. 15-30.

121. Ferrás, L., et al., *Analytical and numerical study of the electro-osmotic annular flow of viscoelastic fluids.* Journal of colloid and interface science, 2014. **420**: p. 152-157.

122. Dhinakaran, S., et al., *Steady viscoelastic fluid flow between parallel plates under electro-osmotic forces: Phan-Thien–Tanner model.* Journal of colloid and interface science, 2010. **344**(2): p. 513-520.

123. Sousa, J., et al., *Effect of the skimming layer on electro-osmotic—Poiseuille flows of viscoelastic fluids.* Microfluidics and Nanofluidics, 2011. **10**(1): p. 107-122.

124. Choi, W., S.W. Joo, and G. Lim, *Electroosmotic flows of viscoelastic fluids with asymmetric electrochemical boundary conditions.* Journal of Non-Newtonian Fluid Mechanics, 2012. **187**: p. 1-7.

125. Le Bris, C. and T. Lelièvre, *Micro-macro models for viscoelastic fluids: modelling, mathematics and numerics.* Science China Mathematics, 2012. **55**(2): p. 353-384.

126. Comminal, R., J. Spangenberg, and J.H. Hattel, *Robust simulations of viscoelastic flows at high Weissenberg numbers with the streamfunction/log-conformation formulation.* Journal of Non-Newtonian Fluid Mechanics, 2015. **223**: p. 37-61.

127. Oldroyd, J.G., *On the formulation of rheological equations of state.* Proceedings of the Royal Society of London. Series A. Mathematical and Physical Sciences, 1950. **200**(1063): p. 523-541.

128. Kramers, H.A., *The behavior of macromolecules in inhomogeneous flow.* The Journal of Chemical Physics, 1946. **14**(7): p. 415-424.

129. Thien, N.P. and R.I. Tanner, *A new constitutive equation derived from network theory.* Journal of Non-Newtonian Fluid Mechanics, 1977. **2**(4): p. 353-365.

130. Phan-Thien, N., *A nonlinear network viscoelastic model.* Journal of Rheology, 1978. **22**(3): p. 259-283.

131. Bird, R., P. Dotson, and N. Johnson, *Polymer solution rheology based on a finitely extensible bead—spring chain model.* Journal of Non-Newtonian Fluid Mechanics, 1980. **7**(2-3): p. 213-235.

132. Peterlin, A., *Hydrodynamics of macromolecules in a velocity field with longitudinal gradient.* Journal of Polymer Science Part B: Polymer Letters, 1966. **4**(4): p. 287-291.

133. Chilcott, M. and J.M. Rallison, *Creeping flow of dilute polymer solutions past cylinders and spheres.* Journal of Non-Newtonian Fluid Mechanics, 1988. **29**: p. 381-432.

134. Giesekus, H., *A simple constitutive equation for polymer fluids based on the concept of deformation-dependent tensorial mobility.* Journal of Non-Newtonian Fluid Mechanics, 1982. **11**(1-2): p. 69-109.

135. Giesekus, H., *Constitutive equations for polymer fluids based on the concept of configuration-dependent molecular mobility: A generalized mean-configuration model.* Journal of non-newtonian fluid mechanics, 1985. **17**(3): p. 349-372.

136. Courant, R., K. Friedrichs, and H. Lewy, *Über die partiellen Differenzengleichungen der mathematischen Physik.* Mathematische annalen, 1928. **100**(1): p. 32-74.
137. Crank, J. and P. Nicolson. *A practical method for numerical evaluation of solutions of partial differential equations of the heat-conduction type*. in *Mathematical proceedings of the Cambridge philosophical society*. 1947. Cambridge University Press.
138. Clough, R.W. *The finite element method in plane stress analysis*. in *Proceedings of 2nd ASCE Conference on Electronic Computation, Pittsburgh Pa., Sept. 8 and 9, 1960*. 1960.
139. Blazek, J., *Structured finite volume schemes.* Computational Fluid Dynamics: Principles and Applications, 2nd ed.; Elsevier Science: Amsterdam, The Netherlands, 2005: p. 210-213.
140. Ferziger, J.H., M. Perić, and R.L. Street, *Computational methods for fluid dynamics*. Vol. 3. 2002: Springer.
141. Versteeg, H.K. and W. Malalasekera, *An introduction to computational fluid dynamics: the finite volume method*. 2007: Pearson education.
142. Lilek, Z.e. and M. Perić, *A fourth-order finite volume method with colocated variable arrangement.* Computers & Fluids, 1995. **24**(3): p. 239-252.
143. Hu, H.H. and D.D. Joseph, *Numerical simulation of viscoelastic flow past a cylinder.* Journal of non-newtonian fluid mechanics, 1990. **37**(2-3): p. 347-377.
144. Xue, S.-C., N. Phan-Thien, and R. Tanner, *Three dimensional numerical simulations of viscoelastic flows through planar contractions.* Journal of Non-Newtonian Fluid Mechanics, 1998. **74**(1-3): p. 195-245.
145. Mompean, G. and L. Thais, *Finite volume numerical simulation of viscoelastic flows in general orthogonal coordinates.* Mathematics and Computers in Simulation, 2010. **80**(11): p. 2185-2199.
146. Alves, M., F. Pinho, and P. Oliveira, *Effect of a high-resolution differencing scheme on finite-volume predictions of viscoelastic flows.* Journal of Non-Newtonian Fluid Mechanics, 2000. **93**(2-3): p. 287-314.
147. Favero, J., et al., *Viscoelastic fluid analysis in internal and in free surface flows using the software OpenFOAM.* Computers & chemical engineering, 2010. **34**(12): p. 1984-1993.
148. Pimenta, F. and M. Alves, *Stabilization of an open-source finite-volume solver for viscoelastic fluid flows.* Journal of Non-Newtonian Fluid Mechanics, 2017. **239**: p. 85-104.

149. Pimenta, F. and M.A. Alves, *Numerical simulation of electrically-driven flows using OpenFOAM.* arXiv preprint arXiv:1802.02843, 2018.

150. Pimenta, F. and M.A. Alves, *A coupled finite-volume solver for numerical simulation of electrically-driven flows.* Computers & Fluids, 2019. **193**: p. 104279.

151. Chen, X., et al., *A comparison of stabilisation approaches for finite-volume simulation of viscoelastic fluid flow*. International Journal of Computational Fluid Dynamics, 2013. **27**(6-7): p. 229-250.

152. Takamura, Y., et al., *Low-voltage electroosmosis pump for stand-alone microfluidics devices.* Electrophoresis, 2003. **24**(1-2): p. 185-192.

153. Li, L., et al., *Advancement of electroosmotic pump in microflow analysis: A review.* Analytica Chimica Acta, 2019. **1060**: p. 1-16.

154. Jiang, H., et al., *A microfluidic chip for blood plasma separation using electro-osmotic flow control.* Journal of Micromechanics and Microengineering, 2011. **21**(8): p. 085019.

155. Ermann, N., et al., *Promoting single-file DNA translocations through nanopores using electro-osmotic flow*. The Journal of chemical physics, 2018. **149**(16): p. 163311.

156. Huang, G., et al., *Electro-osmotic capture and ionic discrimination of peptide and protein biomarkers with FraC nanopores.* Nature communications, 2017. **8**(1): p. 1-11.

157. Bello, M.S., et al., *Electroosmosis of polymer solutions in fused silica capillaries.* Electrophoresis, 1994. **15**(1): p. 623-626.

158. Chang, F.-M. and H.-K. Tsao, *Drag reduction in electro-osmosis of polymer solutions.* Applied physics letters, 2007. **90**(19): p. 194105.

159. Kamişli, F., *Flow analysis of a power-law fluid confined in an extrusion die.* International journal of engineering science, 2003. **41**(10): p. 1059-1083.

160. Hakim, A., *Mathematical analysis of viscoelastic fluids of White-Metzner type.* Journal of Mathematical Analysis and Applications, 1994. **185**(3): p. 675-705.

161. Koszkul, J. and J. Nabialek, *Viscosity models in simulation of the filling stage of the injection molding process.* Journal of Materials Processing Technology, 2004. **157**(2): p. 183-187.

162. Öztekin, A., R.A. Brown, and G.H. McKinley, *Quantitative prediction of the viscoelastic instability in cone-and-plate flow of a Boger fluid using a multi-mode Giesekus model.* Journal of non-newtonian fluid mechanics, 1994. **54**: p. 351-377.

163. Zhao, C. and C. Yang, *Joule heating induced heat transfer for electroosmotic flow of power-law fluids in a microcapillary.* International journal of heat and mass transfer, 2012. **55**(7-8): p. 2044-2051.

164. Zhao, C. and C. Yang, *Electroosmotic flows of non-Newtonian power-law fluids in a cylindrical microchannel.* Electrophoresis, 2013. **34**(5): p. 662-667.

165. Tang, G., et al., *Electroosmotic flow of non-Newtonian fluid in microchannels.* Journal of Non-Newtonian Fluid Mechanics, 2009. **157**(1-2): p. 133-137.

166. Bryce, R. and M. Freeman, *Extensional instability in electro-osmotic microflows of polymer solutions.* Physical Review E, 2010. **81**(3): p. 036328.

167. Bryce, R. and M. Freeman, *Abatement of mixing in shear-free elongationally unstable viscoelastic microflows.* Lab on a Chip, 2010. **10**(11): p. 1436-1441.

168. Pimenta, F. and M. Alves, *Electro-elastic instabilities in cross-shaped microchannels.* Journal of Non-Newtonian Fluid Mechanics, 2018. **259**: p. 61-77.

169. Song, L., et al., *Electrokinetic instability in microchannel viscoelastic fluid flows with conductivity gradients.* Physics of Fluids, 2019. **31**(8): p. 082001.

170. Song, L., et al., *Elastic instabilities in the electroosmotic flow of non-Newtonian fluids through T-shaped microchannels.* Electrophoresis, 2020. **41**(7-8): p. 588-597.

171. Ko, C.H., et al., *Electroosmotic flow of non-Newtonian fluids in a constriction microchannel.* Electrophoresis, 2019. **40**(10): p. 1387-1394.

172. Sadek, S.H., F.T. Pinho, and M.A. Alves, *Electro-elastic flow instabilities of viscoelastic fluids in contraction/expansion micro-geometries.* Journal of Non-Newtonian Fluid Mechanics, 2020. **283**: p. 104293.

173. Afonso, A., F. Pinho, and M. Alves, *Electro-osmosis of viscoelastic fluids and prediction of electro-elastic flow instabilities in a cross slot using a finite-volume method.* Journal of Non-Newtonian Fluid Mechanics, 2012. **179**: p. 55-68.

174. Huang, Y., et al., *Experimental and theoretical investigations of non-Newtonian electro-osmotic driven flow in rectangular microchannels.* Soft Matter, 2016. **12**(29): p. 6206-6213.

175. Ronshin, F. and E. Chinnov, *Experimental characterization of two-phase flow patterns in a slit microchannel.* Experimental Thermal and Fluid Science, 2019. **103**: p. 262-273.

176. Nito, F., et al., *Quantitative evaluation of optical forces by single particle tracking in slit-like microfluidic channels.* The Journal of Physical Chemistry C, 2018. **122**(31): p. 17963-17975.

177. Sánchez, S., et al., *Joule heating effect on a purely electroosmotic flow of non-Newtonian fluids in a slit microchannel.* Journal of Non-Newtonian Fluid Mechanics, 2013. **192**: p. 1-9.

178. Alves, M., P. Oliveira, and F. Pinho, *A convergent and universally bounded interpolation scheme for the treatment of advection.* International journal for numerical methods in fluids, 2003. **41**(1): p. 47-75.

179. Duarte, A., A.I. Miranda, and P.J. Oliveira, *Numerical and analytical modeling of unsteady viscoelastic flows: The start-up and pulsating test case problems.* Journal of non-newtonian fluid mechanics, 2008. **154**(2-3): p. 153-169.

180. Patankar, S.V., *Numerical heat transfer and fluid flow*. 2018: CRC press.

181. Van Doormaal, J.P. and G.D. Raithby, *Enhancements of the SIMPLE method for predicting incompressible fluid flows.* Numerical heat transfer, 1984. **7**(2): p. 147-163.

182. Sze, A., et al., *Zeta-potential measurement using the Smoluchowski equation and the slope of the current–time relationship in electroosmotic flow*. Journal of colloid and interface science, 2003. **261**(2): p. 402-410.

183. Sousa, P.C., et al., *Measurement of relaxation times in extensional flow of weakly viscoelastic polymer solutions.* Rheologica Acta, 2017. **56**(1): p. 11-20.

184. Sirisinha, C., *A review of extrudate swell in polymers.* J. Sci. Soc. Thailand, 1997. **23**: p. 259-280.

185. James, D.F., *N1 stresses in extensional flows.* Journal of Non-Newtonian Fluid Mechanics, 2016. **232**: p. 33-42.

186. Latinwo, F. and C.M. Schroeder, *Determining elasticity from single polymer dynamics.* Soft Matter, 2014. **10**(13): p. 2178-2187.

187. Groisman, A. and V. Steinberg, *Efficient mixing at low Reynolds numbers using polymer additives.* Nature, 2001. **410**(6831): p. 905-908.

188. Grilli, M., A. Vázquez-Quesada, and M. Ellero, *Transition to turbulence and mixing in a viscoelastic fluid flowing inside a channel with a periodic array of cylindrical obstacles.* Physical review letters, 2013. **110**(17): p. 174501.

189. Burghelea, T., E. Segre, and V. Steinberg, *Elastic turbulence in von Karman swirling flow between two disks.* Physics of fluids, 2007. **19**(5): p. 053104.

190. Jovanović, M.R. and S. Kumar, *Nonmodal amplification of stochastic disturbances in strongly elastic channel flows.* Journal of non-newtonian fluid mechanics, 2011. **166**(14-15): p. 755-778.

191. Groisman, A. and V. Steinberg, *Elastic turbulence in curvilinear flows of polymer solutions.* New Journal of Physics, 2004. **6**(1): p. 29.

192. Ballesta, P. and M. Alves, *Purely elastic instabilities in a microfluidic flow focusing device.* Physical Review Fluids, 2017. **2**(5): p. 053301.

193. Soulies, A., et al., *Characterisation of elastic turbulence in a serpentine micro-channel.* Physics of Fluids, 2017. **29**(8): p. 083102.

194. Balkovsky, E., A. Fouxon, and V. Lebedev, *Turbulence of polymer solutions.* Physical Review E, 2001. **64**(5): p. 056301.

195. Fouxon, A. and V. Lebedev, *Spectra of turbulence in dilute polymer solutions.* Physics of Fluids, 2003. **15**(7): p. 2060-2072.

196. Li, S.K., A.H. Ghanem, and W.I. Higuchi, *Pore charge distribution considerations in human epidermal membrane electroosmosis.* Journal of pharmaceutical sciences, 1999. **88**(10): p. 1044-1049.

197. Lim, C.Y. and Y.C. Lam, *Analysis on micro-mixing enhancement through a constriction under time periodic electroosmotic flow.* Microfluidics and nanofluidics, 2012. **12**(1): p. 127-141.

198. Chakraborty, S. and S. Ray, *Mass flow-rate control through time periodic electro-osmotic flows in circular microchannels.* Physics of Fluids, 2008. **20**(8): p. 083602.

199. Dutta, P. and A. Beskok, *Analytical solution of time periodic electroosmotic flows: analogies to Stokes' second problem.* Analytical Chemistry, 2001. **73**(21): p. 5097-5102.

200. Ramos, A., et al., *AC electric-field-induced fluid flow in microelectrodes.* Journal of colloid and interface science, 1999. **217**(2).

201. Minor, M., et al., *Dynamic aspects of electrophoresis and electroosmosis: a new fast method for measuring particle mobilities.* Journal of Colloid and Interface Science, 1997. **189**(2): p. 370-375.

202. Studer, V., et al., *Fabrication of microfluidic devices for AC electrokinetic fluid pumping.* Microelectronic Engineering, 2002. **61**: p. 915-920.

203. Olesen, L.H., H. Bruus, and A. Ajdari, *ac electrokinetic micropumps: The effect of geometrical confinement, Faradaic current injection, and nonlinear surface capacitance.* Physical Review E, 2006. **73**(5): p. 056313.

204. Olesen, L.H., A. Ajdari, and H. Bruus. *AC electrokinetic micropumps: the effect of geometrical confinement*. in *9th International Conference on Miniaturized Systems for Chemistry and Life Sciences*. 2005.

205. Liu, Q.-s., Y.-j. Jian, and L.-g. Yang, *Time periodic electroosmotic flow of the generalized Maxwell fluids between two micro-parallel plates.* Journal of Non-Newtonian Fluid Mechanics, 2011. **166**(9-10): p. 478-486.

206. Jian, Y.-j., Q.-s. Liu, and L.-g. Yang, *AC electroosmotic flow of generalized Maxwell fluids in a rectangular microchannel.* Journal of Non-Newtonian Fluid Mechanics, 2011. **166**(21-22): p. 1304-1314.

207. Jabari Moghadam, A., *Time-periodic electroosmotic flow of non-Newtonian fluids in microchannels.* International Journal of Engineering, 2016. **29**(5): p. 706-714.

208. Moghadam, A.J. and P. Akbarzadeh, *Non-Newtonian fluid flow induced by pressure gradient and time-periodic electroosmosis in a microtube.* Journal of the Brazilian Society of Mechanical Sciences and Engineering, 2017. **39**(12): p. 5015-5025.

209. Alipanah, M. and A. Ramiar, *High efficiency micromixing technique using periodic induced charge electroosmotic flow: a numerical study.* Colloids and Surfaces A: Physicochemical and Engineering Aspects, 2017. **524**: p. 53-65.

210. Dawn, S. and S. Sarkar, *Control of Mass Flow-Rate of Viscoelastic Fluids Through Time-Periodic Electro-Osmotic Flows in a Microchannel.* Journal of Fluids Engineering, 2021. **143**(11).

APPENDIX A

CALCULATION OF LOG-CONFORMATION REFOMULATIOIN FOR THREE-DIMENSIONAL PROBLEM

For three-dimensional problems, the decomposition of Equation 2.19 yields:

$$\mathbf{\Omega}=\mathbf{R}\begin{bmatrix}0 & \omega_1 & \omega_2\\ -\omega_1 & 0 & \omega_3\\ -\omega_2 & -\omega_3 & 0\end{bmatrix}\mathbf{R}^T,\mathbf{B}=\mathbf{R}\begin{bmatrix}m_{11} & 0 & 0\\ 0 & m_{22} & 0\\ 0 & 0 & m_{33}\end{bmatrix}\mathbf{R}^T,\mathbf{N}=\mathbf{R}\begin{bmatrix}0 & n_1 & n_2\\ -n_1 & 0 & n_3\\ -n_2 & -n_3 & 0\end{bmatrix}\mathbf{R}^T. \tag{A.1}$$

The eigen-decomposition of the conformation tensor **c** can be written as

$$\mathbf{c}=\mathbf{R}\Lambda\mathbf{R}^T, \tag{A.2}$$

where $\mathbf{\Lambda}=\begin{bmatrix}\lambda_1 & 0 & 0\\ 0 & \lambda_2 & 0\\ 0 & 0 & \lambda_3\end{bmatrix}$, and λ_1, λ_2, and λ_3 are the eigenvalues of conformation tensor **c**, which can be calculated by:

$$\det\left(\mathbf{c}-\lambda_i\mathbf{I}\right)=0. \tag{A.3}$$

The above equation yields

$$\lambda_i^3+b\lambda_i^2+c\lambda_i+d=0, \tag{A.4}$$

where the coefficients *b*, *c*, and *d* are calculated by the components of **c**

$$\begin{aligned} b&=-c_{11}-c_{22}-c_{33},\\ c&=c_{11}c_{22}+c_{11}c_{33}+c_{22}c_{33}-c_{12}^2-c_{13}^2-c_{23}^2,\\ d&=-\det\left(\mathbf{c}\right). \end{aligned} \tag{A.5}$$

Then λ_i can be expressed as

$$\begin{aligned}
\lambda_1 &= -\frac{b}{3} + \sqrt[3]{-\frac{q}{2} + \sqrt{\frac{q^2}{4} + \frac{p^3}{27}}} + \sqrt[3]{-\frac{q}{2} - \sqrt{\frac{q^2}{4} + \frac{p^3}{27}}}, \\
\lambda_2 &= -\frac{b}{3} + \omega\sqrt[3]{-\frac{q}{2} + \sqrt{\frac{q^2}{4} + \frac{p^3}{27}}} + \omega^2\sqrt[3]{-\frac{q}{2} - \sqrt{\frac{q^2}{4} + \frac{p^3}{27}}}, \\
\lambda_2 &= -\frac{b}{3} + \omega^2\sqrt[3]{-\frac{q}{2} + \sqrt{\frac{q^2}{4} + \frac{p^3}{27}}} + \omega^2\sqrt[3]{-\frac{q}{2} - \sqrt{\frac{q^2}{4} + \frac{p^3}{27}}},
\end{aligned} \tag{A.6}$$

where $p = (3c - b^2)/(3a^2)$, $q = (27d - 9bc + 2b^3)/27$, and $\omega = (-1 + \sqrt{3}i)/2$.

The eigenvector corresponding to λ_i is then calculated by solving the following equation

$$\left(\mathbf{c} - \lambda_i \mathbf{I}\right) e_i = \mathbf{0}, \tag{A.7}$$

Define $s_1 = (c_{22} - \lambda_i)(c_{33} - \lambda_i) - c_{23}c_{32}$, $s_2 = (c_{11} - \lambda_i)(c_{33} - \lambda_i) - c_{13}c_{31}$, $s_3 = (c_{11} - \lambda_i)(c_{22} - \lambda_i) - c_{12}c_{21}$, and then the eigenvector can be expressed as

$$\begin{aligned}
\mathbf{v}_i &= \left[1 \quad \frac{c_{23}c_{31} - \left(c_{33} - \lambda_i\right)c_{21}}{s_1} \quad \frac{c_{32}c_{21} - \left(c_{22} - \lambda_i\right)c_{21}}{s_1}\right], \text{ if } \max\left(\left|s_j\right|\right) = \left|s_1\right|, \\
\mathbf{v}_i &= \left[\frac{c_{13}c_{32} - \left(c_{33} - \lambda_i\right)c_{12}}{s_2} \quad 1 \quad \frac{c_{31}c_{12} - \left(c_{11} - \lambda_i\right)c_{32}}{s_2}\right], \text{ if } \max\left(\left|s_j\right|\right) = \left|s_2\right|, \\
\mathbf{v}_i &= \left[\frac{c_{12}c_{23} - \left(c_{22} - \lambda_i\right)c_{13}}{s_3} \quad \frac{c_{21}c_{13} - \left(c_{11} - \lambda_i\right)c_{23}}{s_3} \quad 1\right], \text{ if } \max\left(\left|s_j\right|\right) = \left|s_3\right|.
\end{aligned} \tag{A.8}$$

Then Equation 2.30 becomes

$$\begin{aligned}
&\begin{bmatrix} m_{11} & m_{12} & m_{13} \\ m_{21} & m_{22} & m_{23} \\ m_{31} & m_{32} & m_{33} \end{bmatrix} = \begin{bmatrix} 0 & \omega_1 & \omega_2 \\ -\omega_1 & 0 & \omega_3 \\ -\omega_2 & -\omega_3 & 0 \end{bmatrix} + \begin{bmatrix} m_{11} & 0 & 0 \\ 0 & m_{22} & 0 \\ 0 & 0 & m_{33} \end{bmatrix} \\
&+ \begin{bmatrix} 0 & n_1 & n_2 \\ -n_1 & 0 & n_3 \\ -n_2 & -n_3 & 0 \end{bmatrix} \begin{bmatrix} \lambda_1 & 0 & 0 \\ 0 & \lambda_2 & 0 \\ 0 & 0 & \lambda_3 \end{bmatrix}^{-1}.
\end{aligned} \tag{A.9}$$

The above equation yields

$$\begin{cases} m_{12} = \omega_1 + \dfrac{n_1}{\lambda_2} \\ m_{13} = \omega_2 + \dfrac{n_2}{\lambda_3} \\ m_{21} = -\omega_1 - \dfrac{n_1}{\lambda_1} \\ m_{23} = \omega_3 + \dfrac{n_3}{\lambda_3} \\ m_{31} = -\omega_2 - \dfrac{n_2}{\lambda_1} \\ m_{32} = -\omega_3 - \dfrac{n_3}{\lambda_2} \end{cases}. \tag{A.10}$$

Then ω_1, ω_2, ω_3, n_1, n_2, and n_3 are calculated as

$$\begin{cases} \omega_1 = \dfrac{\lambda_2 m_{12} + \lambda_1 m_{21}}{\lambda_2 - \lambda_1} \\ \omega_2 = \dfrac{\lambda_3 m_{13} + \lambda_1 m_{31}}{\lambda_3 - \lambda_1} \\ \omega_3 = \dfrac{\lambda_3 m_{23} + \lambda_2 m_{32}}{\lambda_3 - \lambda_2} \\ n_1 = \dfrac{m_{12} + m_{21}}{\lambda_2^{-1} - \lambda_1^{-1}} \\ n_2 = \dfrac{m_{13} + m_{31}}{\lambda_3^{-1} - \lambda_1^{-1}} \\ n_3 = \dfrac{m_{23} + m_{32}}{\lambda_3^{-1} - \lambda_2^{-1}} \end{cases}. \tag{A.11}$$

APPENDIX B

SUMMARY OF NUMERICAL METHODS USED IN THE VISCOELASTIC SOLVER

Table B.1. Summary of current studies on elastic instabilities of viscoelastic EOF.

Terms	Numerical method
Convective terms	CUBISTA scheme
Laplacian and gradient terms	Central differences
Time derivatives	Three-time level explicit difference scheme
Exponential source term	Taylor expansion
Velocity-pressure coupling	SIMPLEC algorithm
Pressure field	PCG solver
Velocity field	PBiCG solver

APPENDIX C

ELASTIC INSTABILITIES OF VISCOELASTIC EOF

Table C.1. Summary of current studies on elastic instabilities of viscoelastic EOF.

Geometry	Fluids	Electrical parameters	Instabilities
Constriction channel [166] Contraction ratio: 2:1 Width: 200 μm and 100 μm Depth: 20 μm	PAA (18×10^6 and 5×10^6 Da) with 20:80 vol.% methanol: water mixture. 1−480 ppm.	Electro-osmotic mobility: $(5.6\pm0.5)\times10^{-4}$, $(5.7\pm0.7)\times10^{-4}$, and $(3.1\pm0.2)\times10^{-4}$ cm^2/Vs for polymer free, high molecular weight, and low molecular weight 120 ppm PAA solutions. Electric field: 0−900 V/cm.	1. High molecular weight PAA solution leads to fluctuation above a critical flow rate. 2. The fluctuation is dependent on the polymer concentration.
Cross slot channel [148,149] Width: 100 μm Height: 50 μm	PAA, 5×10^6 Da, 300 and 1000 ppm.	Electro-osmotic mobility: $(6.4\pm0.2)\times10^{-4}$, $(7.2\pm0.1)\times10^{-4}$ cm^2/Vs for 1000 ppm and 300 ppm PAA solutions. ΔV = 20−140 V.	1. For both 300 ppm and 1000 ppm PAA solution, transition from steady state to time-dependent state was observed at ΔV = 20−140 V. 2. The fluctuation of the EOF does not enhance mixing effect.
T-shaped channel [170] Main-branch: Width: 200 μm Depth: 30 μm Side-branch 1: Width: 100 μm Depth: 50 μm Side-branch 2: Width: 100 μm Depth: 67 μm	Phosphate buffer-based aqueous polymer solutions. (500 ppm XG, 5% PVP, 2000 ppm PEO, 200 ppm PAA, 1000 ppm hyaluronic acid (HA)).	Electro-osmotic mobility: 3.5×10^{-4}, 0.1×10^{-4}, 4.6×10^{-4}, 0.1×10^{-4}, and 4.2×10^{-4} cm^2/Vs for XG, PVP, HA, PEO, PAA solutions. ΔV = 100−500 V.	1. Fluid shear-thinning might be the primary cause of electro-elastic instabilities (fluctuation of velocity). 2. Fluid elasticity alone does not cause instability. 3. Threshold voltage for the onset of instability decreases with the increase of polymer concentration. 4. Increasing the buffer concentration causes a rise of threshold voltage.
Constriction channel [171] Contraction ratio: 10:1 Width: 400 μm and 40 μm	1 mM phosphate buffer-based aqueous polymer solutions.	Electro-osmotic mobility: 0.54×10^{-4}, 0.75×10^{-4}, 0.06×10^{-4}, 0.14×10^{-4},	1. Fluid elasticity alone does not cause instability. 2. Fluid shear-thinning effect alone

Depth: 40 μm depth Length of constriction: 200 μm	(2000 ppm XG, 5% PVP, 3000 ppm PEO, and 200 ppm PAA.)	1.82×10^{-4} cm^2/Vs for buffer, XG, PVP, PEO, PAA solutions. Electric field: 100–400 V/cm.	caused counter-rotating circulations in weakly elastic XG solution. 3. No electric field-dependent phenomenon was observed in strong viscoelastic and shear-thinning PAA solutions.
Hyperbolic/abrupt contraction with abrupt/ hyperbolic expansion [172] Channel 1: (7.2:1) Width: 401 μm and 56 μm Depth: 100 μm Length of constriction: 382 μm Channel 2: (22.4:1) Width: 403 μm and 18 μm Depth: 100μm Length of constriction: 128μm	1 mM borate buffer with 0.05% wt. sodiumdodecylsulfate. 100, 300, 1000, and 10000 ppm PAA solutions.	Electro conductivity: 20.2, 55.5, 178.3 and 161.8 μS/cm for 100, 300, 1000, and 10000 ppm PAA solutions. ΔV = 2.5−90 V.	1. For hyperbolic contraction, upstream vortices were observed on high contraction ratio geometry. The vortices grow with increasing electric field. 2. For abrupt contraction, small vortices were observed at the entrance of low contraction ratio geometry. 3. For abrupt contraction, small vortices and large flow circulation were observed near the entrance. And large downstream vortices were observed for 1000 ppm PAA solution.

APPENDIX D

BOUNDARY CONDITIONS

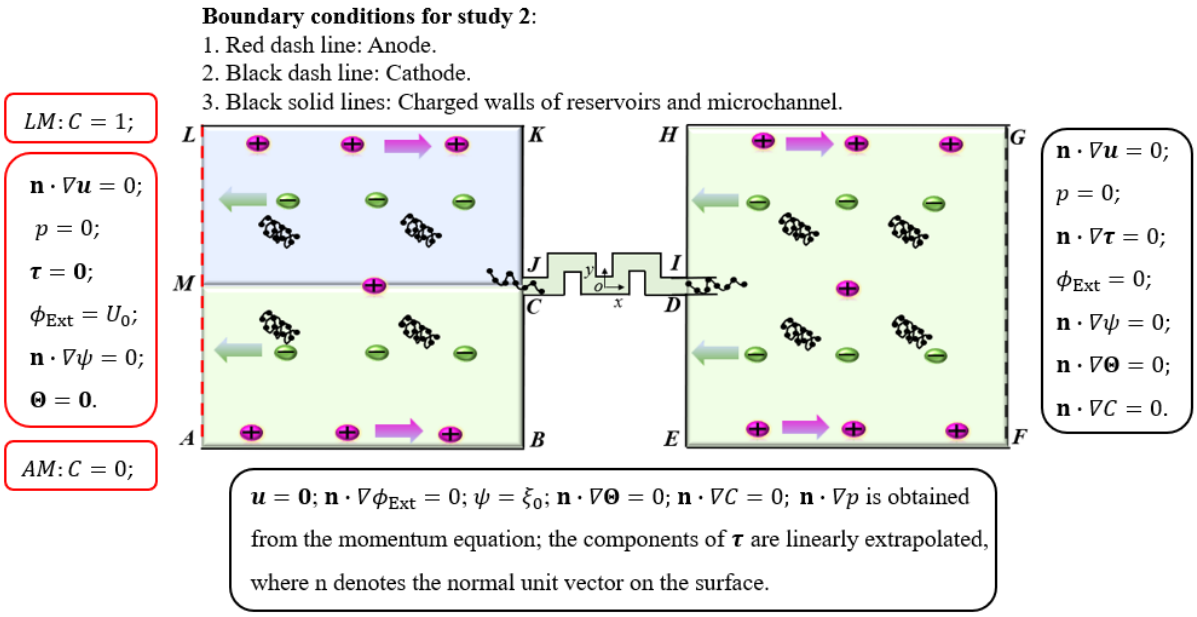

Figure D.1 Boundary conditions for study 2 in Chapter 4.

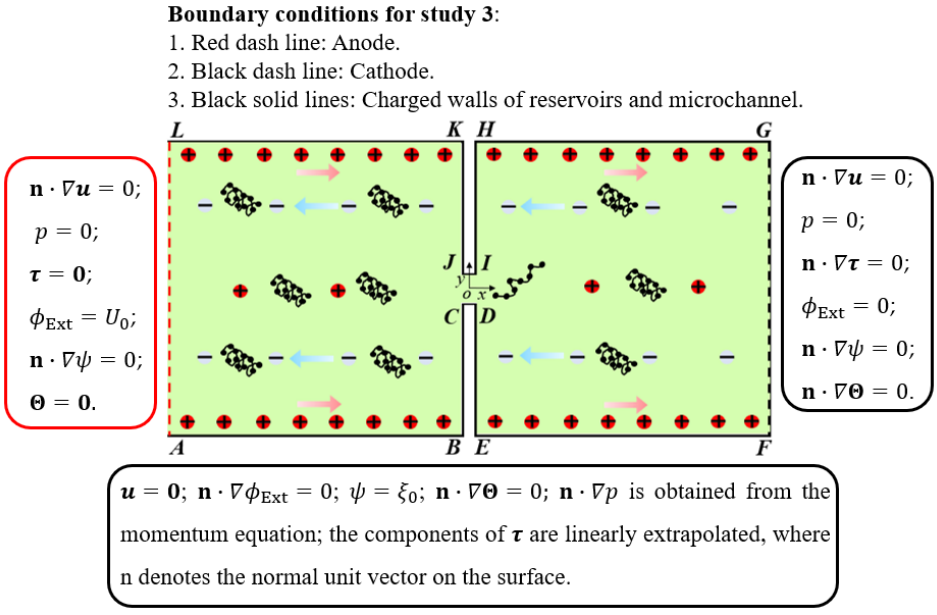

Figure D.2 Boundary conditions for study 3 in Chapter 5.

VITA

Jianyu Ji

Department of Mechanical Engineering

Old Dominion University, Norfolk, VA 23529

Educational Background

- Ph.D. in Mechanical Engineering, Old Dominion University, Norfolk, VA. (2019-2022)
- Master in Engineering Mechanics, Nanjing University of Aeronautics and Astronautics, Nanjing, China. (2016-2019)
- Bachelor in Engineering Mechanics, Nanjing University of Aeronautics and Astronautics, Nanjing, China. (2012-2016)

Selected Publications

- **J. Ji**, S. Qian, and Z. Liu, Electroosmotic flow of viscoelastic fluid through a constriction microchannel. Micromachines, 2021, 12, 417.
- **J. Ji**, S. Qian, A. M. Parker, and X. Zhang, Pulsating electroosmotic flow of viscoelastic fluid through microchannel with 90° bends. (Manuscript)
- **J. Ji**, S. Qian, A. M. Parker, and X. Zhang, Frequency study of time-periodic electroosmotic flow of viscoelastic fluid through short constriction microchannel. (Manuscript)